≪UNIVERSITÀ DEGLI STUDI DI NAPOLI FEDERICO II≫

Facoltá di Scienze Matematiche, Fisiche e Naturali

Dipartimento di Scienze Fisiche

XVIII ciclo di dottorato in

Fisica fondamentale ed applicata

Tesi di dottorato di ricerca

Opto-mechanical effects in nematic and cholesteric liquid crystals

Dottorando

dott. Antonio Setaro

Coordinatore del ciclo

prof. Arturo Tagliacozzo

Napoli, Novembre 2005

ad Onga

ed Opa

Contents

Introduction

At the beginning of the research in liquid crystals the German physicist O. Lehmann observed under microscope that cholesteric droplets, put under a thermal gradient, began to rotate. Such phenomenon is nowadays known as the Lehmann rotation.

In spite of its relative simplicity, this phenomenon is very intriguing because it is strictly related to non-equilibrium thermodynamics in chiral media, where *strange* phenomena could take place: for example a thermodynamic force (whose vectorial nature is polar) could be coupled to a flux of axial vectorial nature. The Lehmann rotation phenomenon is due, in particular, to the coupling between an applied thermal gradient or electrostatic field and the induced torque that puts in rotation the cholesteric drop.

Usually such effects are very weak and thus very difficult to detect since the chirality degree of materials formed by chiral molecules is very low. Cholesteric liquid crystals, on the contrary, possess a *structural*, macroscopic chirality; their chirality degree is much higher than systems based on the molecular chirality, so that these materials are good candidates to observe the cross-coupling phenomena.

Since Lehman's observations made at the end of the 19th century, very few works appeared subsequently on this subject, because it is very difficult to realize appropriate experimental geometries where competing effects (as the flexo-electric effect, for example) are negligible. The idea behind the present

work is to exploit a focalized laser beam to create a cholesteric droplet in a nematic environment, possessing a cylindrical symmetry around the director angular velocity induced by the external polar field. Laser light plays, in such a configuration, an auxiliary role; its utility lies in the fact that, by mean of it, we may control at will the geometry of the cholesteric profile so to avoid spurious effects as the flexoelectric effect.
During this work we exploited an experimental apparatus able to detect the whole transverse profile of the molecular reorientation present in the illuminate zone and not only the amount of induced birefringence. Besides the light-assisted Lehman effect, which was the main goal of this work, we were able to observe other yet not reported phenomena as the laser-induced rigid rotation of the whole reorientation profile and of the molecular director in nematics, the laser-induced "frozen" low-birefringent steady state and the laser-induced director rotation in cholesterics (the last two phenomena were predicted theoretically but not yet observed experimentally, at our knowledge).

In the **first chapter** we will shortly describe the results of nonequilibrium thermodynamics, paying attention to the phenomenological equations and their relation to the symmetry of the physical system (Curie's principle). We'll then describe briefly chirality and expose Pomeau's idea about *strange* transport phenomena in optically active fluids and how they can be exploited to obtain an enantiomers separation in a racemic mixture.

In the **second chapter** we'll briefly describe the liquid crystalline mesophases, paying particular attention to the nematic and cholesteric ones, and to their elastic properties.

The **third chapter** will be devoted to the description of the interaction between liquid crystals (LC) and external (electrostatic, magnetic and optical) fields. The Freédericksz effect will be described and then specialized to two interesting configurations: nematic samples under circularly polarized light and cholesteric samples under linearly or circularly polarized light.

The **fourth chapter** will be devoted to the Lehmann effect: it's history will be reviewed as well as the principal efforts performed to replicate it or to measure the coupling constant between polar and axial vectors (in particular, thermo- and electro-mechanical coupling constants). The chapter will close with the exposition of the idea behind our experiment.

The **fifth chapter** will be devoted to describe the evolution of our detection apparatus through different stages and why it was evolved in this way. Moreover, it will be discussed how to interpret the camera acquisitions obtained from our detection apparatus in its final configuration, a configuration, as we know, never used before to study the interaction between light and liquid crystals. The last part of this chapter will be devoted to the description of the mixture we chose to use in such work.

The **sixth chapter** will be devoted to our experimental observations on nematic liquid crystals under linearly and circularly polarized light. Our detection apparatus lead us to observe an unexpected dynamical response for circularly polarized light, namely the light-induced rigid rotation of the molecular director and of the whole reorientation profile. A 3-D model has been described in the last part of the chapter, which accounts fairly well for the experimental observations.

The **seventh chapter** will be devoted to the experimental characterization of the OFT in cholesterics for linearly, circularly and depolarized impinging light. The cholesteric response in such configurations shows features that was never observed before and that are predicted, for the case of circularly polarized impinging light, from a very recent numerical model.

The **eighth and last chapter** will be finally devoted to the search of the light-assisted Lehmann rotation induced by an electrostatic field. When the cholesteric "droplet" was created by the depolarized light, the system shows the same features of the Lehmann rotation. When circularly polarized light is exploited, instead, we could observe the competition between the photon spin

angular momentum transfer to the cholesteric and the Lehmann torque induced by the electrostatic field.

Chapter 1

Vectors, pseudovectors and chirality

1.1 Reflections

If one considers a coordinate transformation from a cartesian system $\{x, y, z\}$ to another $\{x', y', z'\}$, this transformation can be represented by means of an orthogonal matrix $\mathcal{Q} = \{q_{ij}\}$, so that a vector $\vec{v}$ will be transformed, in the new system of reference, in:

$$\vec{v}\,' = \widehat{\mathcal{Q}}\,.\,\vec{v} \quad \text{or, component by component:} \quad v_i' = \sum_j q_{ij} v_j. \tag{1.1.1}$$

If we consider a reflection or inversion of the axis, its matrix will be in the form:

$$q_{ij} = -\delta_{ij} \tag{1.1.2}$$

and thus

$$v_i' = -v_i. \tag{1.1.3}$$

It is worth noting that such transformation will change the initial right-handed coordinate system into a left-handed one. If we consider the distance vector

$$\vec{r} = (x_1, x_2, x_3) \tag{1.1.4}$$

it will transformed through $\mathcal{Q}$ into the vector

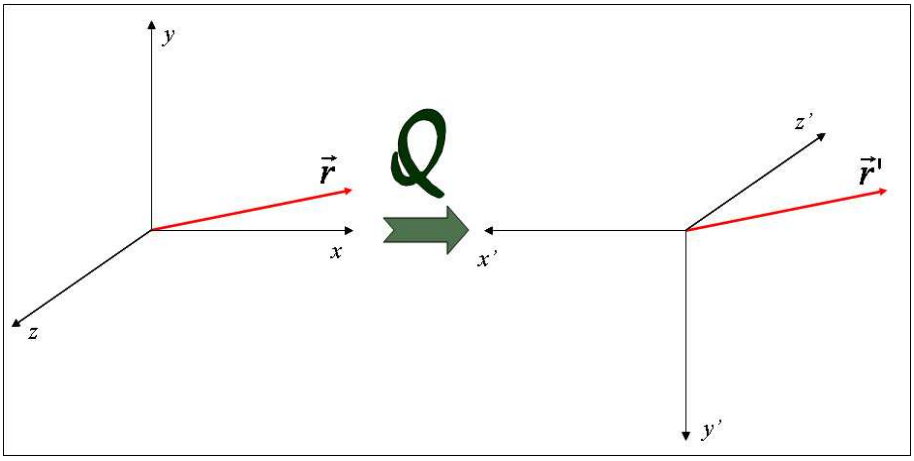

Figure 1.1: Behavior of a polar vector under the action of a inversion $\mathcal{Q}$ of the cartesian coordinates.

$$\vec{r}\,' = (x_1', x_2', x_3') = (-x_1, -x_2, -x_3) \tag{1.1.5}$$

whose components are negative. Remembering that the new set of axis is opposite to the original, the transformation result will be to leave $\vec{r}$ exactly as it was before the transformation was carried out, as shown in figure 1.1.
The distance vector $\vec{r}$ and all other vectors behaving this way under reflection of the coordinate system are called *polar vectors* or, shortly, *vectors*.

A fundamental difference appears when we consider a vector defined as the cross product of two polar vectors. Let

$$\vec{c} = \vec{a} \wedge \vec{b} \quad \text{or, component by component:} \quad c_i = \varepsilon_{ijk} a_j b_k. \tag{1.1.6}$$

where $\vec{a}$ and $\vec{b}$ are both polar vectors. When the coordinate system is inverted:

$$\begin{cases} a_i \to -a_i \\ b_i \to -b_i \end{cases} \tag{1.1.7}$$

From the definition of $\vec{c}$ it will transform in

$$c_i' = c_i \tag{1.1.8}$$

that is $\vec{c}$ doesn't behave like a polar vector under reflection (see figure 1.2), being reflected under a reflection transform. These kind of objects are called *axial vectors* or *pseudovectors*. Example of pseudovectors are the angular velocity ($\vec{\omega} = \vec{r} \wedge \vec{v}$), the angular momentum ($\vec{L} = \vec{r} \wedge \vec{p}$), the torque ($\vec{N} = \vec{r} \wedge \vec{f}$) or magnetic induction field ($\frac{\partial \vec{B}}{\partial t} = -\nabla \wedge \vec{E}$).

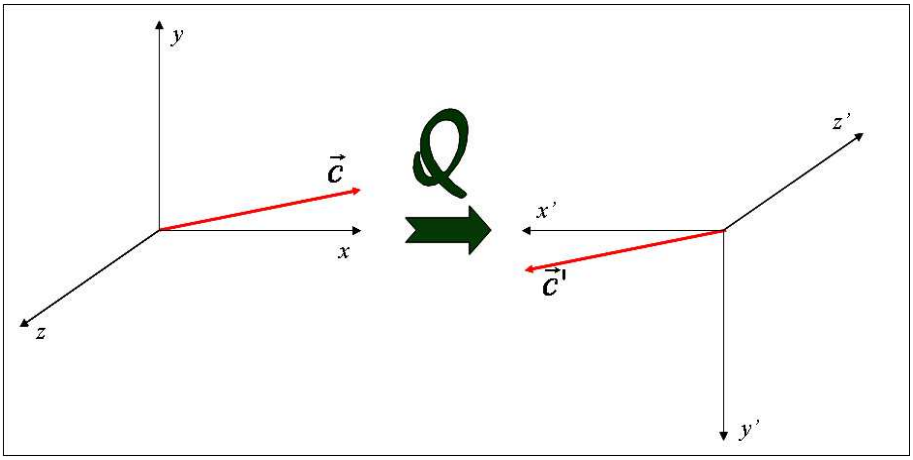

Figure 1.2: Behavior of an axial vector under the action of a inversion $\mathcal{Q}$ of the cartesian coordinates.

If we agree that the universe does not care whether we use right- or left-handed system, then it does no make sense to add an axial vector to a polar vector. In vector equations like $\vec{a} = \vec{b}$, either $\vec{a}$ and $\vec{b}$ must be both polar vectors or axial vectors. There are exception to this prohibition: where the universe distinguish between right-handed and left-handed systems, in the beta decay, for example, it is possible to add polar and axial vectors.

1.2 Entropy production and phenomenological equations

Considering the thermodynamical evolution of a physical system, one has to consider the law of conservation of the energy (basing on the first law of thermodynamics) and the entropy production law (the second law of thermodynamics).

If one considers the structure of the expression for the entropy production, one can see that it consists of a sum of products of two factors. One of this factors in each term is a *flow* quantity (for example heat flow, diffusion flow, chemical reaction rate and so on). The other factor in each term is related to a gradient of an intensive state variable and may contain external forces $\vec{F}_k$. Usually one refers to the first factor in such terms as **flux** J_i and to the second factor as **thermodynamic force** X_i, or *affinity*. The expression for the entropy production is thus:

$$T\dot{S} = \sum_i J_i X_i \tag{1.2.9}$$

The expression for the entropy production vanishes when the system is at the thermodynamic equilibrium, when all the forces and fluxes simultaneously vanish. For irreversible processes, one has to compute the expression for the entropy production. For a large class of irreversible phenomena under a wide range of experimental conditions, the irreversible flows are linear functions of the thermodynamic forces and can be expressed by means of phenomenological laws which are introduced *ad hoc* in the purely phenomenological theories of irreversible processes. As an example one can consider Fourier's law for heat conduction, in which the components of the heat flow are expressed as linear functions of the components of the temperature gradient. If one restrict to this linear region, one may write quite generally

$$J_i = \sum_k L_{ik} X_k. \tag{1.2.10}$$

The quantities L_{ik} are called *phenomenological coefficients* and the relations (1.2.10) are called as *phenomenological equations*.

If one introduces the phenomenological equations into the expression for the entropy production (1.2.9), one gets a quadratic expression in the thermodynamic forces of the form

$$T\dot{S} = \sum_{ik} L_{ik} X_i X_k. \tag{1.2.11}$$

It could arise the question about the validity of the linear approximation versus the introduction of nonlinear phenomenological laws. For ordinary transport

phenomena like heat and electric conduction, it is verified that the linear approximation holds under every experimental conduction. In other cases, as for example in systems performing chemical reactions, one has to work in a very limited range close to the equilibrium to ensure the validity of the linear approximations.

1.3 Curie principle and the influence of symmetry properties of matter on the linear laws.

In principle, any component of a flux can be a linear function of the components of all the thermodynamic forces. It is worth noting that fluxes and thermodynamic forces do not have the same tensorial character: they can be scalars, vectors or (second rank) tensors. This means that, under rotations and reflections, their components transform in different ways.

As a consequence, symmetry properties of the material system considered may have the effect that the components of the fluxes do not depend to on all components of the thermodynamic forces or that not every kind of flux will depend from every kind of thermodynamical force. This is known as the *Curie symmetry principle* [Curie (1894)]. By means of such reasonings, it can be shown, as anticipated in section 1.1, that in an isotropic system fluxes and forces of different tensorial character (as vectors and pseudovectors) do not couple. The symmetry, or its lack, will determine the nature of the possible couplings between forces and fluxes.

The spatial symmetry of the system conditions the nature of the couplings between forces and fluxes in the phenomenological equations. The property of time reversal invariance of the system at the microscopic level influences besides the inverse equations, reverting the rules between "causes" and "effects". These reverting relations are known as the Onsanger reciprocal relations and won't be described here because of the dependence of their expression from the nature of the system (for example, whether it is under the action of a magnetic field or not). Their derivation and expression can be found, for example, on reference [de

Groot and Marur (1962)].

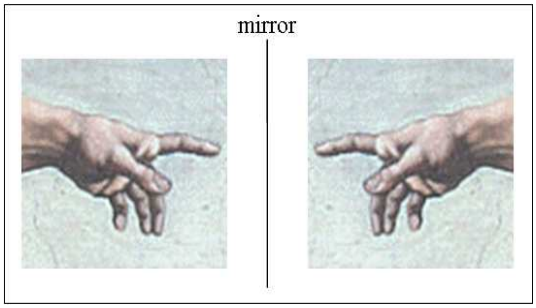

Figure 1.3: Adam's hand and its mirror reflection. Hand is a chiral object: it can not be superimposed to its mirror image.

1.4 Chirality

The word "chirality" comes from the ancient Greek $\chi\epsilon\acute{\iota}\rho$, hand. Chirality thus means *handedness*. The definition of chirality is due to Lord Kelvin[1] and it is related to the geometrical properties of an object: a figure is *chiral* if it is not identical to its mirror image or, in mathematical terms, if it cannot be mapped to its mirror image by applying only rotations and translations. The simplest example of chiral object coming from everyday life is the hand (see figure 1.3). An object superimposable with its mirror image is said to be *achiral*. It is worth noting that doesn't possess much sense speaking of the "amount" of chirality of an object: it can be superimposable to its mirror image (chiral) or it can not be (achiral). There are not other possibilities.
As shown in figure 1.4, chiral objects don't possess planes of symmetry.
Although the introduction of the concept of chirality could seem a "useless" geometrical concept, chirality has great consequences on our life. Chiral molecules possess, as discovered by Biot, rotatory power, that is they can rotate the direction of the polarization of light.
The two different antipodal species of the same chiral molecule with opposite

[1] Lord Kelvin's words: "I call any geometrical figure, or group of points, chiral, and say that it has chirality if its image in a plane mirror, ideally realized, cannot be brought to coincide with itself".

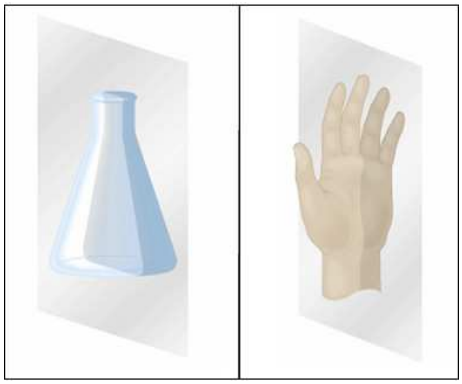

Figure 1.4: Chiral objects, unlike achiral, don't possess planes of symmetry.

handedness are said *enantiomers* and are labelled by the addiction of a L- or D- suffix to the name of the species, according to the versus of the rotatory power of the respective species (see figure 1.5).
The active ingredients in caraway seeds and spearmint demonstrate the great difference arising between the different handedness of the enantiomers of the same chemical species: though they have identical molecular structures, the two substances taste differently because they are opposite in chirality. Another, and

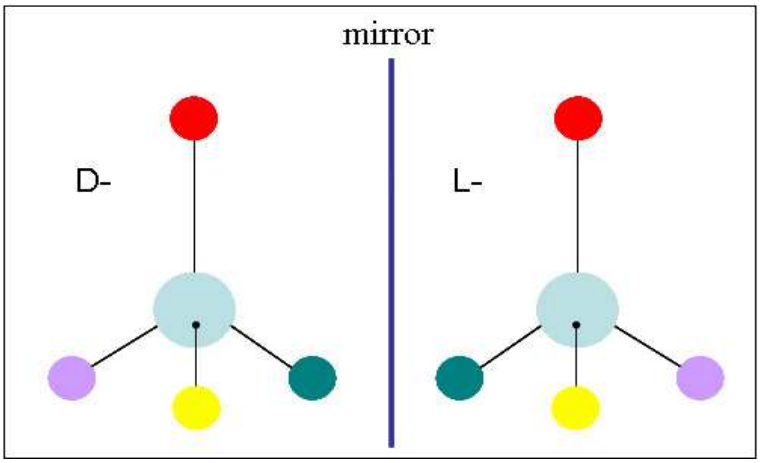

Figure 1.5: D- and L- enantiomers of a chiral molecule.

more dramatic example comes from drug research and pharmacology: the tragic administration of thalidomide to pregnant women in the 1960s. R-thalidomide possess sedative properties while its S- enantiomer induces fetal malformations. What could seem a mathematical game can cause giant differences in our life. A 50/50 mixture of L- and D- enantiomers of the same chiral molecule is said *racemic* and doesn't show optical activity.

1.5 Transport phenomena for optically active molecules

As pointed out by Pomeau [Pomeau (1971)], a system in which Curie's principle consequences can be observed are optically active fluids, fluids consisting of optically active left- or right-handed molecules and thus violating parity.
In such systems are allowed fluxes like:

$$\begin{cases} \vec{J} = \alpha_{i,j}\ \vec{F_i} \wedge \vec{F_j} \\ \\ \vec{J} = \beta\ \nabla \wedge \vec{v} \end{cases} \tag{1.5.12}$$

The phenomenological coefficients $\alpha_{i,j}$ and β depend upon the thermodynamic forces and flux under consideration and they reverse their sign depending from which kind of molecules are we dealing with (left- or right-handed).

An interesting application exploiting the consequences of the presence of such unusual fluxes was proposed by Pomeau, who proposed a new technique able to separate the two species forming a racemic mixture by applying on the mixture two perpendicular vectorial fields $\vec{F_i}$ and $\vec{F_j}$. In this way one could expect that their application gives rise to a current that will separate the two optical antipodes in a direction perpendicular to the applied forces.

A physical sketch of how such system works is obtained by describing the optical active molecules as Archimedes' screws (with the respective handedness). The size of these screws is supposed to be sufficient large with respect to the solvent's molecules length so that their interaction with the solvent is

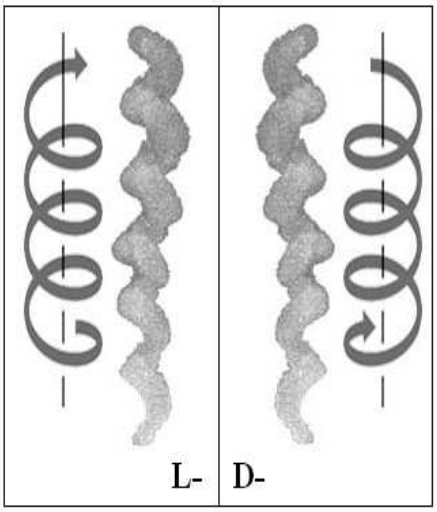

Figure 1.6: Schematization of the motion of the screws with opposite handedness under the action of the electric field.

well described by hydrodynamic laws. Applying a static electric field along the z direction, the screws will begin to rotate around the z axis and the sign of this rotation will depend upon the screws handedness (see figure 1.6). Let's moreover suppose that, under the application of a second thermodynamic force applied along the y direction, the solvent will acquire a mean drift velocity v_y with respect to the optically active molecules.
For the Magnus effect[2] the rotating screws will therefore experience a translational velocity directed along the x axis and whose sign will depend upon the rotation sign and thus upon the optical activity. It is therefore possible to separate in principle the two different species forming the racemic mixture.

Chiral system are thus the ideal systems where the "strange" couplings between vectors and pseudovectors can be observed. The particular chiral system that we will use in this work are **cholesteric liquid crystals** (whose descrip-

[2]Effect consisting in the generation of a sidewise force acting on a spinning cylindrical or spherical solid immersed in a fluid (liquid or gas) when there is relative motion between the spinning body and the fluid. The Magnus effect is responsible for the curve of a served tennis ball or a driven golf ball.

tion will come in the following chapters) because they possess a *macroscopical* chiral structure (because of their long-range helical order) and can make such effects more feasible.

Chapter 2

Liquid crystals

2.1 Soft condensed matter

Matter experiences very different states of aggregation: the most commonly known are solid, liquid and gaseous, each of them characterized by its own well defined assembling rules. In the solid phase (precisely in the crystalline solid one), for example, each atom is locked into a definite location in the crystal lattice, realizing a highly ordered and strongly anisotropic structure. Liquid phase, on the contrary, is very disordered: atoms can freely move within the liquid without being locked into well-defined positions and thus liquid is an isotropic phase.

Between these two phases matter experiences sometimes other states of aggregation, characterized by intermediate properties; one often refers to them as *soft condensed matter* or *soft matter*. We can find matter in such a state of aggregation in everyday life: glues, paints or soaps and so on.

Their peculiarity is that they are *viscoleastic*: they don't posses the stiffness of solids (even though exhibiting some elastic response) nor show the same rheological behavior of liquids. *How* intermediate are such properties will depend from the material. In this work we will deal with **liquid crystals**.

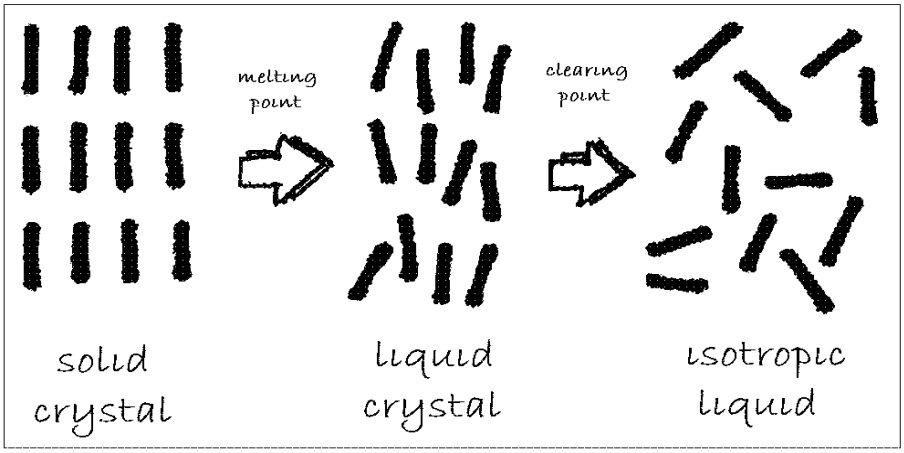

Figure 2.1: Schematic representation of some matter's state of aggregation.

2.2 Liquid crystals (LCs)

Liquid crystals represents an equilibrium phase of matter in which the molecules are arranged with a degree of order that falls inbetween the complete positional disorder of a liquid and the long-ranged, three dimensional order of a crystal. It is worth pointing that this phase differs completely from the partial-crystalline phase, which is a nonequilibrium state of matter in which the system is somehow prevented from reaching its equilibrium state and in which microscopic regions of crystalline order coexist with disordered regions, often forming complex structures. At the beginning of liquid crystal research (at the end of 19. century), Lehmann devoted much of his pioneering work on liquid crystals on persuading other researchers that LCs were not partial cristalline but a completely new phase.
Liquid crystals are found in:

- certain organic compounds with highly anisotropic molecular shapes (rod- or disc-like)
- polymers composed of units having a high degree of rigidity
- polymers or molecular aggregates which form rigid rod-like structures in

solution.

They are very interesting because possess rheological properties analogous to fluids but are birefringent like crystals (with the great difference that the direction of optical axis is not fixed and can vary from point to point within them) and show giant optical nonlinearities. One can figure them like fluids possessing extra internal degrees of freedom.

2.2.1 Classification of the LCs mesophases

The most disordered type of liquid crystalline is surely the **nematic** phase, which has no positional order (the centres of mass of the molecules are arranged like in an isotropic liquid) but in which the molecules are, on the average, oriented about a particular direction. Thus the only kind of ordering that survives in such mesophase is the orientational molecular ordering. The versor describing such direction is often called **molecular director** or **director**:

$$\hat{n}(\theta, \phi) = \Big(\sin\theta\cos\phi, \sin\theta\sin\phi, \cos\theta \Big). \tag{2.2.1}$$

If the molecules of a system in such mesophase are chiral, their centres of mass will be randomly distributed within the fluid but, as a consequence of the microscopical chirality, a structure develops with well defined macroscopical chirality. In these systems there is indeed the tendency for neighboring molecules to align at a slight angle to one another; this weak tendency leads the director to form a helix in space, whose pitch is much longer than the size of a single molecule: thus arises a "transfer" of chirality from the molecules to the whole structure. This phase is called **chiral nematic** or **cholesteric**.

Other liquid crystalline mesophases are more ordered than the two described above: smectic and the columnar phases, for example, will possess also a positional ordering. In what follows we won't pay attention to these other kind of liquid crystals.

2.3 Continuum theory

Although a microscopic approach for studying LC's behavior is available, we will focus our attention on a macroscopic approach exploiting continuum theory's results. Continuum theory offers a powerful tool for a macroscopical description of the behavior of liquid crystals: it provides an expression of their energy which, minimized, will leads to describe equilibrium configuration of the molecular director. It should be noted that the validity of such description hold as long as (a represents the mean molecular size):

$$a \, \nabla \cdot \hat{\boldsymbol{n}} \ll 1 \tag{2.3.2}$$

that is as long as $\hat{\boldsymbol{n}}$'s variations remains lower then the length l over which molecular ordering varies appraisably.

If a system doesn't exchange work with the environment and its temperature and volume remain fixed, the relevant thermodynamical potential becomes Helmholtz free energy $\mathcal{F}$, obtained from system's internal energy $\mathcal{U}$ by mean of a Legendre transform on the canonical variables temperature and entropy $(\mathcal{T}, \mathcal{S})$:

$$\mathcal{F} = \mathcal{U} - \mathcal{T}\mathcal{S}. \tag{2.3.3}$$

The system will reach equilibrium minimizing $\mathcal{F}$. To show that, let's consider an arbitrary isothermal state transform, for which we have:

$$\frac{\mathcal{Q}}{\mathcal{T}} \leq \Delta\mathcal{S}. \tag{2.3.4}$$

Thermodynamic's first principle states that

$$\mathcal{Q} = \Delta\mathcal{U} + L. \tag{2.3.5}$$

We can then write

$$L \leq \mathcal{T} \, \Delta\mathcal{S} - \Delta\mathcal{U} = -\Delta\mathcal{F}. \tag{2.3.6}$$

If our system has $V = \text{cost.}$ and $L = 0$ we have:

$$\Delta\mathcal{F} \leq 0. \tag{2.3.7}$$

The system will thus evolve toward the free energy minimum.

2.3.1 Frank-Oseen elastic energy

In order to give the expression of the free energy density $\mathcal{F} = \mathcal{F}(\hat{\boldsymbol{n}}, \nabla\hat{\boldsymbol{n}})$ associated with LC's distortions we will follow Oseen reasoning [de Gennes (1974); Chandrasekhar (1977); Stewart (2004)]. The energy of a LC sample can be obviously obtained by integrating the free energy density over the whole sample volume:

$$F = \int_V \mathcal{F}(\hat{\boldsymbol{n}}, \nabla\hat{\boldsymbol{n}})\, d^3\vec{x}. \tag{2.3.8}$$

Let's assume the liquid crystal being incompressible. An LC exhibiting a relaxed configuration in the absence of forces acting on it is said to be in a *natural orientation*. The free energy is usually defined to within the addiction of an arbitrary constant: let's choose the value of this constant properly so that $\mathcal{F}(\hat{\boldsymbol{n}}, \nabla\hat{\boldsymbol{n}}) = 0$ for any natural orientation; any other configuration induced upon the sample produces an increasing in the energy, that is:

$$\mathcal{F}(\hat{\boldsymbol{n}}, \nabla\hat{\boldsymbol{n}}) \geq 0. \tag{2.3.9}$$

LCs usually lack polarity: $\hat{\boldsymbol{n}}$ and $-\hat{\boldsymbol{n}}$ are thus physically indistinguishable and it is therefore natural to require that:

$$\mathcal{F}(\hat{\boldsymbol{n}}, \nabla\hat{\boldsymbol{n}}) = \mathcal{F}(-\hat{\boldsymbol{n}}, -\nabla\hat{\boldsymbol{n}}). \tag{2.3.10}$$

Moreover, $\mathcal{F}$ must be frame of reference-independent; defined Q any orthogonal matrix and Q^T its transpose, when $\hat{\boldsymbol{n}} \to Q\,\hat{\boldsymbol{n}}(Q^T\,\vec{r})$, it must hold:

$$\mathcal{F}(\hat{\boldsymbol{n}}, \nabla\hat{\boldsymbol{n}}) = \mathcal{F}(Q\,\hat{\boldsymbol{n}}, Q\,\nabla\hat{\boldsymbol{n}}\,Q^T). \tag{2.3.11}$$

Let's choose our coordinate system with z parallel to the director at the origin, so that:

$$\hat{\boldsymbol{n}}(0,0,0) = (0,0,1). \tag{2.3.12}$$

Small changes Δx, Δy and Δz from the origin in the x,y and z direction will

induce three types of change in the orientation of $\hat{\boldsymbol{n}}(\underline{0})$, leading to six components of curvature, called also curvature strains. In Frank's notation, these "splay", "twist" and "bend" components are:

$$\begin{cases} \text{splay:} & s_1 = \frac{\partial n_x}{\partial x}, \quad s_2 = \frac{\partial n_y}{\partial y} \\ \text{twist:} & t_1 = -\frac{\partial n_y}{\partial x}, \quad t_2 = \frac{\partial n_x}{\partial y} \\ \text{bend:} & b_1 = \frac{\partial n_x}{\partial z}, \quad b_2 = \frac{\partial n_y}{\partial z} \end{cases} \tag{2.3.13}$$

where the components of the director are $\hat{\boldsymbol{n}} = (n_x, n_y, n_z)$ and the terms are evaluated in the origin. A physical representation of what's happening when the system is under the action of such deformations can be viewed in figure 2.2.

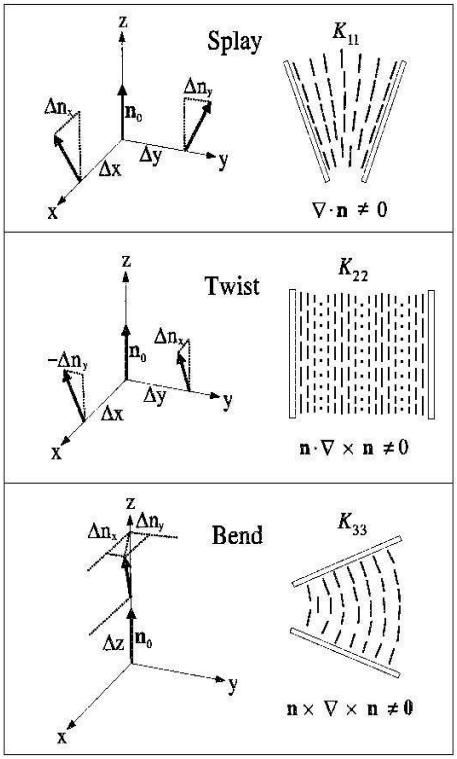

Figure 2.2: Schematic representation of splay, twist and bend deformations acting on LC.

Expanding $\hat{\boldsymbol{n}}$ in a Taylor series round the origin gives (using Einstein summation convention and the convention about $\hat{\boldsymbol{n}}$'s derivatives: $n_{i,j}(\vec{x}) = \partial_{x_j} n_i(\vec{x})$):

$$n_i(\vec{x}) = n_i(\underline{0}) + x_j n_{i,j}\big|_{\vec{x}=\underline{0}} + o(|\vec{x}|^2), \qquad i = 1,2,3 \tag{2.3.14}$$

Keeping in mind the choice of our reference system and that $\hat{\boldsymbol{n}}\cdot\hat{\boldsymbol{n}} = 1$ and thus $0 = \vec{\nabla}(\hat{\boldsymbol{n}}\cdot\hat{\boldsymbol{n}}) = 2\hat{e}_j\, n_i n_{i,j}$, we can write: $n_{z,j}(\underline{0}) = 0$; $\hat{\boldsymbol{n}}$'s series expansion can be therefore rewritten as:

$$\begin{cases} n_x = a_1 x + a_2 y + a_3 z + o(|\vec{x}|^2) \\ \\ n_y = a_4 x + a_5 y + a_6 z + o(|\vec{x}|^2) \\ \\ n_z = 1 + o(|\vec{x}|^2) \end{cases} \tag{2.3.15}$$

where the a_i constants can be related to the others given in expression (2.3.13) by:

$$\begin{cases} a_1 = s_1, \quad a_2 = t_2, \quad a_3 = b_1, \\ \\ a_4 = -t_1, \quad a_5 = s_2 \quad a_6 = b_2 \end{cases} \tag{2.3.16}$$

Let's now expand the free energy density $\mathcal{F}$ with respect to the six curvature strains:

$$\mathcal{F} \simeq k_i a_i + \frac{1}{2} k_{ij}\, a_i a_j, \qquad i,j = 1,2,...,6 \tag{2.3.17}$$

where k_i and k_{ij} are known *curvature elastic constants*; the quadratic terms in (2.3.17) can always be written as a quadratic form where $k_{ij} = k_{ji}$.
Since we are dealing with uniaxial objects, a rotation about the z axis makes no change to the physical description, that is the free energy density should be identical when described with the new curvature strains a_i':

$$\mathcal{F} \simeq k_i a_i' + \frac{1}{2} k_{ij}\, a_i' a_j'. \tag{2.3.18}$$

By making use of such an idea and and cleverly choosing the frame rotation around z-axis, it's possible to show that, of the six k_i only two are independent:

$$\{k_i\} = \{k_1, k_2, 0, 0, -k_2, k_1, 0\} \tag{2.3.19}$$

and that, of the thirty-six k_{ij}, only five are independent:

$$||k_{ij}|| = \left\| \begin{array}{cccccc} k_{11} & k_{12} & 0 & -k_{12} & (k_{11}-k_{22}-k_{24}) & 0 \\ k_{12} & k_{22} & 0 & k_{24} & k_{12} & 0 \\ 0 & 0 & k_{33} & 0 & 0 & 0 \\ -k_{12} & k_{24} & 0 & k_{22} & -k_{12} & 0 \\ (k_{11}-k_{22}-k_{24}) & k_{12} & 0 & -k_{12} & k_{11} & 0 \\ 0 & 0 & 0 & 0 & 0 & k_{33} \end{array} \right\|. \tag{2.3.20}$$

The general form of the free energy density, expressed with Franks curvature strains, will therefore be:

$$\mathcal{F} = k_1(s_1+s_2) + k_2(t_1+t_2) + \frac{1}{2}k_{11}(s_1+s_2)^2 + \frac{1}{2}k_{22}(t_1+t_2)^2 +$$

$$+\frac{1}{2}k_{33}(b_1^2+b_2^2) + k_{12}(s_1+s_2)(t_1+t_2) - (k_2 2 + k_2 4)(s_1 s_2 + t_1 t_2) \tag{2.3.21}$$

Introducing the new constants:

$$s_0 = -\frac{k_1}{k_{11}}, \qquad t_0 = -\frac{k_2}{k_{22}} \tag{2.3.22}$$

and redefining free energy with the addiction of the constant:

$$\mathcal{F}_d = \mathcal{F} + \frac{1}{2}k_{11}s_0^2 + \frac{1}{2}k_{22}t_0^2 \tag{2.3.23}$$

the free energy density can be written in the form:

$$\mathcal{F}_d = \frac{1}{2}k_{11}(s_1+s_2-s_0)^2 + \frac{1}{2}k_{22}(t_1+t_2-t_0)^2 + \frac{1}{2}k_{33}(b_1^2+b_2^2) +$$
$$+k_{12}(s_1+s_2)(t_1+t_2) - (k_{22}+k_{24})(s_1 s_2 + t_1 t_2). \tag{2.3.24}$$

Observing that:

$$\left\{ \begin{array}{rcccl} s_1+s_2 & = & n_{x,x}+n_{y,y} & = & \nabla\cdot\hat{\boldsymbol{n}} \\ -(t_1+t_2) & = & n_{y,x}+n_{x,y} & = & \hat{\boldsymbol{n}}\cdot\nabla\wedge\hat{\boldsymbol{n}} \\ b_1^2+b_2^2 & = & n_{x,x}^2+n_{y,y}^2 & = & (\hat{\boldsymbol{n}}\wedge\nabla\wedge\hat{\boldsymbol{n}})^2 \end{array} \right. \tag{2.3.25}$$

and that

$$-(s_1 s_2 + t_1 t_2) = n_{y,x} n_{x,y} - n_{x,x} n_{y,y} = \frac{1}{2}\nabla\cdot\Big[(\hat{\boldsymbol{n}}\cdot\nabla)\nabla - (\nabla\cdot\hat{\boldsymbol{n}})\hat{\boldsymbol{n}}\Big] \qquad (2.3.26)$$

$\mathcal{F}_d$ can be written in vector notation as:

$$\mathcal{F}_d = \frac{1}{2}k_{11}(\nabla\cdot\hat{\boldsymbol{n}} - s_0)^2 + \frac{1}{2}k_{22}(\hat{\boldsymbol{n}}\cdot\nabla\wedge\hat{\boldsymbol{n}} + t_0)^2 + \frac{1}{2}k_{33}(\hat{\boldsymbol{n}}\wedge\nabla\wedge\hat{\boldsymbol{n}})^2 +$$

$$-k_{12}(\nabla\cdot\hat{\boldsymbol{n}})(\hat{\boldsymbol{n}}\cdot\nabla\wedge\hat{\boldsymbol{n}}) + \frac{1}{2}(k_{22}+k_{24})\nabla\cdot\Big[(\hat{\boldsymbol{n}}\cdot\nabla)\nabla - (\nabla\cdot\hat{\boldsymbol{n}})\hat{\boldsymbol{n}}\Big]. \qquad (2.3.27)$$

The constants k_{11}, k_{22} and k_{33} are said, respectively, *splay*, *twist* and *bend elastic constants*. The combination $(k_{22}+k_{24})$ is called *saddle-splay* constant. It is worth noting that the saddle-splay term is often omitted from the free energy expression since it doesn't contribute to the bulk equilibrium equations because, being a divergence, becomes, when integrated over the whole volume, a surface integral over the boundary. Thus we will omit this term in the forthcoming expression of LC's free energy.

So far we have not jet stated which kind of LC we are dealing with. We have just used the invariance of the free energy with respect to the rotation of the reference frame. There is still another invariance requirement that free energy must satisfy (see eq. (2.3.10)). That can be true only if $k_{12} = 0$ and $s_0 = 0$. Keeping in mind s_0's definition it must also be $k_1 = 0$.

We have now to achieve free energy's definitive expression for nematics and cholesterics exploiting their symmetry properties.

2.3.2 Nematic free energy

Nematic molecules remain alike upon reflection within planes containing the director. Applying a proper transformation of such kind one can easily see that $k_2 = 0$ and thus $t_0 = 0$. Nematic's elastic free energy density will therefore be:

$$\mathcal{F}_d^{(n)} = \frac{1}{2}k_{11}(\nabla\cdot\hat{\boldsymbol{n}})^2 + \frac{1}{2}k_{22}(\hat{\boldsymbol{n}}\cdot\nabla\wedge\hat{\boldsymbol{n}})^2 + \frac{1}{2}k_{33}(\hat{\boldsymbol{n}}\wedge\nabla\wedge\hat{\boldsymbol{n}})^2 \qquad (2.3.28)$$

The three elastic constants are positive and their order of magnitude is $\frac{U}{a} \sim$ $\sim 10^{-6}$dyne (where $U \sim 0.1$eV is the typical molecular interaction energy).

2.3.3 Cholesteric free energy

The molecules constituting cholesterics are chiral and thus their mirror image is different from themselves. Their enantiomorphism has the great consequence of breaking the symmetry under reflection within planes containing the director and therefore $t_0 \neq 0$. The resulting expression for cholesteric free energy is:

$$\mathcal{F}_d^{(c)} = \frac{1}{2}k_{11}(\nabla\cdot\hat{\boldsymbol{n}})^2 + \frac{1}{2}k_{22}(\hat{\boldsymbol{n}}\cdot\nabla\wedge\hat{\boldsymbol{n}} + t_0)^2 + \frac{1}{2}k_{33}(\hat{\boldsymbol{n}}\wedge\nabla\wedge\hat{\boldsymbol{n}})^2 \qquad (2.3.29)$$

2.4 Equilibrium equations

Equilibrium equations for such systems can be derived by making $\mathcal{F}_d$ stationary under the variation of $\hat{\boldsymbol{n}}$ over the unit sphere; the resulting Euler-Lagrange equations are:

$$-\frac{\partial F_d}{\partial n_i} + \partial_j\Big(\frac{\partial F_d}{\partial n_{i,j}}\Big) = -\lambda(\vec{x})n_i \qquad (2.4.30)$$

where $\lambda(\vec{x})$ is a multiplier ensuring the satisfaction of condition $\hat{\boldsymbol{n}}\cdot\hat{\boldsymbol{n}} = 1$. Defining the *molecular field* $\vec{h}^d$ as:

$$h_i^d \equiv -\frac{\partial F_d}{\partial n_i} + \partial_j\Big(\frac{\partial F_d}{\partial n_{i,j}}\Big) \qquad (2.4.31)$$

the Euler-Lagrange equations (2.4.30) will simplify to a parallelism condition, point by point, between director and molecular field:

$$h_i^d = -\lambda(\vec{x})\, n_i. \qquad (2.4.32)$$

Moreover there is another way of obtaining director's equilibrium configuration instead of solving Euler-Lagrange equations. Defining the *elastic torque* $\vec{\tau}_d$ as:

$$\vec{\tau}_d = \hat{\boldsymbol{n}}\wedge\vec{h}^d \qquad (2.4.33)$$

the Euler-Lagrange equations (2.4.30) become:

$$\vec{\tau}_d = \underline{0}. \qquad (2.4.34)$$

An equilibrium configuration will therefore zeroes the elastic torque.

These two procedures are equivalent and they can be used even in the presence of external fields acting on the LC: it is always possible to compute the free energy contribution due to the presence of the external fields, to obtain the relative Euler-Lagrange equations and the consequent equilibrium configuration; alternatively, but equivalently, one can obtain the expression of the external field torque acting on the LC: the equilibrium configuration will be obtained by setting the total torque to zero.

2.5 Boundary effects or anchoring

In discussing the elasticity of nematics and cholesterics one has to pay attention on the point of *how* can one impose a distortion on LCs. The easiest way (that doesn't needs the action of external fields) is forcing the orientation that interfaces (properly prepared) impose on the layer of LCs with whom they are in contact. Any surface will impose his way of ordering on the director of adjacent LC. In most practical cases surface forces at boundaries are much stronger than bulk elastic forces and their effect is enough to impose a well-defined direction to the director $\hat{\boldsymbol{n}}$ at the surfaces. This is the case of *strong* anchoring. The effect of the anchoring, in this case, will be to impose a given direction to the director at boundaries but has not to be taken into account by adding extra free energy terms to the free energy. In the case of *weak* anchoring, instead, one has to take into account both bulk and surface terms in the free energy.
There are two important cases of strong anchoring:

- **homeotropic**: is an alignment perpendicular to the sample surfaces. This kind of anchoring is usually obtained by covering the surface with a surfactant layer.

- **planar**: it forces the molecules to be parallel to the surface. For a free surface any direction in the plane of the surface may be allowed, while for a solid substrate a particular direction in the plane may be imposed by the crystalline structure of the surface. An easy way of imposing a singled direction is obtained just by rubbing a glass surface.

2.6 Nematics and cholesterics equilibrium configurations

From the expression (2.3.28) we can easily see that a nematic LC reaches its *natural* equilibrium configuration when $\mathcal{F}_d^{(n)} = 0$; that happens only when the splay, twist and bend terms are simultaneously equal to zero, that is when $\hat{\boldsymbol{n}}$ remains parallel to itself pointing along the same direction everywhere in the whole sample volume. It is worth noting that free energy minimum leaves undetermined the direction along which the director points: the energy of a nematic "monodomain" is independent of the orientation of the director. Anchoring effects play their important rule right in breaking the symmetry of the nematic phase, imposing their preferential direction to the whole nematic sample.
For cholesteric liquid crystals, the expression of their free energy $\mathcal{F}_d^{(c)}$ is very similar to the nematic one $\mathcal{F}_d^{(n)}$; the effect of the small dissimilarity between them will however imply great differences between the respective equilibrium configurations. From now on, the constant t_0 will be denoted as q_0; for sake of simplicity, let's write $\mathcal{F}_d^{(c)}$ as:

$$\mathcal{F}_d^{(c)} = \frac{1}{2}k_{11}(\nabla\cdot\hat{\boldsymbol{n}})^2 + \frac{1}{2}k_{22}(\hat{\boldsymbol{n}}\cdot\nabla\wedge\hat{\boldsymbol{n}})^2 + \frac{1}{2}k_{33}(\hat{\boldsymbol{n}}\wedge\nabla\wedge\hat{\boldsymbol{n}})^2 + \\ + k_{22}q_0\ \hat{\boldsymbol{n}}\cdot\nabla\wedge\hat{\boldsymbol{n}} + \frac{1}{2}k_{22}q_0^2. \tag{2.6.35}$$

Scaling down the free energy zero point by the constant term $\frac{1}{2}k_{22}q_0^2$, we obtain that cholesteric free energy can be expressed as:

$$\mathcal{F}_d^{(c)} = \mathcal{F}_d^{(n)} + k_{22}q_0\ \hat{\boldsymbol{n}}\cdot\nabla\wedge\hat{\boldsymbol{n}}. \tag{2.6.36}$$

What will be cholesteric equilibrium configuration? We have to minimize again free energy. It is easy to see that, in the *planar distortion* hypothesis (that is $\hat{\boldsymbol{n}}(\vec{x},t) = \hat{\boldsymbol{n}}(z,t)$) and without any constraint at the boundaries, this condition is satisfied if:

$$\begin{cases} \theta(z,t) = \frac{\pi}{2} \\ \\ \phi(z,t) = q_0 z + \phi_0 \end{cases} \tag{2.6.37}$$

that is if the molecules will tend to align along a spiral with *pitch* $p = 2\pi/q_0$ (see figure 2.3).

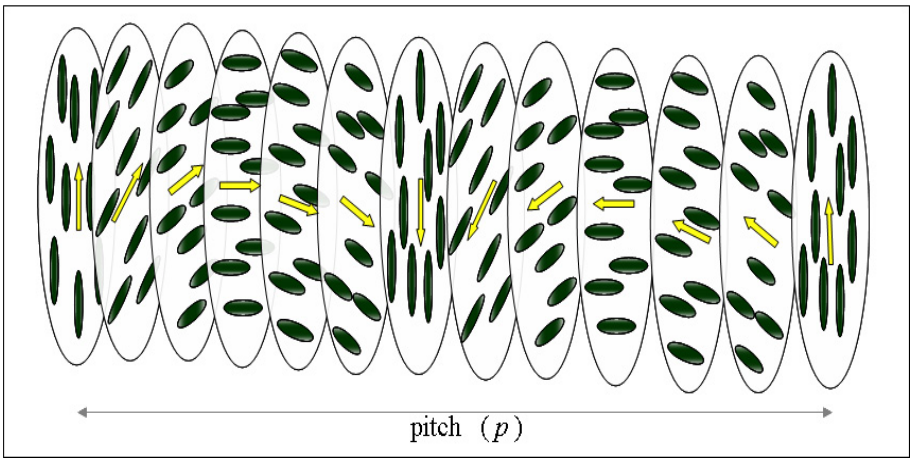

Figure 2.3: Typical molecular arrangement in the cholesteric phase.

2.6.1 Elastic and chiral torques

From now on we will call *elastic torque* the torque derived from nematic free energy:

$$\vec{\tau}_d = \vec{\tau}_d^{(n)} = \hat{\boldsymbol{n}} \wedge \vec{h}^{d,(n)} \tag{2.6.38}$$

where $\vec{h}^{d,(n)}$ is:

$$h_i^{d,(n)} = -\frac{\partial F_d^{(n)}}{\partial n_i} + \partial_j \Big(\frac{\partial F_d^{(n)}}{\partial n_{i,j}} \Big). \tag{2.6.39}$$

Recalling the splay, twist and bend terms in nematic free energy expression, one can compute the relative elastic torques:

$$\begin{cases} \vec{\tau}_d^S = k_{11}\nabla(\nabla\cdot\hat{\boldsymbol{n}}) \\ \\ \vec{\tau}_d^T = -k_{22}\Big[A\,\nabla\wedge\hat{\boldsymbol{n}} + \nabla\wedge(A\,\hat{\boldsymbol{n}})\Big] \qquad \text{where:} \quad \begin{cases} A = \hat{\boldsymbol{n}}\cdot(\nabla\wedge\hat{\boldsymbol{n}}) \\ \vec{B} = \hat{\boldsymbol{n}}\wedge(\nabla\wedge\hat{\boldsymbol{n}}) \end{cases} \\ \\ \vec{\tau}_d^B = k_{33}\Big[\vec{B}\wedge(\nabla\wedge\hat{\boldsymbol{n}}) + \nabla\wedge(\hat{\boldsymbol{n}}\wedge\vec{B})\Big] \end{cases} \tag{2.6.40}$$

obviously their sum gives the total elastic torque:

$$\vec{\tau}_d^S + \vec{\tau}_d^T + \vec{\tau}_d^B = \vec{\tau}_d. \tag{2.6.41}$$

We will call *chiral torque* the torque derived from the term $f_c = $
$= k_{22}q_0\ \hat{\boldsymbol{n}}\cdot\nabla\wedge\hat{\boldsymbol{n}}$:

$$\vec{\tau}_c = \hat{\boldsymbol{n}}\wedge\vec{h}^c \tag{2.6.42}$$

where

$$h_i^c = -\frac{\partial f_c}{\partial n_i} + \partial_j\Big(\frac{\partial f_c}{\partial n_{i,j}}\Big). \tag{2.6.43}$$

The explicit expression of the chiral torque is:

$$\vec{\tau}_c = 2\,k_{22}\,q_0\ (\hat{\boldsymbol{n}}\wedge\nabla\wedge\hat{\boldsymbol{n}}). \tag{2.6.44}$$

2.7 Homeotropic anchoring and frustrated cholesterics

It is interesting to study what happens if one tries to frustrate the cholesteric structure. *Frustration* is the competition between different influences on a physical system that favour incompatible ground states. Cholesterics, for example tend to form twisted structure that could be incompatible with the effect of other agents, such as applied electric or magnetic fields or geometric constraints. One

refers to such cases of *frustrated* cholesterics and often observes the birth of complex ordered structures. One of the most studied case is the cholesteric helix unwinding by mean of an applied magnetic field. A good review of frustrated cholesterics can be found in ref. [Kamien and Seilinger (2001)]. Our interest will be however devoted to another intriguing configuration, occurring when boundaries are treated for homeotropic anchoring; to understand why such configuration is incompatible with the cholesteric structure, one can refer to figure 2.3: the z axis is parallel to the helix axis and the walls lay in planes parallel to the xy plane. Without anchoring conditions the molecules will tend to be parallel to the xy plane as shown in the figure; treating the walls for homeotropic anchoring will force the molecules in contact with the boundaries to be parallel to the z axis and thus to be normal to the plane where they would tend to lay. The question is: would in such case the helix structure survive? To give an answer to this question we have to solve the Euler-Lagrange equations or, alternatively, balancing the total torque with boundary conditions given by homeotropic anchoring.

Let's work again in the plane distortion approximation $\hat{\boldsymbol{n}}(\vec{x},t) = \hat{\boldsymbol{n}}(z,t)$ and let's choose again our frame of reference so that the undistorted state can be written as: $\hat{\boldsymbol{n}}_U = (0,0,1)$. Let's consider a distortion around this state inducing the small variation: $\delta\hat{\boldsymbol{n}}(z,t) = (\delta n_x(z,t), \delta n_y(z,t), 1)$; for the sake of simplicity let's call: $\delta n_x = \xi$ and $\delta n_y = \psi$.
The expression of the free energy in the small distortion approximation will be:

$$\mathcal{F}_d^{(c)} = k_{22}(\psi\ \xi' - \psi'\ \xi) + \frac{1}{2}k_{33}[(\xi')^2 + (\psi')^2] \tag{2.7.45}$$

and the relative Euler-Lagrange equations will be:

$$\begin{cases} 2k_{22}q_0\psi' + k_{33}\xi'' = 0 \\ \\ 2k_{22}q_0\xi' - k_{33}\psi'' = 0 \end{cases} \tag{2.7.46}$$

It s worth noting that, as repeated above, if one computes the elastic and the chiral torque in the same approximations (plane distortion and small distortion), the total torque balance equation will lead to the same equations.

For the sake of simplicity, let's introduce $\zeta = z/d$ (where d is the sample thickness) and let's derive with respect to ζ: $v_\xi = \partial_\zeta \xi = \xi'$ and $v_\psi = \partial_\zeta \psi = \psi'$. Introducing the dimensionless quantity

$$\tilde{q}_0 = \frac{k_{22}}{k_{33}} \frac{q_0 d}{\pi} \tag{2.7.47}$$

the Euler-Lagrange equations will be:

$$\begin{cases} v'_\xi + 2\pi\, \tilde{q}_0\, v_\psi = 0 \\ \\ v'_\psi - 2\pi\, \tilde{q}_0\, v_\xi = 0 \end{cases} \tag{2.7.48}$$

One can easily decouple these equations by deriving them and substituting one into the other; the system will therefore be transformed in:

$$\begin{cases} v''_\xi + (2\pi\, \tilde{q}_0)^2 v'_\xi = 0 \\ \\ v''_\psi + (2\pi\, \tilde{q}_0)^2 v'_\psi = 0 \end{cases} \tag{2.7.49}$$

By integration, one obtains:

$$\begin{cases} v_\xi(\zeta) = A\cos(2\pi\, \tilde{q}_0 \zeta) + B\sin(2\pi\, \tilde{q}_0 \zeta) \\ \\ v_\psi(\zeta) = C\cos(2\pi\, \tilde{q}_0 \zeta) + D\sin(2\pi\, \tilde{q}_0 \zeta) \end{cases} \tag{2.7.50}$$

These solutions have to respect equations (2.7.48): thus $D = A$ and $C = -B$. Integrating them between 0 and ζ with the condition that $\xi(\zeta = 0) = \psi(\zeta = 0) = 0$, we finally obtain:

$$\begin{cases} \xi(\zeta) = \frac{1}{2\pi\, \tilde{q}_0} \Big[A\sin(2\pi\, \tilde{q}_0 \zeta) + B\Big(1 - \cos(2\pi\, \tilde{q}_0 \zeta)\Big) \Big] \\ \\ \psi(\zeta) = \frac{1}{2\pi\, \tilde{q}_0} \Big[A\Big(1 - \cos(2\pi\, \tilde{q}_0 \zeta)\Big) - B\sin(2\pi\, \tilde{q}_0 \zeta) \Big] \end{cases} \tag{2.7.51}$$

Imposing on the other wall of the cell the anchoring condition $\xi(\zeta = 1) =$
$= \psi(\zeta = 1) = 0$, one finally obtains:

$$\begin{cases} A\sin(2\pi\, \tilde{q}_0) + B\Big(1 - \cos(2\pi\, \tilde{q}_0)\Big) = 0 \\ \\ A\Big(1 - \cos(2\pi\, \tilde{q}_0)\Big) - B\sin(2\pi\, \tilde{q}_0) = 0 \end{cases} \tag{2.7.52}$$

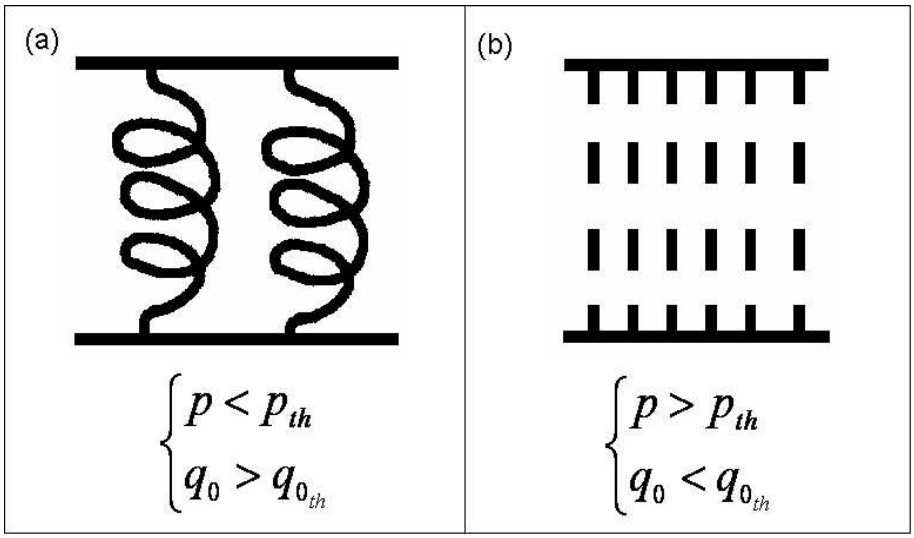

Figure 2.4: Cholesteric liquid crystals samples frustrated by the competition between chiral torque and effect of the homeotropic anchoring.

An homogenous system, in order to possess a nontrivial solution (in this case, twisted structure compatible with homeotropic anchoring on the walls), must possess determinant zero. This brings to the condition:

$$\frac{\sin^2(\pi\tilde{q}_0)}{(\pi\tilde{q}_0)^2} = 0. \tag{2.7.53}$$

We are working in the small distortion approximation and thus we can consider the first zero, that is $\tilde{q}_0 = 1$ or, in terms of q_0:

$$q_{0_{th}} = \frac{k_{33}}{k_{22}}\frac{\pi}{d}. \tag{2.7.54}$$

Remembering the relationship between q_0 and the pitch p, the system has nontrivial solutions when the cholesteric pitch is shorter then the threshold pitch:

$$p_{th} = 2\frac{k_{22}}{k_{33}}d. \tag{2.7.55}$$

So, if the the pitch p is shorter than p_{th}, the chiral torque will be strong enough to overcome the anchoring at the walls and a twisted structure will form; if, on the contrary, the value of the pitch is greater than the threshold value, the system wont't be able to twist, the effect of the anchoring prevails and the

cholesteric sample is forced to behave like a homeotropically aligned nematic one (see figure 2.4).

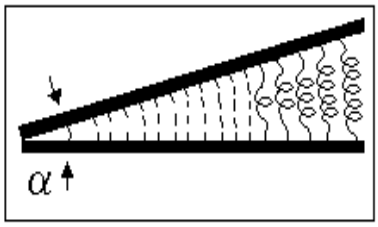

Figure 2.5: Schematic transversal view of a wedge cell.

2.7.1 Cholesteric fingers and fingerprint textures

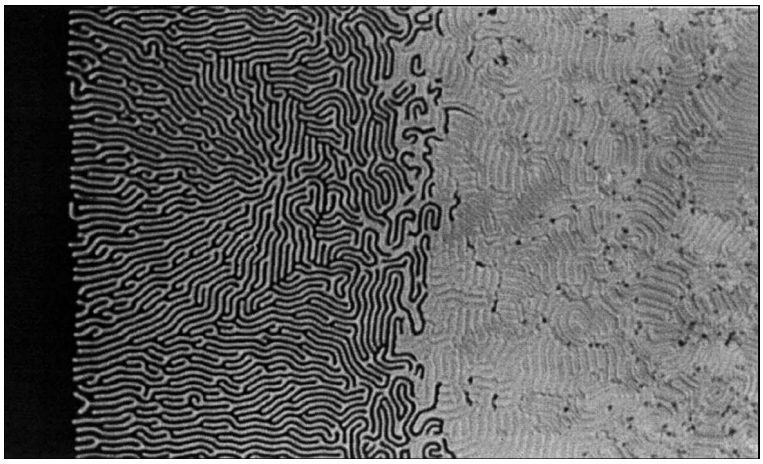

Figure 2.6: View between crossed polarizers of a wedge cell filled with cholesteric LC and whose walls are treated for homeotropic anchoring (after ref. [P. Oswald and Pirkl (2000)]) The dark region is the thinner one, where the anchoring prevails against the chiral torque. Thereafter is the fingerprint texture, where we can observe cholesteric domain surrounded by nematic regions and, finally, on the right is the brightest region, where the cholesteric torque prevails.

Usually people don't handle with chiral LC possessing pitch variable at will. In such cases, if one wants to ensure that the anchoring constraints win the

chiral torque (or succumb), he can exploit the expression of critical pitch value dependence from the sample thickness (eq. (2.7.54) or (2.7.55)). Given a p value, one has to realize a sufficiently thick cell to ensure the helix birth or, on the contrary, one can make sufficiently thin cells to ensure prevailing of the homeotropic anchoring.

Often is useful to work with *wedge* cells, that is cells whose walls, instead of being parallel, are at a slight angle α. As shown in figure 2.5, in such cells one can observe the coexistence of chiral and homeotropic regions, whose extension depends from the value of the *confinement ratio*:

$$C = \frac{d}{p}. \tag{2.7.56}$$

A chiral region surrounded by an homeotropic region is often called *cholesteric finger* and a pattern of cholesteric fingers is called fingerprint texture.

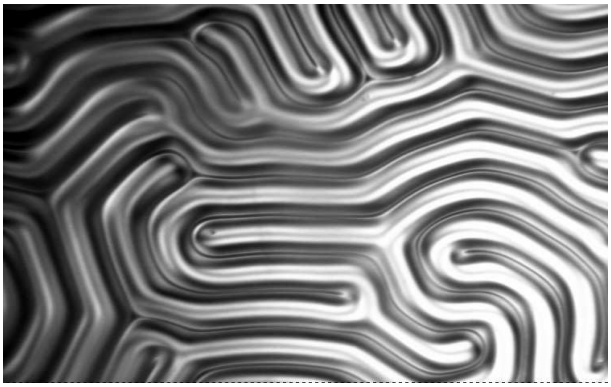

Figure 2.7: View between crossed polarizers of a typical fingerprint texture.

Chapter 3

External fields effect on LC

So far we have considered what happens when we act *mechanically* on LCs. In this chapter we will consider the interaction with external fields (magnetic and electric static fields and optical fields).

3.1 Static fields

3.1.1 Electric field

The application of an electric field $\vec{E}$ to a liquid crystal produces a dipole moment per unit volume called *polarisation* $\vec{P}$. LC's anisotropy generally forces $\vec{E}$ and $\vec{P}$ to have different directions. They are related by mean of the susceptibility tensor $\hat{\chi}_e$ via the equation:

$$\vec{P} = \epsilon_0 \hat{\chi}_e \vec{E} \qquad \text{where:} \qquad \hat{\chi}_e = \begin{vmatrix} \chi_{e\perp} & 0 & 0 \\ 0 & \chi_{e\perp} & 0 \\ 0 & 0 & \chi_{e\parallel} \end{vmatrix} \tag{3.1.1}$$

where ϵ_0 is the permittivity of the free space and $\chi_{e\parallel}$ and $\chi_{e\perp}$ denote, respectively, the susceptibilities parallel and perpendicular to the director.
Introducing the electric displacement vector

$$\vec{D} = \epsilon_0 \vec{E} + \vec{P} \tag{3.1.2}$$

and the dielectric tensor

$$\hat{\epsilon} = \begin{vmatrix} \epsilon_{e\perp} & 0 & 0 \\ 0 & \epsilon_{e\perp} & 0 \\ 0 & 0 & \epsilon_{e\parallel} \end{vmatrix} \tag{3.1.3}$$

where $\epsilon_{e\parallel} = 1 + \chi_{e\parallel}$ and $\epsilon_{e\perp} = 1 + \chi_{e\perp}$ and the *dielectric anisotropy* ϵ_a is $\epsilon_a = \epsilon_\parallel - \epsilon_\perp$, the general expression for the electric displacement is:

$$\vec{D} = \epsilon_0 \epsilon_\perp \vec{E} + \epsilon_0 \epsilon_a (\hat{\boldsymbol{n}} \cdot \vec{E}) \hat{\boldsymbol{n}}. \tag{3.1.4}$$

The total electric energy will therefore be:

$$w_E = -\frac{1}{2} \vec{D} \cdot \vec{E} = -\frac{1}{2} \epsilon_0 \epsilon_\perp |\vec{E}|^2 - \frac{1}{2} \epsilon_0 \epsilon_a (\hat{\boldsymbol{n}} \cdot \vec{E})^2. \tag{3.1.5}$$

Because the first term is independent of the orientation of $\hat{\boldsymbol{n}}$, it will usually omitted from the energy expression, which then reduces to:

$$w_E = -\frac{1}{2} \epsilon_0 \, \epsilon_a (\hat{\boldsymbol{n}} \cdot \vec{E})^2. \tag{3.1.6}$$

When $\epsilon_a > 0$ the energy is minimized when $\hat{\boldsymbol{n}}$ and $\vec{E}$ are parallel while, when $\epsilon_a < 0$, when they are perpendicular. In this work we made use of materials with positive dielectric anisotropy. An applied electric field will thus tend to align the director along its direction.

The expression of the electric torque is:

$$\vec{\tau}_E = \frac{\epsilon_a}{4\pi} (\hat{\boldsymbol{n}} \cdot \vec{E}) \Big(\hat{\boldsymbol{n}} \wedge \vec{E} \Big) \tag{3.1.7}$$

3.1.2 Magnetic field

The application of a magnetic field $\vec{H}$ across a LC sample induces a magnetization $\vec{M}$ in the liquid crystal due to the weak magnetic dipole moments imposed upon the molecular alignment by the magnetic field. Similarly to the case of the electric field, the general magnetization expression is:

$$\vec{M} = \chi_\perp \vec{H} + (\chi_\parallel - \chi_\perp) \Big(\hat{\boldsymbol{n}} \cdot \vec{H} \Big) \hat{\boldsymbol{n}} \tag{3.1.8}$$

where $\chi_\parallel$ and $\chi_\perp$ are the diamagnetic susceptibilities when the field and the director are, respectively, parallel and perpendicular.

The magnetic induction can be expressed as:

$$\vec{B} = \mu_0 \, \mu_\perp \vec{H} + \mu_0 \chi_a \Big(\hat{\boldsymbol{n}} \cdot \vec{H} \Big) \hat{\boldsymbol{n}} \tag{3.1.9}$$

where $\chi_a = \chi_\parallel - \chi_\perp$ is called the *magnetic anisotropy* and is generally very small compared to ϵ_a (in the SI its order of magnitude is 10^{-6} while $\epsilon_a \sim 1$).

The total magnetic energy will be:

$$w_H = -\frac{1}{2} \vec{B} \cdot \vec{H} = -\frac{1}{2} \mu_0 \mu_\perp |\vec{H}|^2 - \frac{1}{2} \mu_0 \mu_a (\hat{\boldsymbol{n}} \cdot \vec{H})^2. \tag{3.1.10}$$

Because the first term is independent of the orientation of $\hat{\boldsymbol{n}}$, it is usually omitted from the energy expression, which then reduces to:

$$w_H = -\frac{1}{2} \mu_0 \, \mu_a (\hat{\boldsymbol{n}} \cdot \vec{H})^2. \tag{3.1.11}$$

When $\mu_a > 0$ the energy is minimized when $\hat{\boldsymbol{n}}$ and $\vec{H}$ are parallel while, when $\mu_a < 0$, when they are perpendicular.

The expression of the magnetic torque is:

$$\vec{\tau}_H = \chi_a (\hat{\boldsymbol{n}} \cdot \vec{H}) \Big(\hat{\boldsymbol{n}} \wedge \vec{H} \Big) \tag{3.1.12}$$

3.2 Optical fields

Let's consider an electromagnetic monochromatic wave at frequency ω in the optical range impinging on the LC sample. The expressions of the real fields impinging on the sample are:

$$\begin{cases} \vec{E}_{\text{real}}(t) = \frac{1}{2} \Big(\vec{E} e^{-\imath \omega t} + \vec{E}^* e^{\imath \omega t} \Big) \\ \\ \vec{D}_{\text{real}}(t) = \frac{1}{2} \Big(\vec{D} e^{-\imath \omega t} + \vec{D}^* e^{\imath \omega t} \Big) \end{cases} \tag{3.2.13}$$

The electromagnetic energy $\mathcal{U}$ will be an oscillating function with respect to the time. Its average value over the optical period π/ω is:

$$w_o = \langle \mathcal{U} \rangle = \frac{1}{16\pi} \Big(\vec{D}^* \cdot \vec{E} + \vec{B}^* \cdot \vec{H} \Big). \tag{3.2.14}$$

Remembering that the magnetic effects are usually negligible with respect to the electric one, the optical energy expression will be:

$$w_o = -\frac{1}{16\pi}\epsilon_\perp |\vec{E}|^2 - \frac{1}{16\pi}\epsilon_a |\hat{\boldsymbol{n}}\cdot\vec{E}|^2. \tag{3.2.15}$$

Again, the first term is not affected from the director orientation and can be therefore omitted. Then, the expression of the optical energy reduces to:

$$w_o = -\frac{1}{16\pi}\epsilon_a |\hat{\boldsymbol{n}}\cdot\vec{E}|^2. \tag{3.2.16}$$

The relative optical torque is:

$$\tau_o = \frac{\epsilon_a}{8\pi}\mathrm{Re}\Big[(\hat{\boldsymbol{n}}\cdot\vec{E}^*)\Big(\hat{\boldsymbol{n}}\wedge\vec{E}\Big)\Big] \tag{3.2.17}$$

The field $\vec{E}$ is relative to the complex wave at a given point and it is not the amplitude of the impinging wave. How such amplitudes are related to the torque (3.2.17) can be computed by mean of the Maxwell equations.

It is worth noting that, although the formal expression of the optical torque resembles very closely the expression of the static electric torque, the two interaction processes are very different. Static fields are usually applied on the whole sample while the optical field consists of a laser beam impinging on the sample and whose transversal dimensions are much smaller than the cell walls extension. Thus we have to take in account the transverse effect arising when the optical fields interact with LCs (see section 3.3.2). Moreover, light has a vector character, as described by its polarization state. LC are being birefringent materials, are very sensitive to the light polarization state, yielding to reorientation effects having no analogue in the static electric field case.

3.3 Fréedericksz effect

One of the most known and exploited effects in the wide multitude of phenomena occurring in LCs is the Fréedericksz effect, that can be induced by a static electric or magnetic field [Fréedericksz and Zolina (1933)] or by an optical field [Zolot'ko et al. (1980); Durbin et al. (1981); Zel'dovich and Tabiryan (1982)].
To describe briefly this phenomenology, let's refer to figure 3.1: a nematic LC

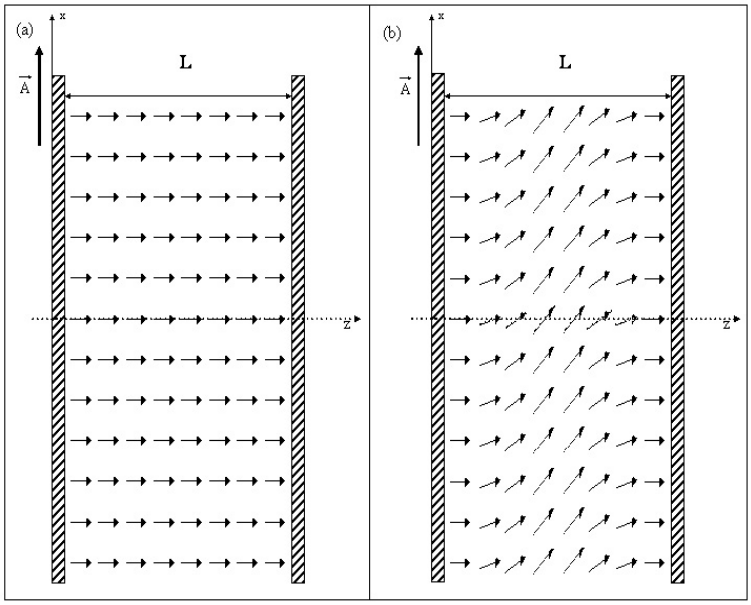

Figure 3.1: Fréedericksz effect generated by a static (electric or magnetic) field $\vec{A}$: (a) if ($|\vec{A}| < |\vec{A}_{th}|$) the field not affect the sample, that remains undistorted, while (b) if the field intensity exceeds a threshold value ($|\vec{A}| > |\vec{A}_{th}|$) the sample will be distorted.

sample is treated for homeotropic anchoring. Let the z axis be the axis along which the molecules are aligned and let us apply a static field $\vec{A}$ (electric or magnetic) along the x axis. The torque induced into the sample is:

$$\vec{\tau}_A = \frac{\Delta a}{4\pi}(\hat{\boldsymbol{n}}\cdot\vec{A}\,)\Big(\hat{\boldsymbol{n}}\wedge\vec{A}\Big) \tag{3.3.18}$$

where Δa is the opportune anisotropy (dielectric or magnetic, depending from the nature of $\vec{A}$). In this configuration ($\hat{\boldsymbol{n}}\perp\vec{A}$) the torque is zero and $\vec{A}$ doesn't affect the sample. But, if the director would experience slight thermal fluctuations, then it would experience a nonzero torque due to the presence of $\vec{A}$. However, if the intensity of the applied field won't be high enough, the contrasting elastic torque $\vec{\tau}_d$ will prevail, damping the fluctuations and forcing the sample to the undistorted state. On the contrary, if the applied field is above a critical threshold value, the sample will experience a Fréedericksz transition, and the sample will reach a distorted equilibrium state, as shown in figure 3.1-(b).

3.3.1 Optical Fréedericksz Transition (O.F.T.)

The situation is quite different when the transition is induced by an optical field. As mentioned above, a laser beam has a finite spatial extension ($\simeq 100\mu$m) (see figure 3.2). Moreover, LCs are sensitive to the light polarization: the OFT will therefore change its character drastically with respect to the impinging light polarization. The analysis of the optical reorientation of LC will thus be a highly complex nonlinear problem: the nature of the OFT depends upon the light polarization state, that, in its turn, depends upon the local birefringence of the medium. The cause becomes the effect, the effect becomes the cause again and so on till an equilibrium condition is reached that, in principle, could even not exist. In the last case, we observe the rising of dynamical regimes (often complex).

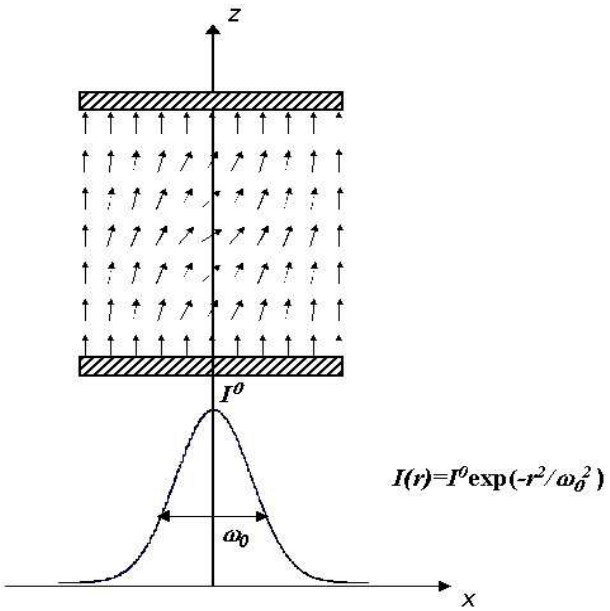

Figure 3.2: Reorientation profile induced by a laser beam with transverse gaussian profile in a nematic sample homeotropically aligned.

3.3.2 Transverse effects

The OFT, as mentioned above, induces inhomogeneity in the molecular response because the sample is not uniformly subjected to the same field. Thus, the illuminated molecules will experience the optical torque and will reorientate; contemporary, during their reorientational process, they will exert an elastic torque on their not illuminated neighbours, that couldn't otherwise reorient, creating a strong transversal correlation within the crystal. Another consequence of the finite beam size and inhomogeneous exposure to the optical field is the rising of the threshold value for the OFT.

Self-phase modulation

One of the most spectacular effects arising in the OFT is the self-phase modulation. When a laser beam traverses an LC slab, one observes in the far field

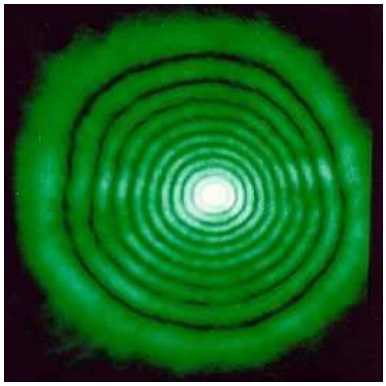

Figure 3.3: Picture of a typical far field diffraction ring pattern due to the self-phase modulation in LCs.

a series of concentric rings diverging very rapidly. Figure 3.3 shows a typical self-diffraction rings pattern. A rigorous mathematical treatment of such phenomenon can be found in [Santamato and Shen (1985)]. It can be shown that the rings number, related to the phase difference accumulated between ordinary and extraordinary wave travelling through the cell, is strictly related to the reorientational amplitude (supposed to be, like the impinging laser profile,

gaussian) at the centre of the reorientation profile:

$$\mathcal{N} \propto \theta^2(\vec{r} = 0). \tag{3.3.19}$$

Exploiting such considerations it is thus possible to measure the ring number and to obtain the amplitude of the reorientational profile.

3.4 S.I.S.L.S.

S.I.S.L.S. is the acronym for self-induced stimulated light scattering and occurs when a circularly polarized laser beam impinges normally to a nematic slab treated for homeotropic alignment. Theoretical and experimental studies of such effect can be found in references [Santamato et al. (1986, 1987, 1988)].

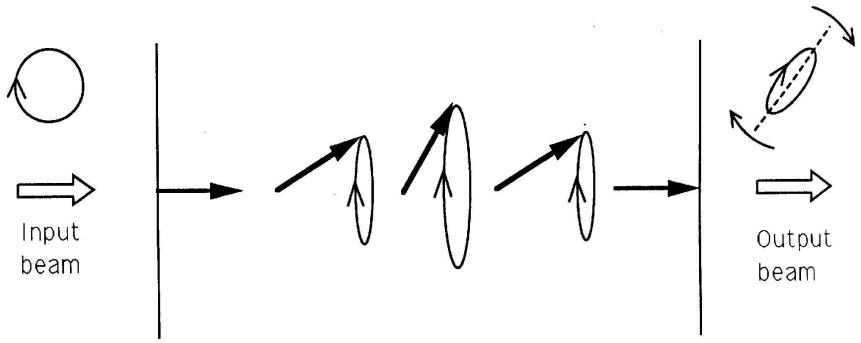

Figure 3.4: Schematic representation of director's rotation induced from a circularly polarized laser beam.

In figure 3.4 is shown a schematic sketch of the SISLS process. If the impinging beam possesses an intensity beyond the Fréedericksz threshold value, $\hat{\boldsymbol{n}}$ reorientates (along a direction ϕ depending from system's residual anisotropies) and the cell becomes birefringent. The radiation, traversing the birefringent medium, changes its polarization state and, thus, photons release part of their spin angular momentum to the medium. The amount of exchanged spin angular

momentum can be expressed as[1]:

$$\Delta s_3 = \frac{I(e_{in} - e_{out})}{\omega} \tag{3.4.20}$$

where e represents the ellipticity of the polarization ellipse. LCs molecules will thus be put in rotation and the birefringence axes will begin to rotate.

Self-induced stimulated light scattering is a nondestructive process because the photon is scattered from the medium (not absorbed), releasing part of its energy and angular momentum to it. Said ω and J_z frequency and angular momentum[2] of the impinging light and ω' and $J_z{}'$ the frequency and angular momentum after the scattering process, the medium will become from the diffused photon $\hbar(\omega' - \omega)$ energy and $(J_z{}' - J_z)$ angular momentum. It is thus transferred to the body the difference of photon's energy and angular momentum.
The rotational energy transferred to the body is dissipated through the viscous forces and induces into the scattered photon a red-shift $\Delta\omega = 2\Omega$ (where Ω is the angular velocity induced in the body). This effect was experimentally observed [Santamato et al. (1987)].

3.5 O.F.T. in cholesterics

A review of the peculiarities of the OFT in cholesteric liquid crystal can be found in [Abbate et al. (1996)] and in the references there cited.
The phenomenology of this reorientation process is very particular. Let's begin by considering the case of linearly polarized light (see figure 3.5). When the laser intensity goes over the Fréedericksz threshold ($\tilde{I}_1$ in figure) the system reaches the so called Optical Phase Locked (OPL) regime: the sample is "locked" in a low birefringence state for a wide range of intensities; after a second threshold $\tilde{I}_2$ the system jumps abruptly to a highly distorted state. Decreasing the laser intensity below $\tilde{I}_2$, the system, instead of turning back to the low birefringence

[1] It should be taken in account that light possesses both spin and orbital angular momentum and how to decompose light's total angular momentum into the spin and the orbital part, but in the geometry of our experimental setup (laser beam with circular transverse profile) the light doesn't carry orbital angular momentum nor can exchange it with LCs; thus the observed effects can be ascribed exclusively to the light's spin transfer.

[2] We use J_z for denoting light's *total* angular momentum.

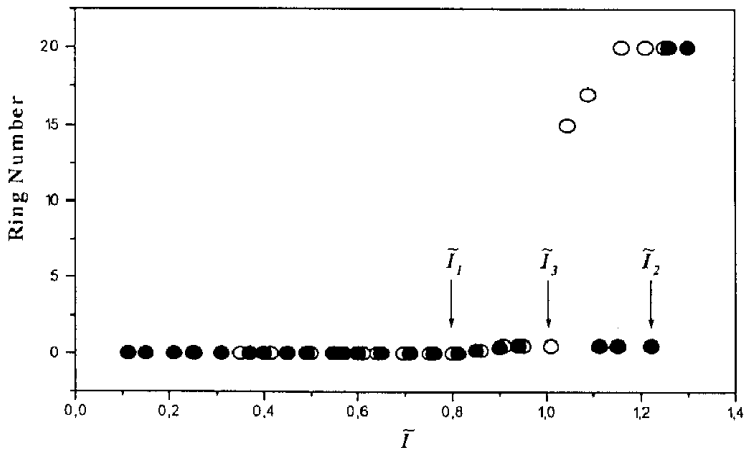

Figure 3.5: Ring number versus laser intensity for a cholesteric sample illuminated with linearly polarized light (after [Abbate et al. (1996)]). Series • : obtained increasing the laser intensity - series ∘ : obtained decreasing the laser intensity.

OPL state, shows an hysteretic behavior remaining in the highly distorted state till a third threshold $\tilde{I}_3$.
The presence of the optical phase-locked state and the occurrence of the bistability without the action of external elements is a very unusual characteristic of cholesterics (nematic don't show such features); they arise because of the competition between the helical structure induced by the chiral torque and the homeotropic anchoring conditions imposed at the sample boundary.

To explain the observed "locked" behavior that, for a wide range of intensities prevents the formation of rings in the far field, in [Abbate et al. (1996)] the authors suppose that the excess energy put into the sample by the laser beam, instead of increasing the sample birefringence (raising the rings number), is stored in the twist degree of freedom. If this were the case, a rotation of the polarization plane should be present in the plane beyond the sample, because of Mauguin's theorem [Mauguin (1911)]. The phase retardation induced into the sample is frozen to the value $\delta \sim \pi$ and the sample should behave as a retarder plate $\lambda/2$, rotating the polarization's direction. In the forthcoming chapters of

this work it will be given an experimental proof that this picture is true.

When the imping light is circularly polarized the sample, as a consequence of the cholesteric helical structure with its well defined helicity, behaves differently under left- or right-handed circularly polarized light, depending from whether light and helix helicity are equiversal or not.

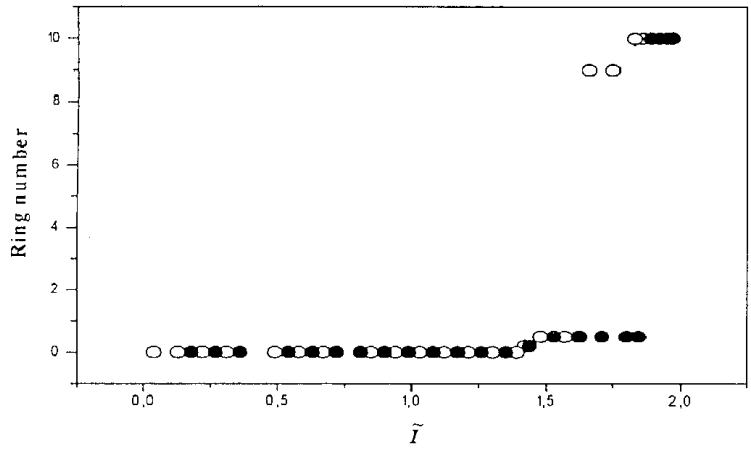

Figure 3.6: Ring number versus laser intensity for a cholesteric sample illuminated with circularly polarized light with helicity opposite with respect to the cholesteric helical sense (after [Abbate et al. (1996)]). Series • : obtained increasing the laser intensity - series ∘ : obtained decreasing the laser intensity.

We have thus to consider the two cases separately:

- **Same helicity**

  When the helicity of light and the chiral torque are the same it is possible observed the double threshold feature (OPL and highly distorted state) and the hysteresis loop (see figure 3.6).

- **Opposite helicity**

  When the helicity of light and the chiral torque are in contrast the OPL and hysteresis loop disappear, as shown in figure 3.7.

In the work [Maddalena et al. (1995)] and in the very recent work [Brasselet et al. (2005)] numerical simulations are performed in which it is foreseen that,

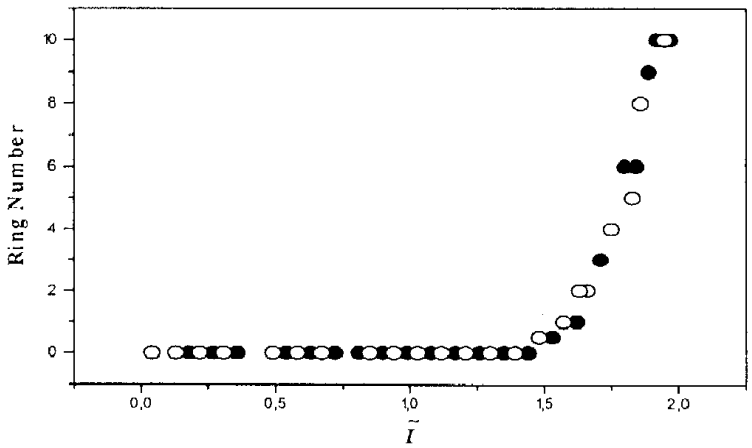

Figure 3.7: Ring number versus laser intensity for a cholesteric sample illuminated with circularly polarized light with helicity concordant with respect to the cholesteric helical sense (after [Abbate et al. (1996)]). Series • : obtained increasing the laser intensity - series ○ : obtained decreasing the laser intensity.

under particular conditions depending from the helical pitch p, the confinement ratio (defined in eq. (2.7.56)) and the helicity of light, it is expected that the director *rotates* (precesses or nutates). In this work will be given, among other effects, the first experimental observation of the rotation in cholesteric samples under the action of circularly polarized light.

It is important to point out that the works cited above were developed within the plane wave approximation, where all relevant parameters are assumed to depend on one spatial coordinate (z) and the time (t). The validity of such approximation will be discussed later by confronting the experimental acquisitions with predictions of a newly developed model in three-dimensions.

Chapter 4

Lehmann effect and unusual couplings in cholesterics

At the beginning of the research on LCs, the German physicist O. Lehmann published a work [Lehmann (1900)] on which he reported his big amount of observations about the behavior of a strange, almost unknown at the time, matter's state of aggregation, shoch is known, today, as the cholesteric phase. Amongst these observations, he reported the rotation of cholesteric drops subjected to a thermal gradient parallel to the axis of the helical structure. From polarimetric considerations, he argued that the *structure* rather that the drop itself was put in rotation by the heat flux.

The peculiarity of this phenomenon, making it so intriguing, is that the drop reacts to the applied thermal gradient, which is a **polar** vector, generating a torque (that induces the rotation of the drop in the plane xy orthogonal to the applied gradient), which is an **axial** vector. Such couplings are, as pointed out in chapter 1, usually forbidden in normal structures but are allowed in parity-breaking structures, as in the case of cholesterics. Such effect is thus strictly related to the *geometric* structural properties of the considered material (i.e. the macroscopic chiral structure of cholesteric LCs).

Many experiments have been executed since Lehmann's first observation but no one has been able to replicate an analogous rotation in a clear and unambiguous way, discriminating cross-couplings effects (arising only in chiral structures)

from effects with different origin. In the next sections a short review will be given on the principal efforts done to investigate Lehmann-like phenomena.

4.1 Dynamic continuum theory results for cholesterics

Formulating a dynamic continuum theory for liquid crystals is a very hard work because LCs possess, unlike ordinary fluids, internal orientational degree of freedom (the director); thus orientational dynamic and its interconnection with the fluid motion has to be taken in account.
Leslie [Leslie (1969)] developed the continuum theory for cholesterics and showed [Leslie (1968, 1971)] the existence of Lehmann-like solutions. The dynamic continuum theory won't be exposed in this work and we'll refer to Leslie's work or classical textbooks (as, for example, [de Gennes (1974)]) for it. At last, a very brief but exhaustive summary of the equations needed to study Lehmann's rotation can be find in reference [Shahinpoor (1976)].

From a physical point of view, we can follow Leslie reasoning for understanding *why* do such strange coupling work for cholesterics. Cholesterics, unlike nematics, possess a nonuniform configuration (the helical structure). So, even if they are subjected to a uniform solicitation like a uniform thermal gradient, they will react, because of their structural properties, in a nonuniform way to the applied field, leading , generally, to flow of the fluid and distortion of the orientation pattern. If the applied field is parallel to the helical axis, the material will be at rest and the torque acting on the director seeks to rotate the director uniformly around the helix axis. If there is no external balancing torque (for example, the boundaries are free), the helix simply rotates with uniform angular velocity about its axis. This situation resembles the paper spirals that, put on heat sources, begin to rotate steadily under the action of the ascending air currents.

4.1.1 Lehmann-like effect equation:

It can be shown that the director dynamics in a cholesteric is described by [Gil and Gilli (1998)]:

$$\gamma_1 \frac{\partial \hat{\boldsymbol{n}}}{\partial t} = \vec{h}(\hat{\boldsymbol{n}}) + \nu_E \, \hat{\boldsymbol{n}} \wedge \vec{E} \tag{4.1.1}$$

where $\vec{h}(\hat{\boldsymbol{n}})$ is the molecular field (free energy's lagrangian derivative, already defined in section 2.4), γ_1 is the rotational viscosity coefficient[1] and the coefficient ν_E is said to be, respectively, chemico-, thermo- or electro-mechanical coupling coefficient, depending from the choice of the field $\vec{E}$ between the chemical potential gradient, the thermal gradient or the electric field .

In a configuration resembling the Lehmann effect configuration, that is when the applied field is parallel to the helix axis, and in the planar deformation hypothesis ($\hat{\boldsymbol{n}}(\vec{x}, t) = \hat{\boldsymbol{n}}(z, t)$) such equation simplifies to:

$$\gamma_1 \frac{\partial \varphi}{\partial t} = k_{22} \frac{\partial^2 \varphi}{\partial \, z^2} - \nu_E \, E \tag{4.1.2}$$

We'll consider two important solutions classes for this equation, corresponding to two different boundary conditions: (a) stress free boundaries or (b) planar anchoring.

- (a) **stress free boundaries:**

  When boundaries impose no constraints to the sample the solution of the equation (4.1.2) takes the form:

  $$\varphi(z, t) = q_0 z - \frac{\nu_E E}{\gamma_1} \, t + \text{cost.} \tag{4.1.3}$$

  which represents an helix with pitch q_0 (the natural pitch) and that rotates rigidly with angular velocity depending from the intensity of the applied field, the coupling coefficient and the viscosity coefficient:

  $$\omega = -\frac{\nu_E \, E}{\gamma_1}. \tag{4.1.4}$$

  The rotational velocity is thus independent from the pitch of the sample and depends linearly from the applied field (reverses its sign reversing the sign of the field) and from the coupling coefficient. **This solution represents the Lehmann-like rotatory solution.**

[1] For a proper classification of the viscosity coefficients appearing in LC dynamic see ref. [Stewart (2004)], chapter 4.

- (b) **planar anchoring:**
  When the walls are treated for planar anchoring, forcing the director to lay, for example, along the x-axis at the first wall ($z = 0$) and along the direction $\varphi_{_D}$ at the other wall ($z = D$), the solution of the equation (4.1.2) takes the form:
  $$\varphi(z,t) = \frac{\varphi_{_D}}{D} z - \frac{\nu_E E}{k_{22}} z(D - z) \tag{4.1.5}$$
  which represents, in the absence of the applied field $\vec{E}$, a uniformed twisted structure (whose pitch depends from the anchoring conditions and is thus different from the unperturbed one q_0). The application of the field will induce inhomogeneities in the twist.

Two kind of experiments were performed about cross-couplings in cholesterics: measure of the coupling coefficients (the thermo-mechanical and the electro-mechanical coupling coefficient) and a search for Lehmann-like rotations. In the next sections we will give a brief review of the principal efforts done in those directions.

4.2 Measure of the thermo-mechanical coupling coefficient

A first experimental attempt in measuring the thermo-mechanical coupling coefficient was made by Jánossy's group [Éber and Jánossy (1982, 1984)]. The experimental setup realized in these works is shown in figure 4.1.

In such a configuration the thermal gradient induces a distortion in the director field. A laser traverses the sample along the z direction. The phase difference between ordinary and extraordinary waves at the sample exit has expression:
$$\Delta\phi = \frac{\pi}{120} \frac{L^5}{\lambda} \frac{n_o(n_e^2 - n_o^2)}{n_e^2} \frac{\lambda_{\text{eff}}^2}{k_{33}^2} \Big(\frac{\partial T}{\partial x}\Big)^2 \tag{4.2.6}$$
and is thus related to the *effective* thermo-mechanical coupling coefficient λ_{eff}, related to the thermo-mechanical coupling (λ_3 in Jánossy notation) by means of the relation:
$$\lambda_{\text{eff}} = \lambda_3 + k_{22} \frac{dq_0}{dT} \tag{4.2.7}$$

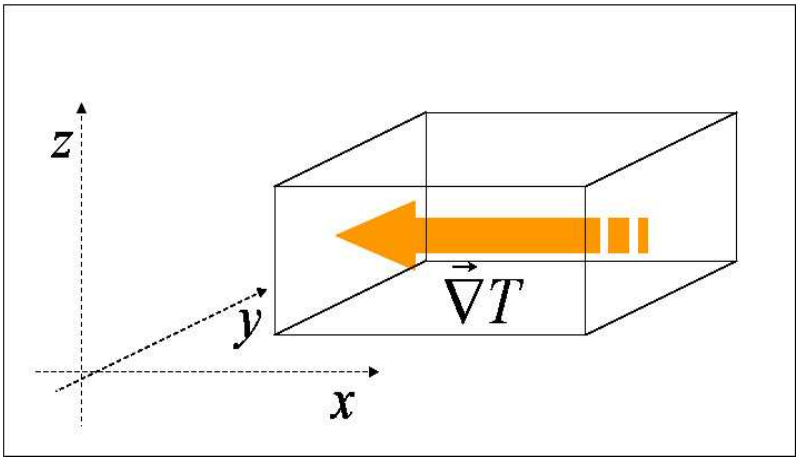

Figure 4.1: Schematic representation of the experimental geometry adopted in [Éber and Jánossy (1982, 1984)]. The sample boundaries (lying in the xy plane) are treated for planar anchoring. The thermal gradient is applied parallel to the x axis.

The estimated value for the thermo-mechanical coupling coefficient was:

$$\frac{\lambda_3}{k_{33}} = 4 * 10^4 \ {}^oC^{-1}m^{-1} \tag{4.2.8}$$

4.3 Measure of the electro-mechanical coupling coefficient

The effort of measuring the electro-mechanical coupling coefficient was performed by the group of Madhusudana in two types of experiments [Madhusudana and Pratibha (1989); Madhusudana et al. (1991)]. In one experiment, following Jánossy's footsteps, they realize a distorted configuration (cell walls treated for planar alignment) while the other experiment is performed on cholesteric drops, resembling Lehmann's original configuration.

4.3.1 Profile distortion in planar cells

In this experiment [Madhusudana et al. (1991)], a sample is prepared, as in Jánossy's experiment, planarly aligned. The difference with Jánossy's experimental setup is that, in this configuration, the electric field is applied parallel to the helix axis (see figure 4.2).

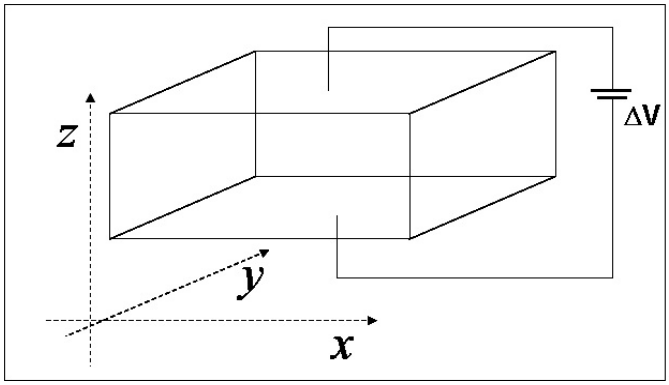

Figure 4.2: In this experimental configuration the applied field is parallel to the helix axis.

The director configuration is then described by eq. (4.1.2); the application of the electric field twists inhomogeneously the structure; the idea of these experiment is to apply a low frequency AC electric field and to observe the azimuthal profile's oscillations due to the electric field's sign inversion.

4.3.2 Rotation of cholesteric drops

In this experiment [Madhusudana and Pratibha (1989)] an opportune mixture of cholesteric drops suspended in its own isotropic phase is prepared. Such drops are successively put under glasses and flattened, paying attention that the drops were surrounded by the isotropic environment and not in contact with the glasses (to ensure the condition stress free boundary required to obtain rotating solutions like those given by eq. (4.1.3)), as shown in figure 4.3; a DC electric field was then applied to the sample.

The drop radius is much greater than the sample thickness ($\delta \gg d$) and the

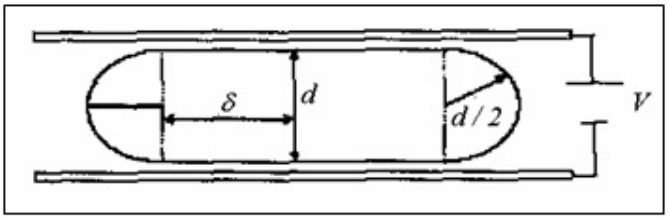

Figure 4.3: A cholesteric drop of radius$\sim \delta$ flattened between glasses at a distance d.

cholesteric pitch is of the order of magnitude of the cell thickness. Typical values for this experiment are: $d \simeq p \simeq 5\mu$m and $\delta \simeq 50\mu$m. Put the drop under crossed polarizers, they observed the χ defect line and the rotation of the dark and bright brushes around it to deduce the rotational velocity of the director.

The value of the electro-mechanical coefficient obtained in these experiments was:

$$\nu_{\vec{E}} \simeq -0.6 * 10^{-12} Jm^{-1} \tag{4.3.9}$$

4.3.3 Is this *really* a Lehmann-like rotation?

Although in Madhusudana's experiment is observed the rotation of drops under an applied electric field, the question is: are such rotations of the Lehmann-like type? That is, are these rotation exclusively adducible to the cross-couplings? As suggested in ref. [Tarasov et al. (2003a,b)], this is not the case. Lehmann-like rotations should arise in situations in which the only contributing factor is the applied polar vector and that can happen, for example, in a geometry in which the applied field is parallel to the helix axis. This is unfortunately not the situation of the flattened cholesteric drops experiment. The topology of a cholesteric drop is very complicated and surely is not a sequence of cholesteric planes forming the usual helix. Moreover, the drops are *flattened*, complicating the topology of the system (remember that the natural cholesteric pitch order of magnitude is comparable to the cell thickness while the radial extension of the drops is one order of magnitude greater).

Inside a flattened cholesteric drop, the splay-bend deformation of the cholesteric layers is significant and, thus, the flexoelectric[2] contribution to the dynamics of the drop must be considered. Moreover in presence of defects -and this is the case, indeed- the splay-bend deformation is further enlarged and the flexoelectric contribution becomes even more stronger.

The interpretation of the experimental observations concerning flattened drops and cross-coupling phenomena driven by the electric field is thus unsatisfactory and the separation between the effects caused by the cross-couplings and effect of other nature is not clear. This configuration is thus unable for observing cross-coupling phenomena as Lehmann-like rotation.
In ref. [Tarasov et al. (2003a,b)] is indeed developed an electrohydrodynamical model reproducing the rotational dynamic of the flattened cholesteric drops by making use of the flexoelectricity and without taking in account the electromechanical coupling.

4.4 The idea behind our experiment

The idea of our experiment is to realize homeotropic samples filled with a cholesteric LC with pitch slightly longer than the critical threshold value for pitch frustration ($p \simeq p_{\mathrm{th}}$). The sample will thus be frustrated by the anchoring to behave like a homeotropically aligned nematic. From the predictions and the observations reported in ref. [Abbate et al. (1993)] it is expected that the OFT threshold value is very low (zero in the limit $p \to p_{th}^{+}$). A laser light impinging on the sample will thus easily reorient it, leading to the formation a of a cholesteric domain.
The advantage of such configuration is that the cholesteric domain is well localized within the region illuminated by the laser beam and the helix will automatically develop with its axis along the beam direction, the same direction

[2]The flexoelectric effect is the analogous of the piezoelectric effect in ordinary crystals [Meyer (1969); Patel and Meyer (1987)]. It is a linear electro-optic effect and its contribution to the free energy is:

$$f_{\text{f-e}} = -e_S \vec{E} \cdot \vec{S} - e_B \vec{E} \cdot \vec{B} \tag{4.3.10}$$

where $\vec{S}$ and $\vec{B}$ are the splay and bend deformation terms. This effect becomes significant when large splay-bend deformation takes place.

along which can be applied the electric field.
This configuration seems thus optimal for excluding effects of other nature. Eventual rotations can exclusively be ascribed to the cross-couplings effects.
It is worth noting that, in such scheme, light plays an auxiliary role, leading only to the formation of the cholesteric domain. A sketch of our geometry can be found in figure 4.4. The splay-bend deformation, moreover, can be reduced at will by working very close to the threshold.

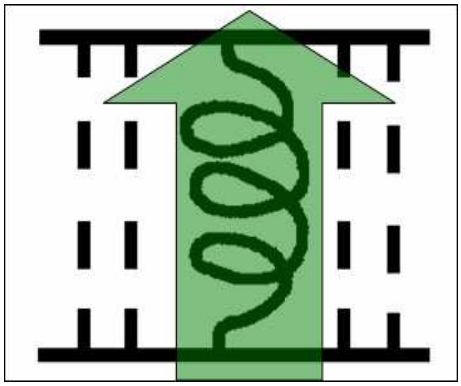

Figure 4.4: A sketch of our experimental geometry.

4.4.1 Homeotropic alignment's effects on Lehmann-like rotation

The question that could arise about our geometry is that the configuration in which we choosed to work (homeotropically aligned sample) is neither the stress-free boundary situation described by eq. (4.1.3) nor the planar aligned one, described by eq. (4.1.5). Are we sure that the director, under the action of the applied field, rotates? And how will be the eventual angular velocity in such configuration related with the stress-free boundary one (4.1.4)?

To give an answer to this question let's consider eq. (4.1.1). Since we are interested only on the effect of the field $\vec{E}$ and not on the molecular arrangement within the sample, we'll omit the effect of the molecular field $\vec{h}$. Let's then

consider the vector product with $\hat{\boldsymbol{n}}$ of the members of eq. (4.1.1):

$$\gamma_1 \hat{\boldsymbol{n}} \wedge \frac{\partial \hat{\boldsymbol{n}}}{\partial t} \approx \nu_E \, \hat{\boldsymbol{n}} \wedge \hat{\boldsymbol{n}} \wedge \vec{E}. \tag{4.4.11}$$

Supposing to apply the field parallel to the helix axis, for the helix structure frustrated by the homeotropic alignment (shown in figure 2.4-(a)), the dynamic equation will be:

$$\sin^2 \theta \left(\gamma_1 \frac{\partial \varphi}{\partial t} + \nu_E \, E \right) = 0. \tag{4.4.12}$$

Thus, although the homeotropic alignment will force the molecules to arrange outside the cholesteric planes and acquire a "distorted" configuration, the application of the field will give rise to the rotation with the same angular velocity of the stress-free boundary condition.

Moreover the rotation governed by eq. (4.4.12) is independent on θ and, hence, on the splay-bend distortion in the sample (and consequent flexoelectric effect), that can be reduced at will.

Chapter 5

Experimental setup

The aim of this chapter is to give a brief description of the stages through which our detection apparatus is evolved and why it is evolved in this way.

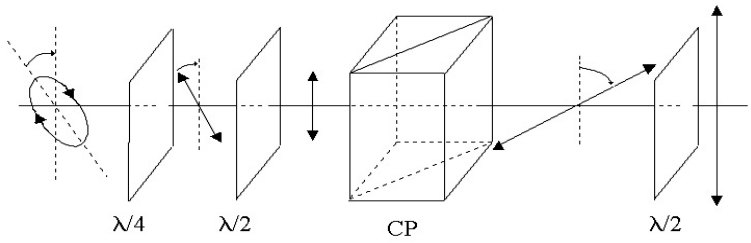

Figure 5.1: Passive attenuator.

5.1 Pump injection stage

All the forthcoming configurations are characterized by a common factor: the first stage or pump injection stage. The pump used in this work is a *Verdi* laser from Coherent, a Nd:YVO_4, frequency doubled laser at $\lambda = 532$nm in a single TEM_{00} mode, linearly polarized and with transverse circular profile.

Although is it possible to vary the pump power electronically, it is better (more stable) to use instead a passive attenuator stage. In figure 5.1 is shown our stage. Pump light comes from the left, linearly polarized along the vertical direction. A $\lambda/2$ retarder waveplate varies at will the direction of pump polarization. The light emerging from the waveplate impinges on a polarizing beam splitter (CP in the figure), that "cuts" the impinging light, letting go ahead only the component polarized along the vertical direction. Rotating the direction of the first waveplate we are thus able to choose the intensity of the trespassing light. The last stage consists of different waveplates (in figure are indicated, as an example, a $\lambda/2$ and a $\lambda/4$); their choice (or the choice of more complex objects, like Babinet's compensator or a Pockel cell) depends on which kind of polarization we want to give to the pump.

The last step of this stage is the injection lens that focalizes the pump light on the LC sample. In this work we made use of a lens with a long focal length[1] ($f = 25$cm).

5.2 Polarimeter stage

Another common factor between the different configurations is the polarimeter; thus we'll describe it briefly here. A very simple polarimeter can be realized putting in rotation around an axis parallel to the probe propagation direction a polarizer. A radiation with Stokes vector $S_{in} = \{S_0, S_1, S_2, S_3\}$ impinging on such a polarizer will emerge from it with a Stokes vector:

$$S_{out} = \left\{ \begin{array}{c} \frac{1}{2}\Big(S_0 + S_1 \cos 2\Omega t + S_2 \sin 2\Omega t\Big) \\ \frac{1}{2}\cos 2\Omega t\Big(S_0 + S_1 \cos 2\Omega t + S_2 \sin 2\Omega t\Big) \\ \frac{1}{2}\sin 2\Omega t\Big(S_0 + S_1 \cos 2\Omega t + S_2 \sin 2\Omega t\Big) \\ 0 \end{array} \right\}. \tag{5.2.1}$$

[1] The choice of a lens with such a long focal length furnishes a wider beam waist ($\simeq 100\mu$m radius) in the focus; this implies higher threshold powers for OFT but contemporary guarantees that the pump light can be treated as a nearly good approximation of the plane wave limit. We want to work in such limit for the necessity of excluding finite-beam size effects that could complicate the interpretation of our experimental results.

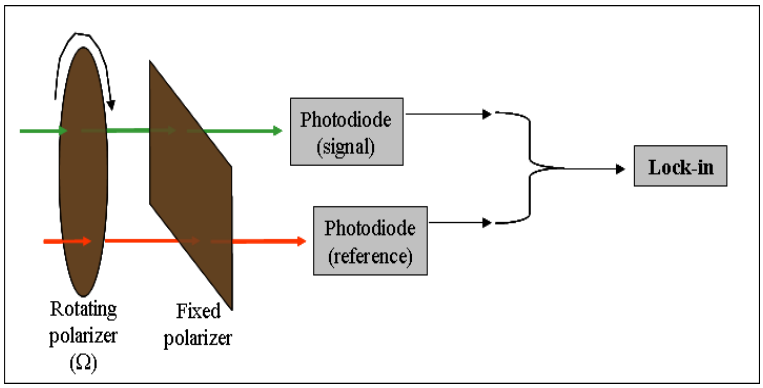

Figure 5.2: A sketch of our simple polarimeter.

Such a radiation will then be collected into a photodiode, who'll thus produce a signal:

$$V_{\text{diode}} \propto S_{0,out} = \frac{1}{2}\Big(S_0 + S_1 \cos 2\Omega t + S_2 \sin 2\Omega t\Big). \tag{5.2.2}$$

A lock-in amplifier with a reference signal at 2Ω will finally be provide the measure of the phase and quadrature part of this signal:

$$\begin{cases} X = S_1 \\ Y = S_2 \end{cases} \tag{5.2.3}$$

By means of this setup it is thus possible to measure two of the Stokes parameters (S_1 and S_2); a slight modification of this simple configuration allows us to measure a third Stokes parameter. As a matter of fact, by adding (see figure 5.2) after the rotating polarizer a second one with axis along a direction κ with respect to the reference direction (the vertical), one obtains a photodiode signal:

$$V_{\text{diode}} \propto c + X_1 \cos 2\Omega t + Y_1 \sin 2\Omega t + X_2 \cos 4\Omega t + Y_2 \sin 4\Omega t \tag{5.2.4}$$

where:

$$\begin{cases} c &= \frac{1}{4}\, S_0 + \frac{1}{8}\, S_1 \cos 2\kappa + \frac{1}{8}\, S_2 \sin 2\kappa \\ X_1 &= \frac{1}{4}\, S_0 \cos 2\kappa + \frac{1}{4}\, S_1 \\ Y_1 &= \frac{1}{4}\, S_0 \sin 2\kappa + \frac{1}{4}\, S_2 \\ X_2 &= \frac{1}{8}\, S_1 \cos 2\kappa - \frac{1}{8}\, S_2 \sin 2\kappa \\ Y_2 &= \frac{1}{8}\, S_1 \sin 2\kappa - \frac{1}{8}\, S_2 \cos 2\kappa \end{cases} \tag{5.2.5}$$

represent, respectively, the c.c. value and the amplitudes of signal's phase and quadrature at 2Ω and 4Ω. Setting the κ value to zero the lock-in signal simplifies to

$$\begin{cases} X_1 = \frac{1}{4}\, S_0 + \frac{1}{4}\, S_1 \\ Y_1 = \frac{1}{4}\, S_2 \\ X_2 = \frac{1}{8}\, S_1 \\ Y_2 = \frac{1}{8}\, S_2 \end{cases} \tag{5.2.6}$$

This simple apparatus thus lets us measure the Stokes parameters of the light emerging from the LC cell[2]. The relationship between Stokes parameters and director's configuration can be easily computed by approximating LC slab as a retarder waveplate inducing a phase shift δ (related to θ) and whose easy axis points at the angle φ with respect to the vertical direction (chosen as reference direction). The emerging Stokes vector $\bar{S}_{\text{exit}} = \{S_{0,\text{exit}}, S_{1,\text{exit}}, S_{2,\text{exit}}, S_{3,\text{exit}}\}$ is related to the impinging Stokes vector $\bar{S} = \{S_0, S_1, S_2, S_3\}$ by means of the

[2]Please note that we can measure by means of this apparatus only three (S_0, S_1 and S_2) of the four Stokes parameter. Since LC are transparent, the light polarization dynamics take place only on the Poincarè sphere and not in its inside. Thus $S_0^2 = S_1^2 + S_2^2 + S_3^2$ and it is possible to deduce S_3's value (but not its sign).

relations:

$$\begin{cases} S_{0,\text{exit}} &= S_0 \\ S_{1,\text{exit}} &= S_1\Big(\cos^2 2\varphi + \sin^2 2\varphi \cos\delta\Big) + S_2 \sin 4\varphi \sin^2\tfrac{\delta}{2} + \\ & \quad -S_3 \sin 2\varphi \sin\delta \\ S_{2,\text{exit}} &= S_1 \sin 4\varphi \sin^2\tfrac{\delta}{2} + S_2\Big(\sin^2 2\varphi + \cos^2 2\varphi \cos\delta\Big) + \\ & \quad +S_3 \cos 2\varphi \sin\delta \\ S_{3,\text{exit}} &= S_1 \sin 2\varphi \sin\delta - S_2 \cos 2\varphi \sin\delta + \\ & \quad +S_3 \cos\delta \end{cases} \tag{5.2.7}$$

5.3 First configuration

The first experimental geometry adopted was with co-propagating pump and probe (a He-Ne laser). In figure 5.3 is shown a schematic sketch of this geometry. The probe, whose polarization state is controlled by means of suitable polarizing elements (depending on the choice of the probe polarization state, argument on which we'll discuss later; in figure is indicated by the $\lambda/4$) is injected along the

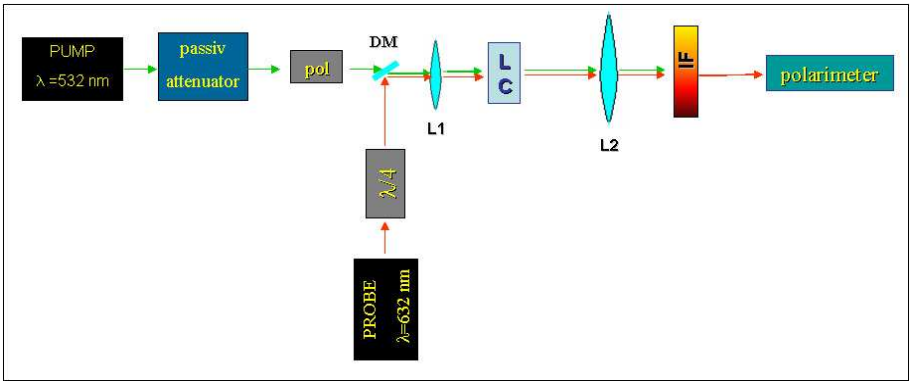

Figure 5.3: First experimental geometry: co-propagating pump and probe.

pump direction by means of a dichroic mirror; both (pump and probe) impinges on the lens L_1 that focalizes them on the LC cell, from which they emerge rapidly

divergent. A second collecting wide lens L_2 (with a 15cm diameter) is therefore put after the cell; the light collected from this second lens impinges lastly on the interferential filter (IF) that cuts off the pump radiation and transmits the probe radiation, that ends up into the polarimeter stage. As in usual pump and probe scheme, the pump induces the phenomena that are analyzed by means of the probe. The choice of the better probe's polarization is thus very important for improving the apparatus sensitivity, specially at the threshold, where a detection sensitivity as high as possible is required to avoid threshold overestimation.

5.3.1 The probe polarization

Let's consider what happens to the probe polarization emerging from LC when it is polarized linearly or circularly. In such cases eqs. (5.2.7) become:

- **Linearly polarized light:**
  Let's consider a probe light linearly polarized along the direction α. The Stokes vector of such radiation is:

$$\overline{S}_{\text{lin}} = \{S_0, S_0 \cos 2\alpha, S_0 \sin 2\alpha, 0\}. \tag{5.3.8}$$

  The Stokes vector of the radiation emerging from the sample in proximity of the threshold (for small δ):

$$\begin{cases} S_{0,\text{exit}} &= S_0 \\ S_{1,\text{exit}} &= S_0 \cos 2\alpha \\ S_{2,\text{exit}} &= S_0 \sin 2\alpha \\ S_{3,\text{exit}} &= -S_0 \delta \sin 2(\alpha - \varphi) \end{cases} \tag{5.3.9}$$

  The lock-in acquires (see eqs. (5.2.6)) S_1 and S_2 (related directly to X_2 and Y_2) and thus this configuration is not very useful, since the signals are unable to distinguish between sample below and above threshold. The only parameter sensitive to δ's variations is S_3, which is, as pointed out before, not measured directly.

- **Circularly polarized light:**

  The Stokes vector for circularly polarized probe beam is:

$$\overline{S} = \{S0, 0, 0, \sigma S_0\} \tag{5.3.10}$$

  with $\sigma \pm 1$ depending from the light under consideration (right- or left-handed). The Stokes vector of the radiation emerging from the sample in proximity of the threshold (for small δ):

$$\begin{cases} S_{0,\text{exit}} &= S_0 \\ S_{1,\text{exit}} &= -\sigma S_0\, \delta \sin 2\varphi \\ S_{2,\text{exit}} &= \sigma S_0\, \delta \cos 2\varphi \\ S_{3,\text{exit}} &= \sigma S_0 \end{cases} \tag{5.3.11}$$

This configuration is the most sensible one, since S_1 and S_2 grow linearly with δ: it is thus a good configuration, indicated for threshold detection measurements. It is worth noting that, in this configuration, one can easily obtain δ and φ using only the amplitude ($R_2 = \sqrt{X_2^2 + Y_2^2}$) and the phase ($R_2 = \arctan(Y_2/X_2)$) of the signal[3] at the frequency 4Ω:

$$\begin{cases} R_2 &= \sqrt{\left(-\frac{1}{8}\sigma S_0\, \sin\delta \sin 2\varphi \right)^2 + \left(\frac{1}{8}\sigma S_0\, \sin\delta \cos 2\varphi \right)^2} = \\ &= \frac{1}{8} S_0 \sin\delta \\ \theta_2 &= \arctan\left(\frac{S_0 \sin\delta\, \cos 2\varphi}{S_0 \sin\delta\, \sin 2\varphi} \right) = \arctan\cot 2\varphi = -\frac{\pi}{2} + 2\varphi \end{cases} \tag{5.3.12}$$

Noting that the angle ψ of the major axis of the polarization ellipse is related to θ_2 by means of the simple relation:

$$\psi = \frac{1}{2}\, \theta_2 \tag{5.3.13}$$

we obtain the that polarization ellipse in the case of circularly polarized light emerges with a difference of phase of $\pi/4$ with respect to the sample direction

[3] Those expression are exact and not the series expansion for small δ given in eqs. (5.3.11).

φ:

$$\psi = \varphi - \frac{\pi}{4}. \tag{5.3.14}$$

5.3.2 Limitations

This system, although the clever choice of the probe polarization, is not very sensitive with respect to δ's variations; δ should increase linearly with the far-field self diffraction ring number. As shown in figure 5.4, this is not the case.

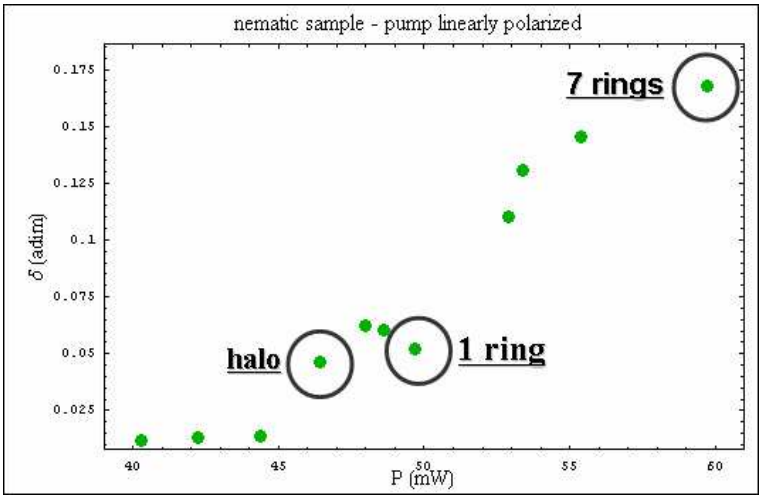

Figure 5.4: δ acquisition taken for a nematic sample (70μm thick) reoriented by a linearly polarized light.

The problem of such configuration lyes in the lacking correspondence between hypothesis and real situation. Experimental data interpretation bases itself on the assumption that the hypothesis leading to eqs. (5.2.7) are true. In particular, it is important for δ being constant over the whole region illuminated by the probe beam. This condition is true only if the probe transverse beam size in correspondence of the sample is much narrower than the pump one and transverses only the central part of the reorientated sample, part in which the δ value remains nearly constant. This assumption was not valid. Experimentally, the probe illuminated a region much wider then the region illuminated by the

pump (see figure 5.5). Since both, pump and probe, were focused on the sample by the same lens, it was very hard to make the probe narrower then the pump[4]; thus we decided to adopt a different experimental configuration.

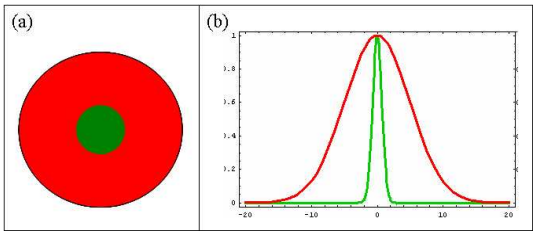

Figure 5.5: Schematic description of pump and probe behavior in proximity of the LC in the first experimental configuration: (a) The probe spot is wider than the pump one. (b) Transverse intensity profiles: the probe integrates over reoriented and unoriented parts of the sample.

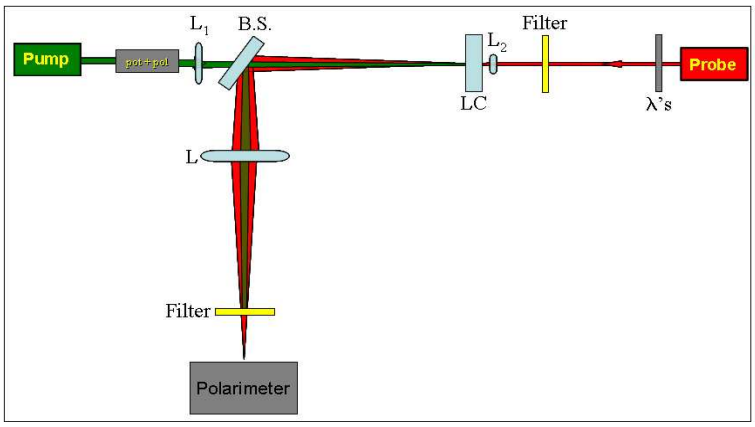

Figure 5.6: Second experimental geometry: counter-propagating pump and probe.

[4]To make the probe narrower than the pump in correspondence of the lens focal plane, one has to ensure the probe being wider than the pump before impinging the lens L_1 (since they are gaussian); the easiest way of making the probe wider is to make use of two lenses confocal mounted (in telescopic configuration) but, despite the simplicity of this configuration, it is not so easy to warranty a probe beam impinging on the lens L_1 parallel and not converging/diverging; in addiction, it is not possible to have a probe narrow at will, because of limitations on the spatial extension of the telescope (the greater the zoom factor (f_1/f_2) is, the longer the telescope $(f_1 + f_2)$ has to be).

5.4 Second configuration

Since the poor sensitivity of the detection apparatus in the first experimental configuration due to the "incorrect" spatial extension of pump and probe and the difficulties in varying them independently, we decided to adopt a second configuration, in which the two beams were counter-propagating. In such a way it is possible to adjust the two beam sizes in proximity of the sample independently, since they are focused on the sample by different lenses, as shown in figure 5.6.

The probe polarization was chosen, according to the reasoning performed in section 5.3.1, to be circular. The lens L_2 focusing the probe beam on the

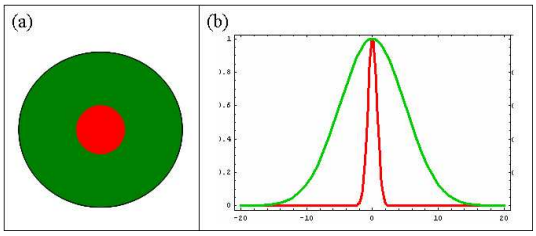

Figure 5.7: Schematic description of pump and probe behavior in proximity of the LC in the second experimental configuration: (a) The probe spot is narrower than the pump one. (b) Transverse intensity profiles: the probe trespasses only the central part of the pump beam, experiencing a constant δ value.

LC sample was chosen with a very short focal length ($f_{L_2} = 3$cm) and ensured the validity of the δ constant value assumption. In figure 5.7 is schematically showed what happens in proximity of the sample.

5.4.1 Limitations

As shown in figure 5.8, this configuration detects very sensitively directors reorientation, even when the far field self-diffraction pattern has not been well developed (indicated in figure with "sizzlings").
The big problem of this configuration is its failure when the self diffraction pattern in the far field has more then one ring. The problem is that, the more

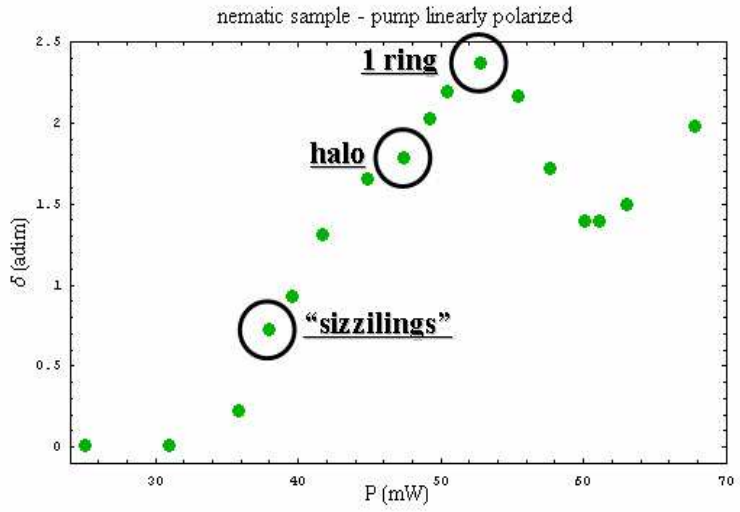

Figure 5.8: δ acquisition taken for a nematic sample (70μm thick) reoriented by a linearly polarized light.

the rings are, the wider the self-diffraction pattern is. The probe beam, rapidly diverging from its own (because focused by a short focal length lens), is too wide to be entirely collected by the beam splitter. The more the rings, the greater is the part of the probe that goes lost. That explains why the signal, after one ring, is rapidly reduced.

As an attempt to solve this problem, one could make use of wider beam splitter but it would extend the range of response of the system to two, three rings and then there will anyway be a critical rings number over which the system will however fail.

This setup is thus indicated for its very high sensitivity for threshold measurements but fails over a certain ring number.

5.5 Third and definitive configuration

Taking into account the difficulties related to the fact that the probe beam had to obey to the laws of the gaussian optics and to its limitations and that we are seeking for a detection apparatus working in every experimental range, our last experimental setup was realized renouncing to a probe laser beam. We used instead as probe a white, depolarized light source (emitted from a light bulb), and realized a probe detection apparatus consisting in an opportune modification of the classical polarized microscope. The sketch of our experimental setup is shown in figure 5.9.
Since, to our knowledge, this work represent the first time in which such an apparatus is used to characterize the interaction between light and liquid crystals, few words have to be spent about the meaning of the acquisitions performed by means of this experimental setup.

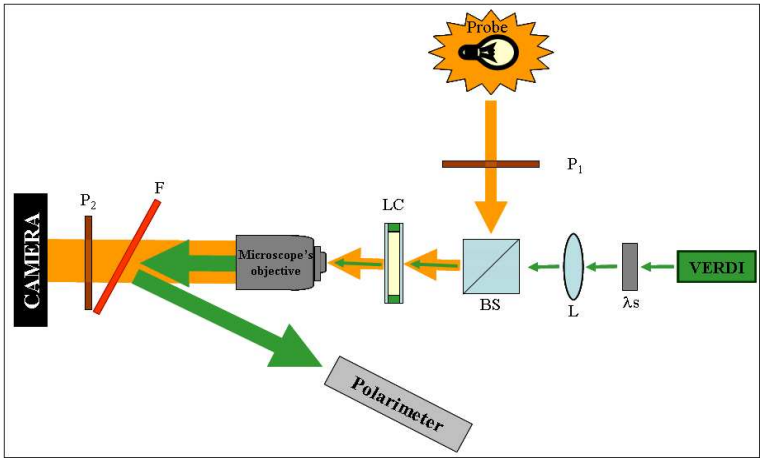

Figure 5.9: A sketch of the third experimental setup.

5.5.1 Microscope observations: the probe arm of the experimental setup.

Since the probe light illuminate a region of the sample much wider (order of magnitude) than the pump beam size, the assumption of a constant δ profile

won't be valid anymore.

Let us then start by approximating the liquid crystal (LC) cell as a retardation waveplate with nonuniform phase shift $\delta(x, y)$ and easy axis at an angle φ with respect to a reference direction (chosen, for convenience, along the linear polarization of the Verdi laser).

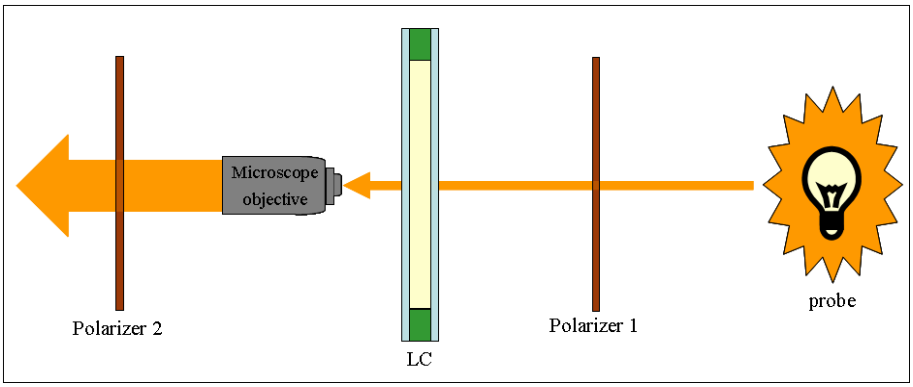

Figure 5.10: The probe's path.

The probe arm of the experiment is made by a light source (a light bulb which emits unpolarized white light isotropically along every direction), a collimating stage (a set of lenses), a first polarizer at an angle η with respect to the reference direction, the LC cell (described, as stated above, as a retarder plate), the second polarizer (crossed with respect to the first polarizer at an angle $\eta + \pi/2$) and, finally, the microscope objective. A schematic representation of the probe arm can be found in figure 5.10.

The intensity of the radiation emerging from such a system is:

$$S_{0,out} = \frac{1}{2}\sin^2\frac{\delta(x,y)}{2}\sin^2[2(\eta-\varphi)]\Big(S_{0,in}+S_{1,in}\cos 2\eta+S_{2,in}\sin 2\eta\Big) \quad (5.5.15)$$

where $S_i(i, 0, .., 3)$ are the Stokes parameters.
If the first polarizer is along the vertical, this expression simplifies to:

$$I = \frac{I_0}{2}\ \cos^2\eta\ \sin^2[2(\eta-\varphi)]\ \sin^2\frac{\delta(x,y)}{2}. \quad (5.5.16)$$

where I_0 is the intensity of the light impinging the first polarizer[5].

At this point it should be described *how* the LC reorientates and, thus, which shape should be given to $\delta(x, y)$ for a good description of the reorientation profile[6]. Firstly, we assume a gaussian reorientation profile centered on the laser beam; then, taking into account the effects of the elastic anisotropy of liquid crystals, we assume this profile being, rather than circular, elliptical (characterized with its long axis at a direction γ with respect the x axis and amplitudes $2\sigma_x$ and $2\sigma_y$, as shown in figure 5.11); we then obtain:

$$\delta(x, y) = n\pi \; e^{-\frac{(x\cos\gamma + y\sin\gamma)^2}{\sigma_x^2} - \frac{(y\cos\gamma - x\sin\gamma)^2}{\sigma_y^2}} \tag{5.5.17}$$

where n represents, the gaussian's amplitude, in π units, at the origin.

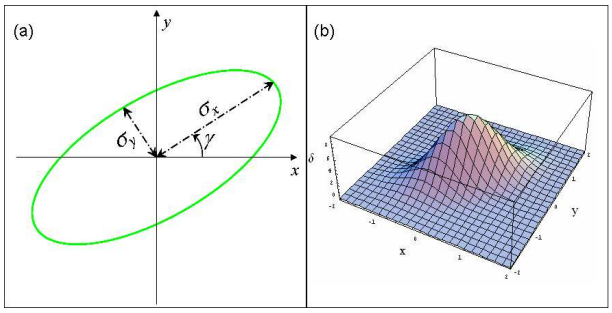

Figure 5.11: Schematic representation of the delay profile.

The resulting probe intensity profile is:

$$I(x, y) = \frac{I_0}{2}\cos^2\eta \; \sin^2\left[2(\eta - \phi)\right] \; \sin^2\left[\frac{n\pi}{2} e^{-\frac{(x\cos\gamma + y\sin\gamma)^2}{\sigma_x^2} - \frac{(y\cos\gamma - x\sin\gamma)^2}{\sigma_y^2}}\right]. \tag{5.5.18}$$

Figure 5.12 shows intensity profiles during a typical LC reorientation process (for example the Fréedericksz transition under linearly polarized light), characterized by an increasing value of n and fixed values of the other parameters.

A very important consequence of expression (5.5.18) is that the angle φ ap-

[5]The factor 1/2 arises because the input light is unpolarized.

[6]The reorientation is assumed to lie in a plane at angle φ with respect to the horizontal axis.

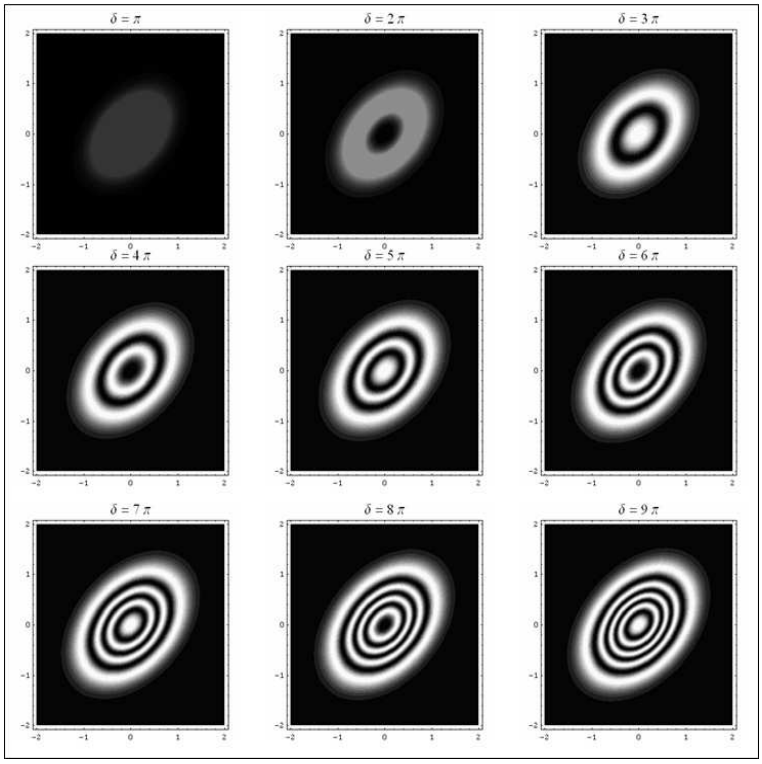

Figure 5.12: Intensity profile of the probe radiation emerging from the system (LC+polarizers) according to expression (5.5.18); parameter values used for this simulation: $S_0 = 1, \eta = \pi/4, \varphi = 0, \gamma = \pi/4, \sigma_x = 0.9, \sigma_y = 0.6$).

pears only in the factor $\sin^2[2(\eta - \varphi)]$ and is thus "decoupled" from the δ-terms of the reorientation profile: φ regulates only (depending from the amount of the "crossing" with the polarizer's angle η) the relative value of the maximum of the intensity profile, independently of the gaussian's amplitude and direction and it doesn't act on the gaussian's shape. So, a steadily growing value of φ doesn't imply, as someone could wrongly expect, a rigid rotation of the concentric ring pattern; rather it determines a periodical modulation of its intensity. An example of this behaviour is shown in figure 5.14.

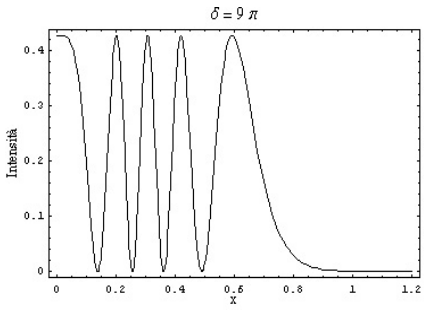

Figure 5.13: As clearly shown in this example, n in expression (5.5.17) represents the number of maxima and minima of a section of probe's intensity profile moving from the middle of the pattern towards the external part.

5.5.2 Pump polarization state.

Besides the polarimeter microscope with the probe bulb lamp, in our experimental setup a second polarimeter analyzes the pump radiation emerging from the LC sample, as can be seen in figure 5.9. In such configuration δ can not be assumed to be constant and its inhomogeneities has to be taken in account.

Let us consider a generic pump polarization state:

$$S_{in} = \{S_0, S_1, S_2, S_3\}.$$

This radiation impinges directly on the LC cell[7], approximated as a retarder waveplate plate $\delta(x, y)$ at angle φ, and emerges from it with an ellipticity:

$$S_{3,out} = S_1 \sin\delta \sin 2\varphi - S_2 \sin\delta \cos 2\varphi + S_3 \cos\delta. \tag{5.5.19}$$

The major axis of the polarization ellipse will be at an angle ψ such that:

$$\tan 2\psi_{out} = \frac{S_{2,out}}{S_{1,out}} =$$

$$= \frac{S_1\ 2\sin 4\varphi\ (1-\cos\delta) + S_2\ (\sin^2 2\varphi + \cos^2 2\varphi\ \cos\delta) + S_3\ \cos 2\varphi\ \sin\delta}{S_1\ (\cos^2 2\varphi + \sin^2 2\varphi\ \cos\delta) + S_2\ 2\sin 4\varphi\ (1-\cos\delta) - S_3\ \sin 2\varphi\ \sin\delta}. \tag{5.5.20}$$

Such an expression is very complicated and depends strongly on δ's shape. However there is a very special case in which this expression simplifies notably:

[7] in what follows, for sake of simplicity, we'll use δ instead of $\delta(x, y)$ but it should anycase be kept in mind that we are dealing with a nonuniform reorientation profile.

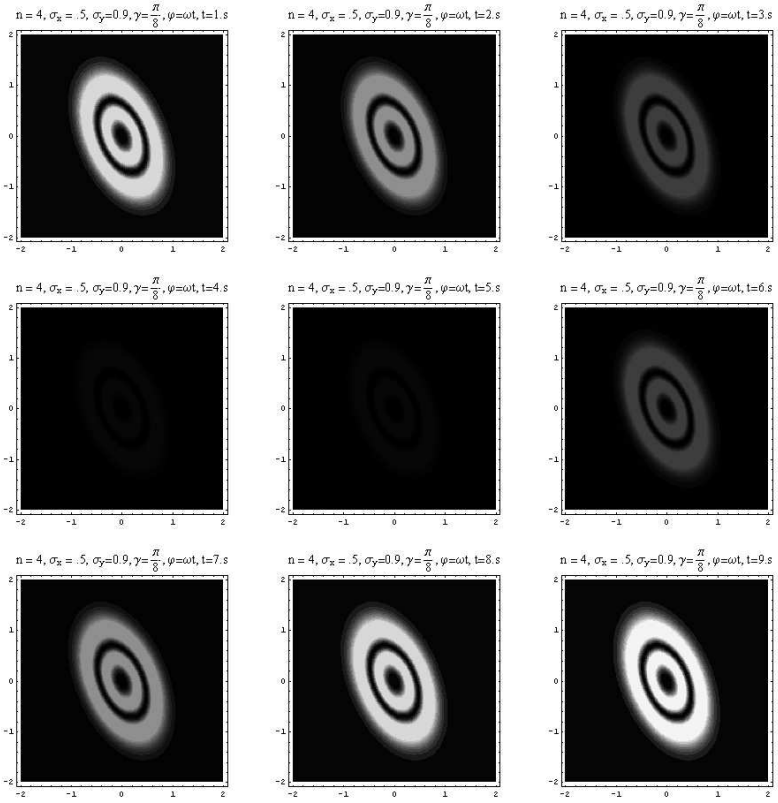

Figure 5.14: The increasing value of φ doesn't change the shape of the concentric ring pattern: it acts only on its brightness, modulating it periodically.

the circular polarization case. In such a case, the initial pump polarization state is:

$$S_{in} = \{S_0, 0, 0, \sigma S_0\}$$

(with $\sigma = \pm 1$ depending from the handedness of the light) and ψ's expression simplifies to:

$$\psi_{out} = -\frac{1}{2} \operatorname{arctan\,cot} 2\varphi = -\varphi \pm \frac{\pi}{4} \tag{5.5.21}$$

(the sign + or − are depending from the choice of the tangent's determination). It is worth noting that in this case ψ_{out} is independent from $\delta(x, y)$, whatever complicated shape it possesses, and depends uniquely on the angle φ of the easy

axis of the plate.

Reassuming, our probe apparatus (the microscope) allows us to easily obtain the reorientation profile shape's parameters (i. e. n, γ, σ_x and σ_y) but it doesn't work so good in measuring the angle φ.
However, the polarization state of the pump radiation emerging from the LC cell carries information about the LC reoriented state too: φ can be thus obtained from it.

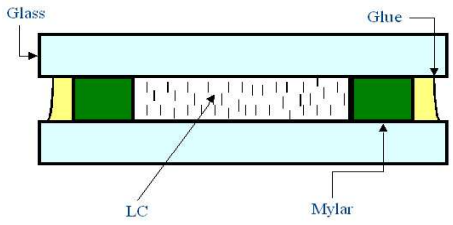

Figure 5.15: Schematical representation of a typical cell section.

5.6 Samples and mixtures

In figure 5.15 it is schematically represented a LC cell, composed by two glasses preventively covered with a surfactant for strong homeotropic anchoring and separated by two Mylar spacers (nominal thickness 70μm).
The used surfactant is D.M.O.A.P. (n-octadecildimetil[3-(trimetoxisilil)propil]--ammoniocloride). The cells on which the electric field has to be applied were realized by making use of I.T.O. (Indium Tin Oxide) coated glasses.

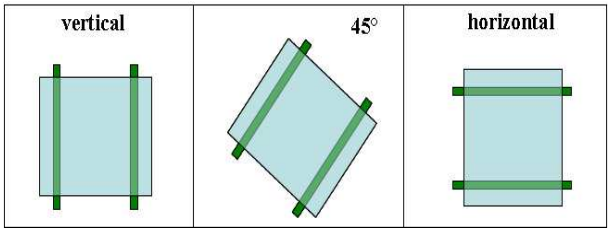

Figure 5.16: Frontal view of the sample aligned parallel to the vertical, at 45^o and along the horizontal direction.

The cholesteric LC used in the reported experimental acquisitions is a mixture obtained by a doping the pure nematic E7 (produced by Merck) with the chiral agent C15 (produced by Merck too); for the mixture used in our experiment C15's per cent concentration is $c_{\mathrm{C15}} = 1.31 \pm .0.01\%$ w/w for our mixture. The pitch of such a mixture, as desired, is slightly longer than the critical

threshold value for our cell thickness (70μm). This mixture shows a singular behaviour: it is so near to the critical value, that shows dependence from the gravity that is not present in other mixtures far away from this critical situation. As a matter of fact, rotating the sample around the z axis (the horizontal axis of laser propagation) the fluxes within the fluid favor the formation of a cholesteric finger pattern in which the finger are parallel to each other and whose axis points along (or normally to) the vertical. In figure 5.16 are represented

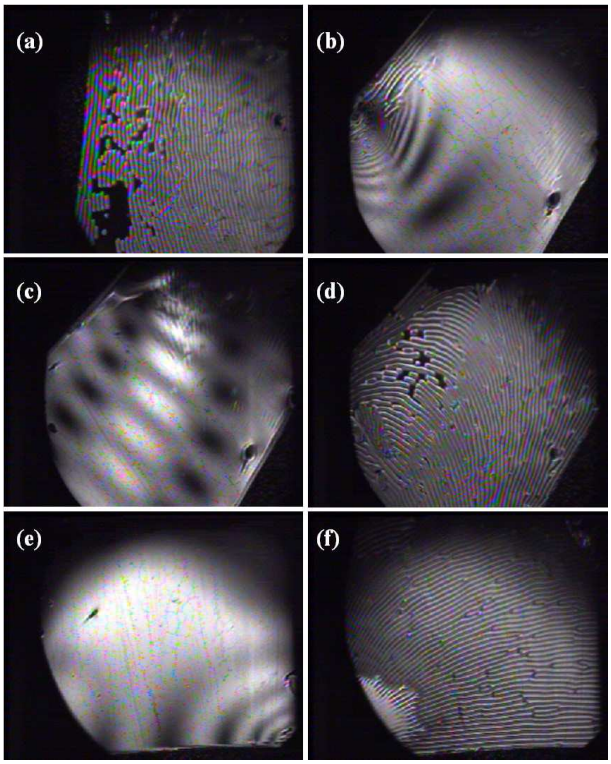

Figure 5.17: The referred positions are those showed in figure 5.16. (a) sample in the vertical position - (b), (c) and (d) sample at 45^o - (e) and (f) sample in the horizontal position.

the sample directions for the pictures taken in figure 5.17. In figure 5.17-(d), for example, we can see how the fingers tend to align their axis along the vertical, that is at 45^o with respect to the mylar stripes.

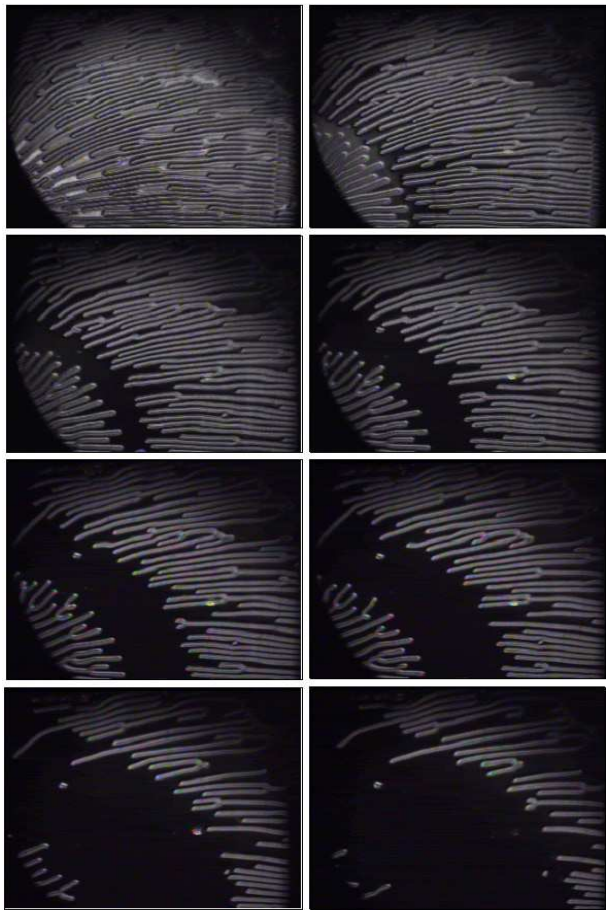

Figure 5.18: The relaxation from thefinger domain to the homeotropic one.

In figure 5.18 is shown the slow relaxation from the striped finger domain to the homeotropic configuration. Being the pitch near to the critical value, this relaxation process needed about 40 hours to reach its stable configuration (without fingers).

In figure 5.19 it is shown the behaviour of the opposite situation: the mixture ($c_{C15} = 1.39 \pm .0.01\%$) had a pitch slightly shorter than the threshold value; the system thus spontaneously tended to form the fingerprint texture (note that in this case the texture is no more striped, resembles really fingerprints because of

its irregularity and the direction of gravity does not matter any more).

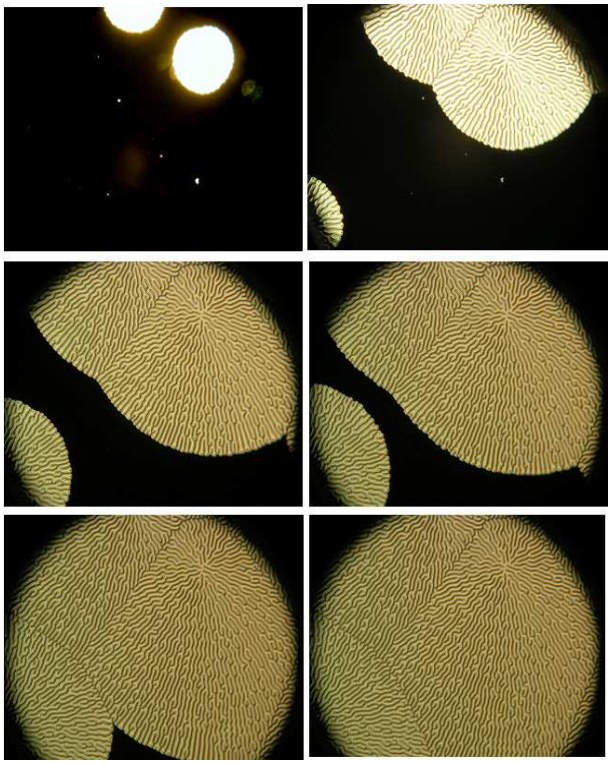

Figure 5.19: Spontaneous fingerprint texture formation.

Chapter 6

Nematic samples

In this chapter we'll report our experimental observations taken on the well studied case of OFT in nematic samples[1]; we monitored the reorientation process with our new detection apparatus, whose ability to detect the shape of the reorientation pattern leads to an unexpected result in the case of circularly polarized impinging light, where the S.I.S.L.S. (described in section 3.4) phenomenon takes place. A model developed beyond the planar distortion hypothesis needs to be developed for a fitting description of the experimental observations.

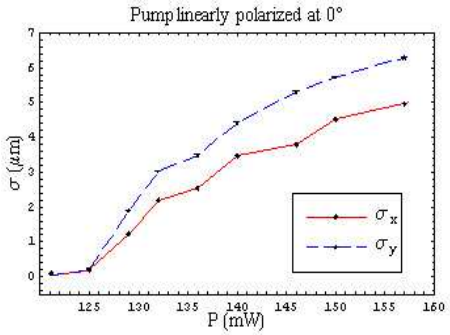

Figure 6.1: Spatial extension of the reorientation pattern for linearly polarized pump light.

[1] As said in the preceding chapter, the samples used in the experiments are 70μm thick cells.

6.1 Linearly polarized pump light

In the case of linearly polarized pump light, the reorientation process is supposed to proceed with an increasing δ value in correspondence of increasing values of the pump power. Contemporary, one expects the φ value remaining constant.

In figure 6.2 are shown the pictures for the reorientation profile taken for dif-

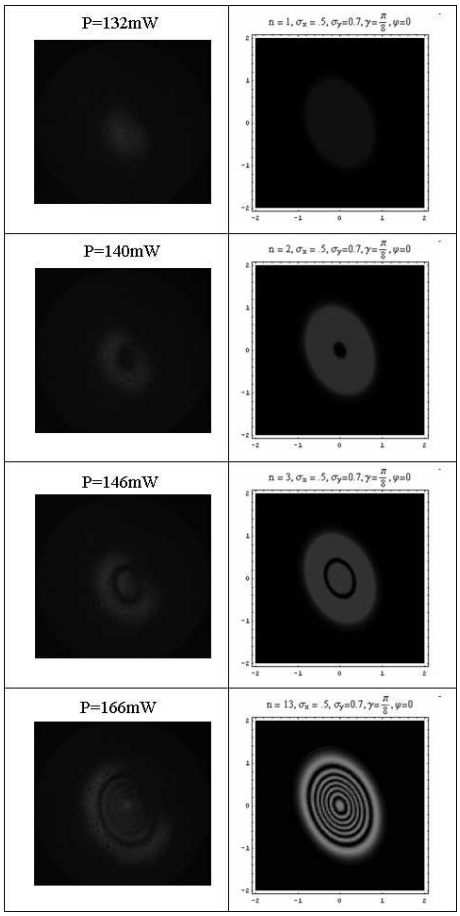

Figure 6.2: Experimental acquisitions (left column) versus inhomogeneous retarder waveplate predictions (right column).

ferent values of the pump power and are confronted with the predictions of the

model developed in section 5.5.1. These simulations were performed by leaving φ unchanged and contemporary increasing δ, or, precisely, the value of the gaussian amplitude n at the origin (referring to eq. (5.5.17)).

As one can see, the agreement between predictions and experimental observations in the case of linearly polarized pump light is very good.

In figure 6.1 are shown the diameters of the reorientation profile (analysis performed by marking every picture and monitoring the markers) as a function of the pump power.

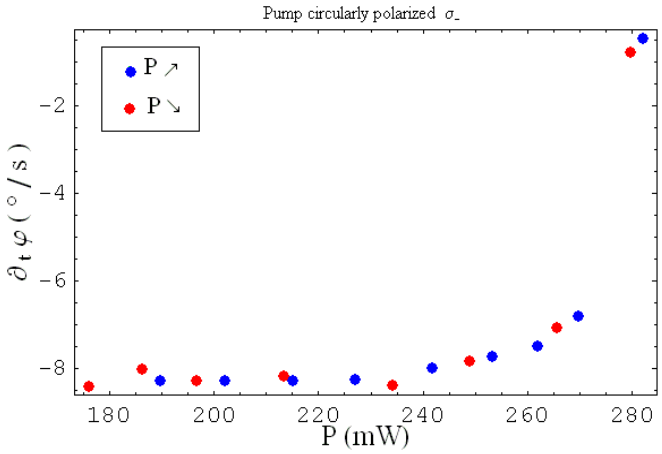

Figure 6.3: Director's rotation angular velocity (pump circularly polarized σ_-).

6.2 Circularly polarized pump light

The case of circularly polarized pump makes clear the innovation introduced by our detection apparatus. To understand why, we can confront the acquisitions taken from the polarimeter stage and the acquisition taken from the microscope (our probe).
In the case of circularly polarized pump, it is expected that, for a given value of the pump power, δ remains constant while φ increases linearly with the time,

corresponding to a physical situation in which the molecular director $\hat{\boldsymbol{n}}$ rotates along the z direction (pump laser direction of propagation). As suggested in section 5.5.1 and simulated in figure 5.14 such behaviour would imply a transmitted intensity profile "fixed" (i.e. whose shape remains frozen) but oscillating in its brightness (depending from the crossing between φ and the direction of the axis of the crossed polarizers).

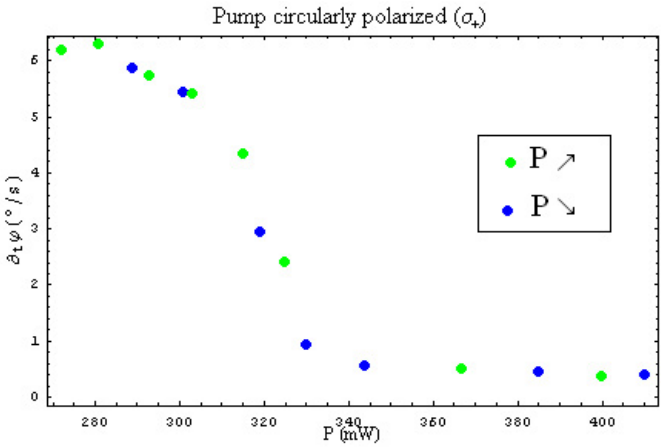

Figure 6.4: Director's rotation angular velocity (pump circularly polarized σ_+).

Observing polarimeter's acquisitions (see figures 6.3 and 6.4), one would probably agree that such predictions are correct, since the director rotates for every pump power. This picture unfortunately doesn't correspond to the physical reality *entirely*. The differences emerge when we observe[2] the behaviour of the reoriented pattern (see figure 6.5).

As expected, the pattern brightness oscillates periodically but δ doesn't remain frozen (as the pattern simulated in figure 5.14 does). The whole pattern is put in rotation by the light. This effect was never observed before. The acquisition systems used till now gained their information, as described in section 3.3.2, eq. (3.3.19), by the far field self diffraction ring pattern; this system

[2]It is possible to download the videos of the dynamic behaviour of the reoriented pattern in this and other experimental configurations from the web page: `http://people.na.inf.it/~anton/PhD.html`.

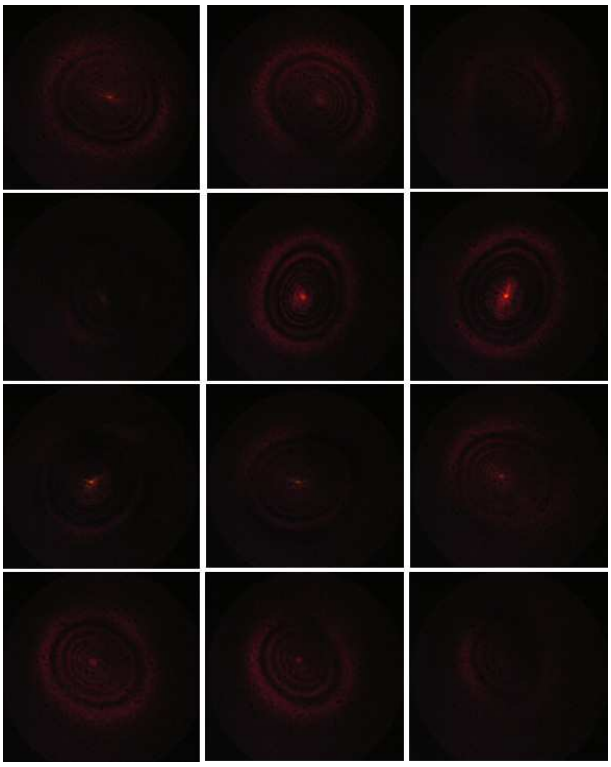

Figure 6.5: Pictures of the reoriented pattern under circularly polarized light.

furnishes the amplitude of the gaussian profile at the origin (n/π in our notation), that doesn't change, since the whole pattern rotates rigidly, without changing its shape. Correspondingly, in our inhomogeneous waveplate retarder model, this situation implies that γ's value increases while the other parameter remain constant, given the pump power value.

From the comparison between pictures and polarimeter acquisition we can deduce that φ and γ velocity are synchronous.

Such results have never been observed before nor have been foreseen by any numerical model (that are usually developed in the planar deformation hypothesis $\hat{\boldsymbol{n}}(\vec{x},t) = \hat{\boldsymbol{n}}(z,t)$).

6.3 3-d model

Recently our group has developed a three-dimensional dynamical model based on the Ritz variational principle for analyzing the results of light's orbital angular momentum (related to the transverse beam profile) transfer in liquid crystals [Piccirillo et al. (2005)].

Such a model goes beyond the planar distortion approximation, retaining all the x, y and z coordinates in the molecular director, and takes in account the anisotropies in the molecular response: it is thus able to describe our experimental observations.

This model is based on a set of ODEs obtained by applying the Ritz variational method to the nematic free energy $\mathcal{F}$ and the dissipation function $\mathcal{R}$ of the whole sample. The method consists in assuming realistic space profiles of the director field $\hat{\boldsymbol{n}}(\vec{x},t;p)$ and of the optical field $\vec{E}(\vec{x},t;p)$ in the sample. The profiles $\hat{\boldsymbol{n}}(\vec{x};p(t))$ and $\vec{E}(\vec{x};p(t))$ depend on time through a set of parameters $p_i(t)$ $(i=1,...,N)$ and are chosen so to calculate analytically the free energy $\mathcal{F}(p)$ and dissipation function $\mathcal{R}(p)$ as explicit functions of the parameters p_i. The $p_i(t)$ time evolution is then evaluated from ODEs

$$\frac{\partial \mathcal{F}}{\partial p_i} = \frac{\partial \mathcal{R}}{\partial \dot{p}_i} \qquad (i=1,...,N). \tag{6.3.1}$$

where $\dot{p}_i$ denotes the time derivative of the parameters p_i.

Crucial to the method is the choice of the profiles of $\hat{\boldsymbol{n}}(\vec{x};p(t))$ and $\vec{E}(\vec{x};p(t))$, that must be as realistic as possible. Since the model deals with beams carrying either orbital and spin angular momentum (thus chosen to be elliptically shaped, with beam waists along the x and y direction, respectively, w_x and w_y), the profiles of for the polar angles θ and ϕ of $\hat{\boldsymbol{n}} = (\sin\theta\cos\phi, \sin\theta\sin\phi, \cos\theta)$ are supposed to be elliptically shaped; their expression is:

$$\theta = \theta(x,y,t) = \theta_0(t) e^{-\frac{1}{2L^2}\boldsymbol{\rho}\cdot Q(t)\boldsymbol{\rho}} \qquad \boldsymbol{\rho} = (x,y), \tag{6.3.2}$$

and

$$\phi = \phi(z,t) = \phi_0(t) - \phi_1(t)\cos\left(\frac{\pi z}{L}\right), \tag{6.3.3}$$

where L is the sample thickness. The matrix $Q(t)$ in Eq. (6.3.2) is given by $Q(t) = R^{-1}(\gamma(t))Q_0(t)R(\gamma(t))$ where $R(\gamma(t))$ is the 2×2 matrix representing the rotation of angle $\gamma(t)$ and $Q_0(t)$ is defined as

$$Q_0(t) = \begin{pmatrix} \alpha_1(t) & 0 \\ 0 & \alpha_2(t) \end{pmatrix} \tag{6.3.4}$$

where α_i are related to the amplitudes of the θ profile by means of the relation $\alpha_{1,2} = 2L^2/(w^{\theta}_{1,2})^2$. The profiles in Eqs. (6.3.2) and (6.3.3) obey the boundary conditions for homeotropic alignment, viz. $\theta(0) = \theta(L) = 0$ and $\partial\phi/\partial z(0) = \partial\phi/\partial z(L) = 0$.
The parameters $p_i(t)$ $(i = 1, \ldots, 6)$ of our model are the maximum tilt angle $\theta_0(t)$, the rotation angle $\phi_0(t)$, the torsion angle $\phi_1(t)$ and, finally, the three independent entries of the 2×2 symmetric matrix $Q(t)$ defining the transverse profile of θ. More precisely, we defined $p_i = (\phi_0, \phi_1, \gamma, \theta_0, \alpha_1, \alpha_2)$ in this order. All the parameters p_i are dimensionless.

When the profiles of eqs. (6.3.2) and (6.3.3) are inserted in the usual Frank's elastic free energy (2.3.28), the integration over the sample volume can be carried out, leading to the expression:

$$\begin{aligned} \mathcal{F} \;=\; & \tfrac{\pi k_{33} L}{16\sqrt{\alpha_1\alpha_2}}\Big[4\pi^2 + \Big(A+B\Big)(\alpha_1+\alpha_2) + \\ & -\Big(A-B\Big)(\alpha_1-\alpha_2)\cos[2(\gamma-\phi_0)]\Big]\theta_0^2 \end{aligned} \tag{6.3.5}$$

In the equations above, we posed $A = 1 - k_{11}/k_{33}$ and $B = 1 - k_{22}/k_{33}$ and we retained terms up to the second-order in θ_0 and to the first order in ϕ_1. No conditions have been posed on the rotation angle ϕ_0.

Because in nematics $A > B$, we see from eq. (6.3.5) that, when $\theta_0 \neq 0$ and, for example, $\alpha_1 > \alpha_2$, the free energy is minimum if $\phi_0 = \gamma$. A restoring force then results tending to orient the average azimuthal angle ϕ_0 of the director along the major axis of the elliptic profile of the θ-distribution. This coupling between ϕ_0 and γ angles vanishes when the twist and the bend elastic constants are equal ($k_{11} = k_{22} \Rightarrow A = B$) or when the laser induced θ-distribution is cylindrically symmetric around the z-axis. This effect is obviously cancelled out in

the one-elastic-constant approximation.

The optical contribution $\mathcal{W}_o$ to the free energy is obtained by integrating over the sample volume the density:

$$w_0 = \frac{I_0}{4\,c\,n_o}(\bar{n}^2(\theta) - n_o^2)\Big(\tilde{S}_0 + \tilde{S}_1 \cos 2\phi + \tilde{S}_2 \sin 2\phi\Big) \tag{6.3.6}$$

where c is the speed of light, $\tilde{S}_i = S_i(z)/S_0(0)$ $(i = 0, ..., 3)$ are the Stokes parameter of the beam polarization inside the sample divided by the value $S_0(0)$ of the Stokes parameter S_0 at the input plane of the nematic film, $I_0 = (c/8\pi)S_0(0)$ is the incident laser intensity, $\bar{n}(\theta)$ is the refractive index as seen by the extraordinary wave, and, finally, n_o is the refractive index of the ordinary wave.
The Stokes parameters S_i are calculated from the explicit expression of the optical electric field in the Geometric Optic Approximation (GOA) for plane waves [Zel'dovich and Tabiryan (1982)].

The dissipation function density expression is:

$$R = \frac{\gamma_v}{2}(\boldsymbol{n}\times\dot{\boldsymbol{n}})^2 \tag{6.3.7}$$

where γ_v is an effective viscosity coefficient. Up to terms in θ_0^2, $\mathcal{R}$ can be expressed as:

$$\mathcal{R} = \Big(\frac{\pi\, k_{33}\, L\, \tau}{2\sqrt{\alpha_1\alpha_2}}\Big)\, \theta_0^2 (M)_{ij}^{-1}\, \dot{p}_i \dot{p}_j \tag{6.3.8}$$

where $\tau = \gamma_v L^2/k_{33}$ is the characteristic response time of the system.

Eqs. (6.3.1) can be then put in the form

$$\dot{p}_i = M_{ij}\mathcal{T}_i \tag{6.3.9}$$

where $\mathcal{T}_i$ are the torque defined by:

$$\mathcal{T}_i = \frac{\partial \mathcal{F}^{\rm tot}}{\partial p_i} \tag{6.3.10}$$

and M_{ij} is given by:

$$M = \begin{pmatrix} 2+\frac{\theta_0^2}{4} & 0 & 0 & 0 & 0 & 0 \\ 0 & 8+\frac{2\theta_0^2}{3} & 0 & 0 & 0 & 0 \\ 0 & 0 & \frac{8\alpha_1\alpha_2}{(\alpha_1-\alpha_2)^2} & 0 & 0 & 0 \\ 0 & 0 & 0 & 4\theta_0^2 & 4\alpha_1\theta_0 & 4\alpha_2\theta_0 \\ 0 & 0 & 0 & 4\alpha_1\theta_0 & 16\alpha_1^2 & 0 \\ 0 & 0 & 0 & 4\alpha_2\theta_0 & 0 & 16\alpha_2^2 \end{pmatrix}. \tag{6.3.11}$$

Retaining all the terms up to the fourth order in θ_0 and ϕ_1, the elastic free energy expression will be:

$$\mathcal{F}_e = F_0 \left\{ P_0 + P_1(\alpha_2+\alpha_1) + P_2(\alpha_2-\alpha_1)\cos[2(\gamma-\phi_0)] \right\} \tag{6.3.12}$$

where

$$F_0 = \frac{\pi k_{33} L}{16\sqrt{\alpha_1\alpha_2}}. \tag{6.3.13}$$

and P_0, P_1, P_2 are polynomials given by:

$$\begin{cases} P_0 &= \pi^2 \left[(4+3\phi_1^2)\theta_0^2 + \left(\frac{A-1}{2} - \frac{5}{3}\phi_1^2\right)\theta_0^4 \right] \\ P_1 &= (A+B)\theta_0^2 - \frac{3}{16}(A-1)\theta_0^4 \\ P_2 &= -(A-B)\left(1 - \frac{1}{2}\phi_1^2 + \frac{1}{12}\phi_1^4\right)\theta_0^2 + \\ & \quad + \frac{(A-1)}{16}\left(3 - \phi_1^2 + \frac{1}{8}\phi_1^4\right)\theta_0^4 \end{cases} \tag{6.3.14}$$

The elastic contributions to the torques $\mathcal{T}_i$ can be obtained by derivation of $\mathcal{F}_e$ with respect to the p_i:

$$\mathcal{T}^e_{\phi_0} = 2F_0P_2(\alpha_2-\alpha_1)\sin[2(\gamma-\phi_0)] \tag{6.3.15}$$

$$\mathcal{T}^e_{\phi_1} = F_0\left\{Q_0 + Q_1(\alpha_2+\alpha_1) + Q_2(\alpha_2-\alpha_1)\cos[2(\gamma-\phi_0)]\right\} \tag{6.3.16}$$

$$\mathcal{T}^e_{\gamma} = -\mathcal{T}^e_{\phi_0} \tag{6.3.17}$$

$$\mathcal{T}^e_{\theta_0} = F_0\left\{T_0 + T_1(\alpha_2+\alpha_1) + T_2(\alpha_2-\alpha_1)\cos[2(\gamma-\phi_0)]\right\} \tag{6.3.18}$$

$$\mathcal{T}^e_{\alpha_1} = -\frac{F_0}{2\alpha_1}\left\{P_0 + P_1(\alpha_2-\alpha_1) + P_2(\alpha_2+\alpha_1)\cos[2(\gamma-\phi_0)]\right\} \tag{6.3.19}$$

$$\mathcal{T}^e_{\alpha_2} = -\frac{F_0}{2\alpha_2}\left\{P_0 - P_1(\alpha_2-\alpha_1) - P_2(\alpha_2+\alpha_1)\cos[2(\gamma-\phi_0)]\right\} \tag{6.3.20}$$

where the polynomials Q_i e T_i $(i = 0, 1, 2)$ are given by:

$$\begin{cases} Q_0 &= \pi^2\phi_1\left(6\theta_0^2 - \frac{10}{3}\theta_0^4\right) \\ Q_1 &= 0 \\ Q_2 &= \phi_1\left[(A-B)\left(1-\frac{1}{3}\phi_1^2\right)\theta_0^2 - (A-1)\left(\frac{1}{8}-\frac{1}{32}\phi_1^2\right)\theta_0^4\right] \end{cases} \tag{6.3.21}$$

$$\begin{cases} T_0 &= \pi^2\left[\left(8+6\phi_1^2\right)\theta_0 + \left(2(A-1) - \frac{20}{3}\phi_1^2\right)\theta_0^3\right] \\ T_1 &= 2(A+B)\theta_0 - \frac{3}{4}(A-1)\theta_0^3 \\ T_2 &= -(A-B)\left(2-\phi_1^2+\frac{1}{6}\phi_1^4\right)\theta_0 + \\ &\quad + \frac{A-1}{4}\left(3-\phi_1^2+\frac{1}{8}\phi_1^4\right)\theta_0^3 \end{cases} \tag{6.3.22}$$

To the same approximation, the optical contributions to the torques $\mathcal{T}_i$ are given by

$$\mathcal{T}^o_{\phi_0} = \frac{\sigma P}{\omega}\left[Z(1-\cos\alpha) - \frac{\alpha^2 G_{4,0}(\alpha)}{6\beta}[3\delta Z + 2(2-6\delta)Z_2]\right] \tag{6.3.23}$$

$$\mathcal{T}^o_{\phi_1} = -\frac{\sigma P}{\omega}\left[2Z\alpha G_{2,1}(\alpha) - \frac{\alpha^2 G_{4,1}(\alpha)}{6\beta}[3\delta Z + 2(2-6\delta)Z_2]\right] \tag{6.3.24}$$

$$\begin{aligned} \mathcal{T}^o_\gamma &= -\tfrac{P}{\omega}(\alpha_1-\alpha_2)(w_1^2-w_2^2)\sin 2\gamma \\ &\quad \left[\tfrac{Z^3\alpha}{8} - \tfrac{\alpha^2}{64\beta}[3\delta Z^3 - 4(3\delta-1)Z_2^3]\right] \end{aligned} \tag{6.3.25}$$

$$\mathcal{T}^o_{\theta_0} = -\frac{P}{\omega}\left[Z(\beta\alpha)^{1/2} - \frac{(\alpha)^{3/2}}{8\sqrt{\beta}}[3\delta Z - 4(3\delta-1)Z_2]\right] \tag{6.3.26}$$

$$\mathcal{T}^e_{\alpha_1} = \frac{P}{\omega}\left[\frac{B_1 Z^3\alpha}{6} - \frac{\alpha^2}{16\beta}[\delta B_1 Z^3 - 4(3\delta-1)C_1 Z_2^3]\right] \tag{6.3.27}$$

$$\mathcal{T}^e_{\alpha_2} = \frac{P}{\omega}\left[\frac{B_2 Z^3\alpha}{6} - \frac{\alpha^2}{16\beta}[\delta B_2 Z^3 - 4(3\delta-1)C_2 Z_2^3]\right] \tag{6.3.28}$$

where $\sigma = \pm 1$ depends on the polarization helicity, P is the power of the incident beam, ω is the optical frequency, $\delta = 1 - n_o^2/n_e^2$, $\beta = \pi n_o \delta L/2\lambda$, and $\alpha = \beta\theta_0^2$ is the small distortion expression for the phase difference accumulated by the extraordinary and ordinary waves in traversing the sample. Moreover, in Eqs. (6.3.23-6.3.28) we posed

$$G_{m,n}(\alpha) = \int_0^1 dz\, \sin^m(\pi z)\cos^n(\pi z)\sin\left[\alpha\left(z - \frac{\sin\pi z}{2\pi}\right)\right], \tag{6.3.29}$$

$$\begin{cases} B_1 &= \frac{3}{4}(w_x^2\cos^2\gamma + w_y^2\sin^2\gamma + \frac{1}{2}w_x^2w_y^2\alpha_2) \\ \\ B_2 &= \frac{3}{4}(w_y^2\cos^2\gamma + w_x^2\sin^2\gamma + \frac{1}{2}w_x^2w_y^2\alpha_1) \end{cases} \tag{6.3.30}$$

$$\begin{cases} C_1 &= \frac{1}{4}(w_x^2\cos^2\gamma + w_y^2\sin^2\gamma + w_x^2w_y^2\alpha_2) \\ \\ C_2 &= \frac{1}{4}(w_y^2\cos^2\gamma + w_x^2\sin^2\gamma + w_x^2w_y^2\alpha_1) \end{cases} \tag{6.3.31}$$

$$\begin{cases} Z &= Z(\alpha_1,\alpha_2,\gamma) = [1+\alpha_1(B_1-C_1)+\alpha_2(B_2-C_2)]^{-1/2} \\ Z_2 &= Z(2\alpha_1,2\alpha_2,\gamma) \end{cases} \tag{6.3.32}$$

The quantities Z and Z_2 have a simple geometrical meaning. They represent, in fact, the superposition integrals of the profiles of θ^2 and θ^4 as obtained from Eq. (6.3.2) with the profile of the intensity I of the incident wave, viz. $Z = \theta_0^{-2}I_0^{-1}\int\theta^2 I\,dxdy$, $Z_2 = \theta_0^{-4}I_0^{-1}\int\theta^4 I\,dxdy$, $I_0 = 2P/(\pi w_x w_y)$. Looking at expressions of the optical torques, we may identify the right-hand side of Eq. (6.3.23) as the expression of the overall photon spin angular momentum $(P/\omega)\Delta s_3$ and the right-hand side of Eq. (6.3.25) as the expression of the overall photon orbital angular momentum $(P/\omega)\Delta L_z$ transferred to the sample in our approximation[3]. The Z factors appearing in these expressions come from averaging over the not uniform index and light intensity transverse profiles.

From Eq. (6.3.25) we see that ΔL_z vanishes in the case of a laser beam having circular cross section ($w_x = w_y$) and it is proportional to $\sin 2\gamma$. Another interesting feature of our model is that the elastic torques $\mathcal{T}^e_{\phi_0}$ and $\mathcal{T}^o_\gamma$ are opposite. They are indeed internal elastic torques tending to align γ to ϕ_0. The existence of these internal torques is related to the elastic anisotropy of the material and to the consequent lack of invariance of the elastic free energy when the director is rotated. When the torques acting on ϕ_0 and γ are added together, the internal elastic torques cancels out, and we recover the total angular momentum balance.

The ODE's of our model were solved by standard Runge-Kutta routine using tabulated values of the material constants of E7 at room temperature, namely

[3] ΔL_z refers to one photon

$k_{11} = 11.09{\cdot}10^{-7}$ dyne, $k_{22} = 5.82{\cdot}10^{-7}$ dyne, $k_{33} = 15.97{\cdot}10^{-7}$ dyne, $n_o = 1.52$, $n_e = 1.73$, were k_{ii} $(i = 1, 2, 3)$ are the material elastic constants for splay, twist and bend, and n_o, n_e are the ordinary and extraordinary refractive indices, respectively. The sample thickness used in this simulation was L= 50μm.

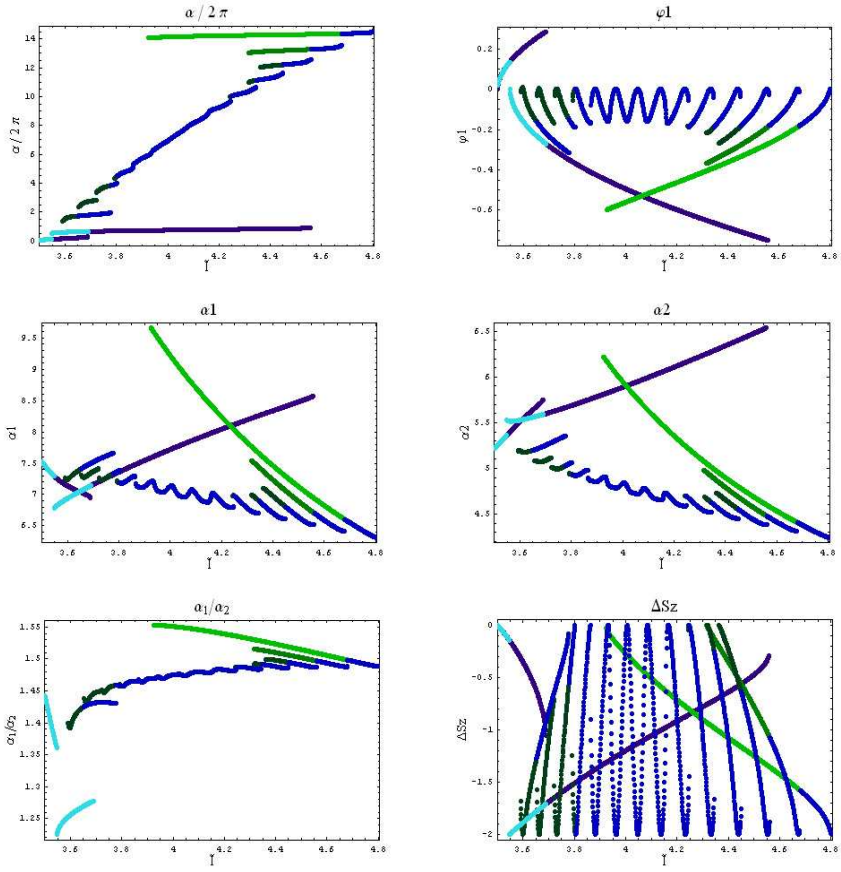

Figure 6.6: Numerical integrations results. - part 1.
$\tilde{I}$ represents the normalized laser intensity.

In figures 6.6 and 6.7 are shown the results of the numerical integration of the above described model performed in a configuration resembling our experimental geometry (beam with transverse circular profile and beam waists

$w_x = w_y = 50\mu$m: we are thus excluding orbital angular momentum effects).

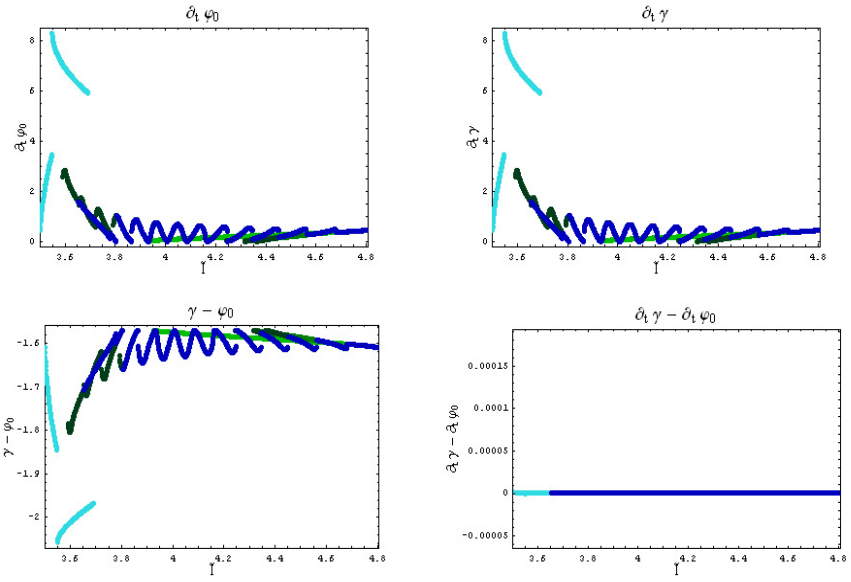

Figure 6.7: Numerical integrations results. - part 2.

Every picture shows the values of the model parameters p_i at a given power value and on a certain dynamical branch. The parameter α shown in figure 6.6 is related tho the amplitude n of the reorientation pattern (see eq. (5.5.17)) is related by means of the relation $\alpha = 2n$. The parameters α_1 and α_2 correspond to σ_x and σ_y. The different colors in the simulations are chosen in accordance with the following convention: blue tonalities are used for integrations in which the intensity was increased at every integration step while green tonalities were used when the intensity was decreased.

Such integrations (and the other performed using different parameter values) show anyway that a beam circularly shaped and impinging on an elastically anisotropic nematic LC gives rise to a reorientation pattern that is elliptically shaped[4] (see in figure 6.6 the part relative to the ratio α_1/α_2) and *rotates*, exactly like experimental observations suggest: ϕ_0 and γ grow with the time with

[4]The pattern becomes circularly shaped only in the case of the elastically isotropic LC, that is when $A = B$.

the same velocity (see figure 6.7) while the other parameters are time independent. Please note that, although ϕ_0 and γ rotate with same angular velocity, they have different values and their difference depends upon the intensity value and the other parameters.

6.3.1 Search for a rigidly rotating solution

From eqs. (6.3.9) the dynamic equation for γ and ϕ_0 are:

$$\begin{cases} \dot{\gamma} &= m_{\gamma,j}\, \mathcal{T}_j \\ \\ \dot{\phi}_0 &= m_{\phi_0,j}\, \mathcal{T}_j \end{cases} \tag{6.3.33}$$

where $m_{i,j}$ are the matrix elements of M. From eq. (6.3.11) it is easy too see that M acts diagonally on both γ and ϕ_0; eqs (6.3.33) will therefore be:

$$\begin{cases} \dot{\gamma} &= m_{\gamma,\gamma}\, \mathcal{T}_\gamma = m_{\gamma,\gamma}\, \mathcal{T}^e_\gamma + m_{\gamma,\gamma}\, \mathcal{T}^o_\gamma \\ \\ \dot{\phi}_0 &= m_{\phi_0,\phi_0}\, \mathcal{T}_{\phi_0} = m_{\phi_0,\phi_0}\, \mathcal{T}^e_{\phi_0} + m_{\phi_0,\phi_0}\, \mathcal{T}^o_{\phi_0} \end{cases} \tag{6.3.34}$$

For sake of simplicity, let's denote $m_{\phi_0,\phi_0} = m_{\phi_0}$ and $m_{\gamma,\gamma} = m_\gamma$. Remembering that

$$\mathcal{T}^e_\gamma = -\mathcal{T}^e_{\phi_0} \tag{6.3.35}$$

for sake of simplicity we call it the internal torque $\mathcal{T}_{\text{int}}$. Expressing then the optical torques as:

$$\begin{cases} \mathcal{T}^o_{\phi_0} = \frac{P}{\omega}\, \Delta S_3 \\ \\ \mathcal{T}^o_\gamma = \frac{P}{\omega}\, \Delta L_z \end{cases} \tag{6.3.36}$$

eqs. (6.3.34) become:

$$\begin{cases} \dot{\gamma} &= m_\gamma \mathcal{T}_{\text{int}} + m_\gamma\, \frac{P}{\omega}\, \Delta L_z \\ \\ \dot{\phi}_0 &= m_{\phi_0} \mathcal{T}_{\text{int}} + m_{\phi_0}\, \frac{P}{\omega}\, \Delta S_3 \end{cases} \tag{6.3.37}$$

Since we are considering beams with transverse circular profile, there will be no orbital angular momentum transfer and $\Delta L_z = 0$. Since we are looking for a rigid solution, we make the *Ansatz* that $\gamma - \phi_0 = \text{cost.}$; since, from eq. (6.3.23)

$\mathcal{T}_{\rm int} = \mathcal{T}_{\rm int}(\gamma - \phi_0)$, our *Ansatz* implies that the internal torque too has to be constant. Moreover, $\gamma - \phi_0 = \text{cost.} \Rightarrow \dot{\gamma} = \dot{\phi_0}$. Let's call their angular velocity Ω:

$$\Omega = \dot{\gamma} = \dot{\phi_0}. \tag{6.3.38}$$

Under such assumptions eqs. (6.3.37) become:

$$\begin{cases} \Omega &= m_\gamma \mathcal{T}_{\rm int} \\ \\ \Omega &= m_{\phi_0} \mathcal{T}_{\rm int} + m_{\phi_0} \frac{P}{\omega} \Delta S_3 \end{cases} \tag{6.3.39}$$

Multiplying the first equation for m_{ϕ_0} and the second one for m_γ and adding them together member by member, we obtain:

$$(m_{\phi_0} + m_\gamma)\Omega = m_{\phi_0} m_\gamma \frac{P}{\omega} \Delta S_3 \tag{6.3.40}$$

and finally

$$\Omega = \frac{m_{\phi_0} m_\gamma}{(m_{\phi_0} + m_\gamma)} \frac{P}{\omega} \Delta S_3 \tag{6.3.41}$$

This result is indeed very important because, for ordinary LC, elastic anisotropies are very small ($\Delta k/k \ll 1$) and thus $\alpha_1 - \alpha_2 \simeq 0$. If one sees at the expression of the matrix M would then understand that the term m_γ will be much greater with respect to m_{ϕ_0}. Expanding for small m_{ϕ_0} we then obtain:

$$\Omega \approx \frac{P}{\omega} \Delta S_3. \tag{6.3.42}$$

This result is very important because on one side it is coherent with paste experiments [Santamato et al. (1986, 1987, 1988)] but contemporary on the other side allows the existence of our rigidly rotating solution; the one doesn't exclude the other.

Chapter 7

Cholesteric samples

In this chapter we'll report our observations performed on cholesteric samples with our new detection apparatus. The mixture used, as anticipated in section 5.6, was obtained by solving some chiral molecules (C15 from Merck) into the nematic E7. The concentration of the used mixture is $c_{C15} = 1.31 \pm .0.01\%$.

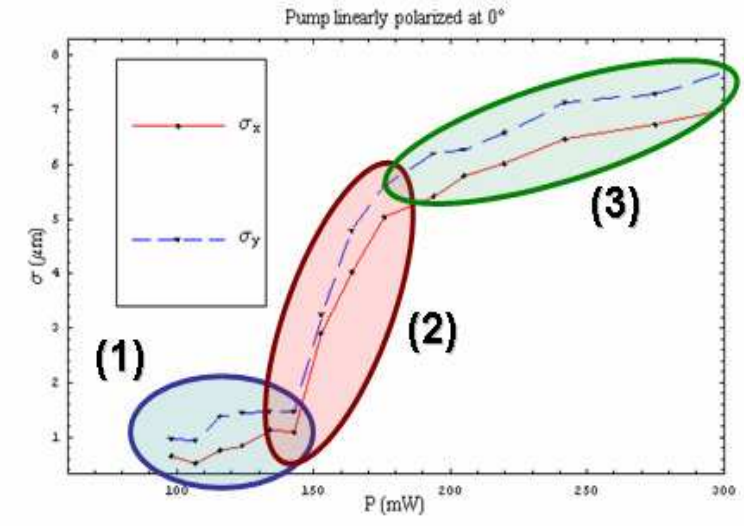

Figure 7.1: Linearly polarized impinging light: spatial extension of the reorientation pattern.

7.1 Linearly polarized light

Under linearly polarized pump light our cholesteric samples had three different kind of responses, as shown in figures 7.1, 7.2 and 7.3, where are reproduced,

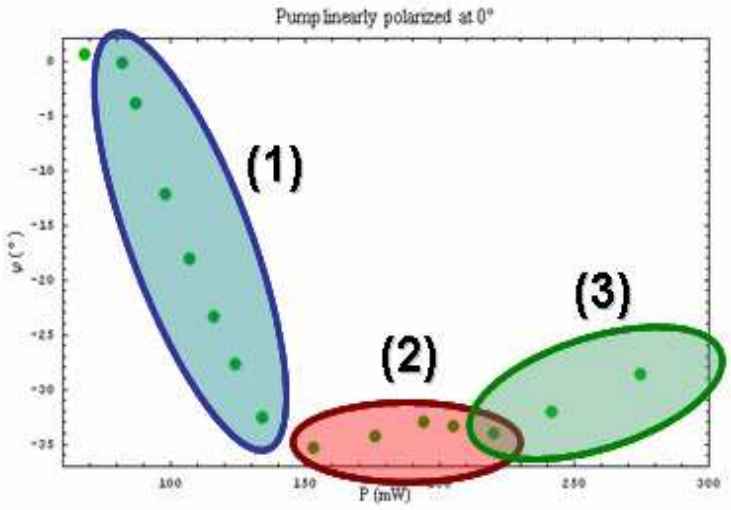

Figure 7.2: Linearly polarized impinging light: φ values obtained from the polarimeter.

respectively, the value of the reoriented pattern extension (σ_x and σ_y), φ's value (taken from the polarimeter) and γ's value (taken from microscope pictures). In the pictures we have distinguished three regions: (1), (2) and (3).

- **region (1):**
  `O.P.L. region.` In this range the value of the induced birefringence in the sample remains frozen. As expected from the authors of ref. [Abbate et al. (1996)] the excess energy stored into the sample, that cannot induce a sample birefringence increase, twists the structure, providing a polarization-rotator effect ($\lambda/2$-like). In fact, if one considers the behaviour of φ: the light emerging from the sample is polarized along a direction that depends from the pump power. In this region γ's remains constant (the reoriented pattern doesn't rotate).

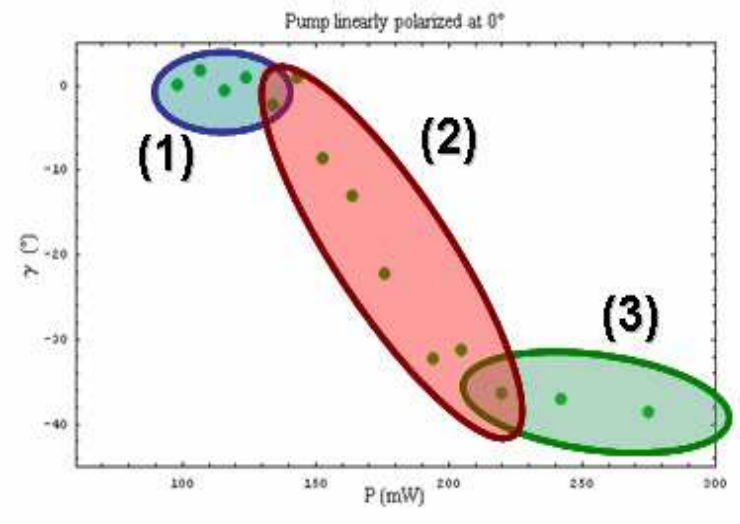

Figure 7.3: Linearly polarized impinging light: γ values gained from the pictures.

- **region (2):**
  In this region φ remains constant while the reorientation pattern grows and rotates: σ_i and γ grow very rapidly. Thus, in this range, the energy excess increases the sample birefringence and doesn't increase the twist of the structure.

- **region (3):**
  In this last region all the systems parameters grow slowly: the reoriented pattern grows (σ_i increase), rotates (γ increases) and φ changes.

It seems thus that these measurements confirm the physical pictures conjectured from the authors of reference [Abbate et al. (1996)].

7.2 Circularly polarized light

As anticipated in section 3.5, a cholesteric sample, because of its intrinsic helicity due to its chirality, distinguishes, unlike nematics, between left-handed and right-handed circularly polarized light. Thus we have to consider the two cases

separately.

7.2.1 Concordant helicities: light circularly polarized (σ_-)

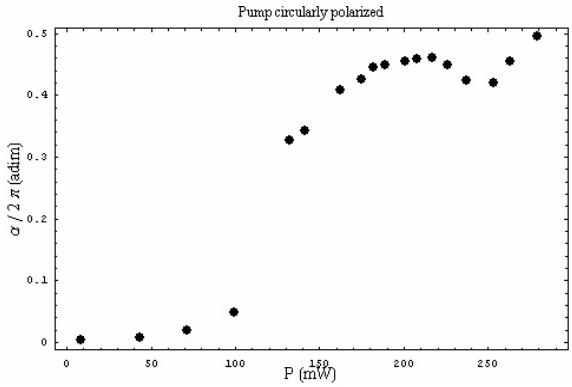

Figure 7.4: Circularly polarized light with the same helicity of the cholesteric helix (σ_-): $\alpha/2\pi$.

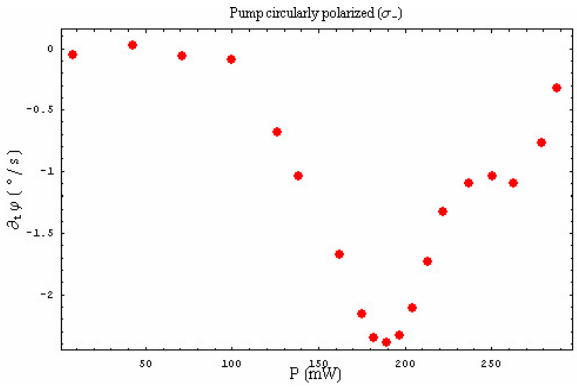

Figure 7.5: Circularly polarized light with the same helicity of the cholesteric helix (σ_-): angular velocity $\partial_t\ \varphi$.

In this case too the authors of reference [Abbate et al. (1996)] and the authors of the more recent work [Brasselet et al. (2005)] made some predictions based on their theoretical model.

They observed in this case, as in the case of linearly polarized pump, an optical phase locked phase, after which the system jumped abruptly to a highly distorted state. Their model predicted besides the presence of director's rotations, in some specific experimental parameters range, but they didn't observed them.

From figure 7.4 appears clear that the system remains in OPL state after which jumps on an highly distorted state (not represented in figure). If one considers instead figure 7.5 one can see that the predictions were true: the director rotates.

7.2.2 Discordant helicities: light circularly polarized (σ_+)

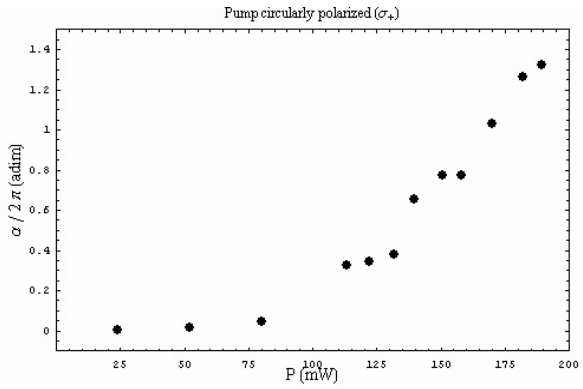

Figure 7.6: Circularly polarized light with the same helicity of the cholesteric helix (σ_+): $\alpha/2\pi$.

The results obtained in this configuration are in contrast with the predictions made by the above cited authors.

In fact they predicted the absence of the OPL state and the absence of director's rotation.

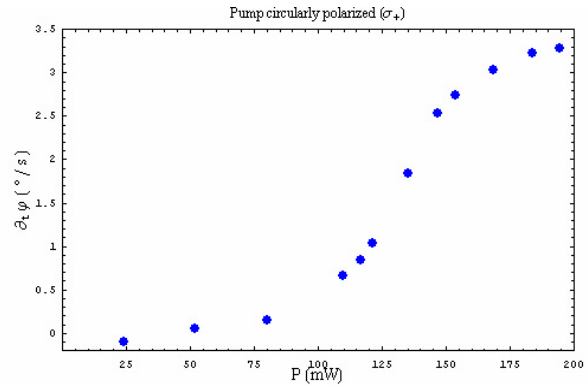

Figure 7.7: Circularly polarized light with the same helicity of the cholesteric helix (σ_+): angular velocity $\partial_t\ \varphi$.

As one can see from figure 7.6, there is indeed no OPL: the sample birefringence grows with the pump power. The great contrast between theoretical predictions and experimental observations comes out when we consider φ's behaviour: it rotates too (see figure 7.7).

The discrepancy between the models and experimental observations is probably due to the fact that, as in the case of nematics, the models are developed in the plane distortion hypothesis ($\hat{\boldsymbol{n}}(\vec{x},t) = \hat{\boldsymbol{n}}(z,t)$) and that, as in the case of nematics, this hypothesis seems to be too crude. In this configurations seems to work the same ($\gamma - \phi_0$) coupling phenomenon present in the nematic case.

An extension of the 3-d model showed in section 6.3 for the case of cholesteric LCs could be probably able to explain such new experimental observations.

7.3 Depolarized light

At last we considered the case of depolarized pump light, for such there are no reference in literature. Our first requirement was the choice of how to become depolarized light. For obtained depolarized light, we followed the method adopted in reff. [Arnone et al. (1996); Marrucci et al. (1998)], that is we made

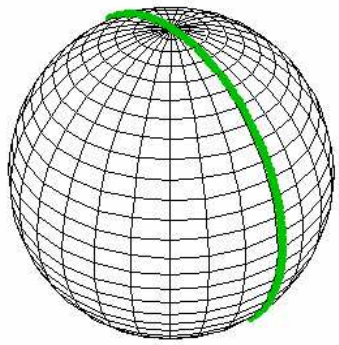

Figure 7.8: A path on Poincarè's sphere equivalent to the one described by eqs. (7.3.1)

the pump polarization vary very rapidly (that is, rapidly than the molecular response time) by means of an electro-optic device (a Pockel's cell).

The choice of how to drive the Pockel's cell was very critical. In references [Arnone et al. (1996); Marrucci et al. (1998)], the cell was driven by a saw-tooth voltage function (with period T) oscillating between two different voltages, chosen to produce the polarization dynamics:

$$\begin{cases} s_1(t) = 0 \\ \\ s_2(t) = \sin(\frac{2\pi t}{T}) \\ \\ s_3(t) = \cos(\frac{2\pi t}{T}) \end{cases} \tag{7.3.1}$$

Such a configuration presents two inconveniences for our purposes: it covers the Poincaré sphere following always the same verse (this problem can be solved by using a triangular wave instead of the saw-tooth) and possesses a privileged direction (45^o in the case of 7.3.1, see figure 7.8 for the path on the Poincarè sphere). This condition is inadmissible for our purposes because a privileged direction could prevent the rotations are we looking for.
For avoiding such problem one could put in rotation around the z axis the Pockel's cell (for varying the privileged direction) but such a solution seems

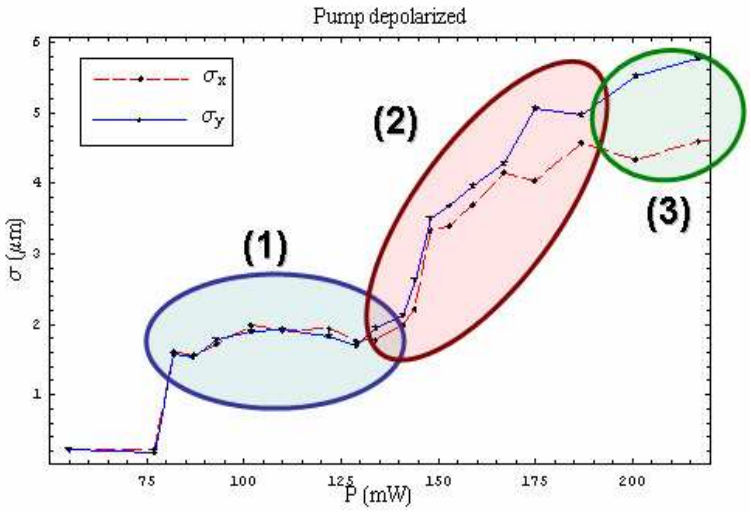

Figure 7.9: Depolarized impinging light: spatial extension of the reorientation pattern.

impracticable. A more feasible solution is to let the system directly jump from one pole on the sphere to the other by driving the cell with a square wave. In such a way the polarization dynamics is:

$$\begin{cases} s_1(t) = 0 \\ \\ s_2(t) = 0 \\ \\ s_3(t) = \sigma(t) \end{cases} \tag{7.3.2}$$

where σ is a square wave jumping from +1 to -1 periodically. In this way the system doesn't possess any preferred direction more.

The results of our observations of the cholesteric behaviour under depolarized light can be again split into three parts:

- **region (1):**
  `O.P.L. region.` In this range the value of the induced birefringence in the sample remains frozen. The sample shows in this case too a polarization-

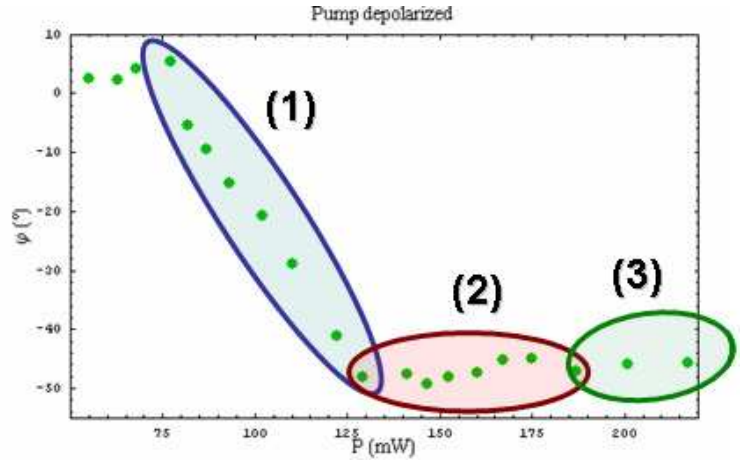

Figure 7.10: Depolarized impinging light: φ values obtained from the polarimeter.

rotator effect ($\lambda/2$-like), almost unexpected indeed since the impinging light is depolarized while the light emerging from the sample is polarized along a direction that depends from the pump power. In this region γ's remains constant (the reoriented pattern doesn't rotate).

- **region (2):**
  In this region φ remains constant while the reorientation pattern grows: σ_i grow while φ and γ are almost constant.

- **region (3):**
  In this last region all the systems parameters grow and γ begins to rotate, as under circularly polarized light.

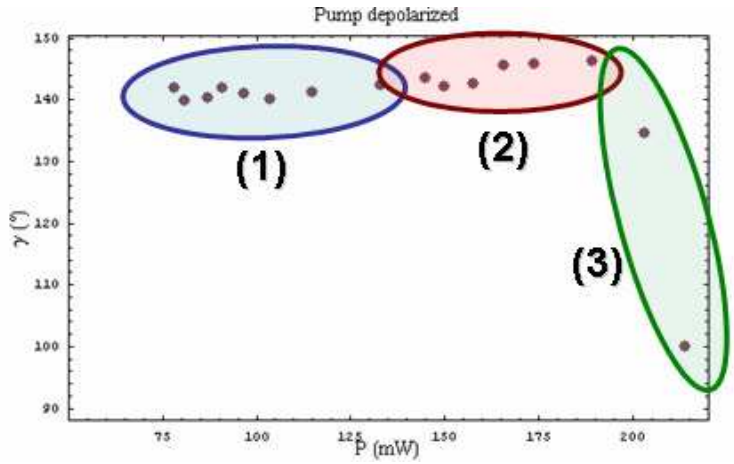

Figure 7.11: Depolarized impinging light: γ values gained from the pictures.

Chapter 8

Electric field effects in cholesterics: the Lehmann rotation

In this last chapter we'll discuss our experimental observations performed on cholesteric samples on which was applied an electric DC field. As mentioned in in chapter 5 the samples were realized with ITO coated glasses.

Two different experimental configurations were performed in this last set of

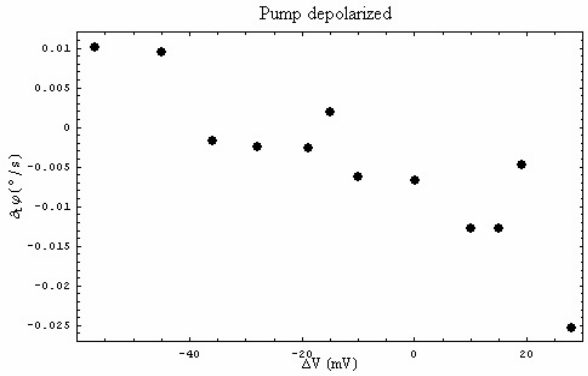

Figure 8.1: Angular velocity versus ΔV. Impinging light power: P = 134 mW.

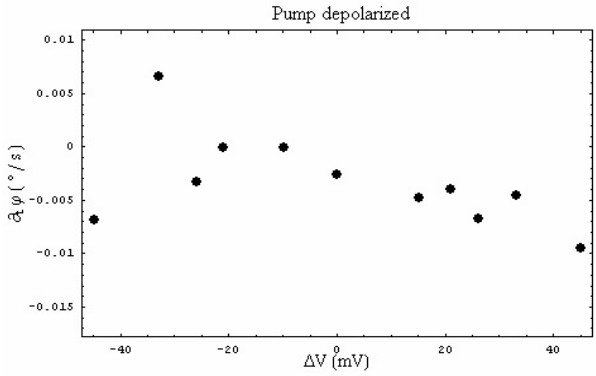

Figure 8.2: Angular velocity versus ΔV. Impinging light power: P = 137 mW.

measurements[1]: the search for the Lehmann rotation for samples reoriented with depolarized light and the study of the competition between the Lehmann torque, due to the cross-couplings, and the spin angular momentum transfer from circularly polarized light.

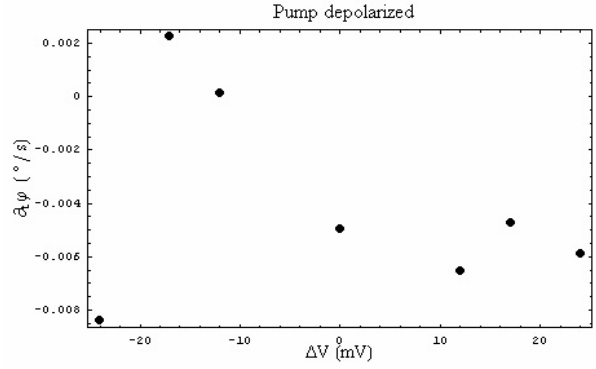

Figure 8.3: Angular velocity versus ΔV. Impinging light power: P = 141 mW.

[1]The movies relative to the measurements reported in this chapter will be available at the web page `http://people.na.infn.it/~anton/PhD.html`.

8.1 Lehmann rotation under depolarized light

The first set of measurements was performed with depolarized light. The choice of such kind of light was taken to avoid the eventuality that the observed rotations were due to the light spin angular momentum transfer, since, as we have

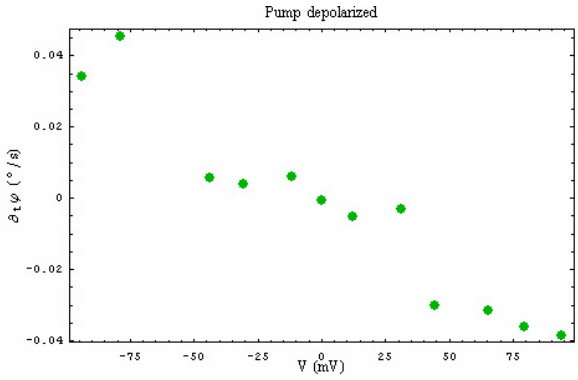

Figure 8.4: Angular velocity versus ΔV. Impinging light power: P = 171 mW.

seen in section 7.2, circularly polarized light induces rotation in cholesteric samples.

In figures 8.1, 8.2, 8.3 and 8.4 is shown the angular velocity versus the applied electric field for different pump powers.

As one can see, the behaviour of the induced angular velocity versus the electric field is linear in the electric field and reverses its sign by reversing the sign of the applied field, as expected from the theory (cfr. eq. 4.1.4).

Please note that these rotation were indeed very slow. The possible causes of such behaviour will be shortly discussed in section 8.3.

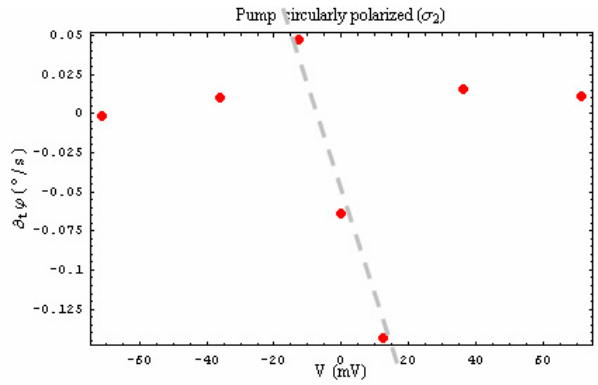

Figure 8.5: Angular velocity versus ΔV. Impinging light (σ_-) power: P = 246 mW.

8.2 Lehmann effect under circularly polarized light

As we have seen in section 7.2, a cholesteric sample, pumped with circularly polarized light, with either the opposite helicities, is put in rotation. The electric

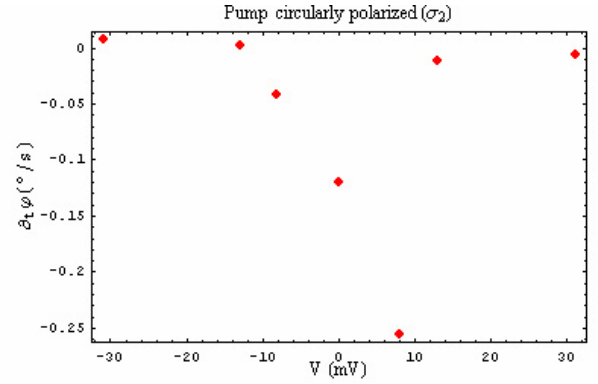

Figure 8.6: Angular velocity versus ΔV. Impinging light (σ_-) power: P = 264 mW.

field will then in such case *compete* with light's spin, giving rise to more complex phenomena. It can so happen that the two torques balance, stopping the

rotation, or cooperate, enhancing the rotation, or, even more, reverting rotation sign.

8.2.1 Concordant helicities: light circularly polarized (σ_-)

In the case of concordant light and cholesteric helix helicities, as we have seen in

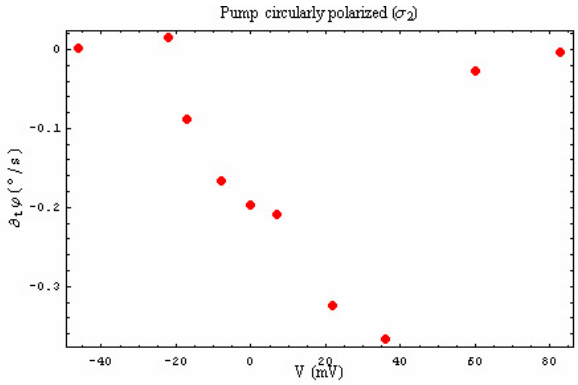

Figure 8.7: Angular velocity versus ΔV. Impinging light (σ_-) power: P = 320 mW.

the preceding chapter, the reoriented pattern rotates anticlockwise (possessing thus negative angular velocity).
The action of the electric field in such configuration is reported in figures 8.5, 8.6 and 8.7. The angular velocity seems to be always linear in the applied electric field, possessing a Lehmann-like behaviour:

$$\omega - \omega_0 \propto -\frac{\nu_{\vec{E}} E}{\gamma}. \tag{8.2.1}$$

where ω_0 possesses a negative value.

Please note the system's behaviour in figure 8.5, where the velocity reverts its sign by inverting the applied field. It is indeed interesting to watch the movies available in the above cited web-page: they show the reoriented pattern rotating clock- and anti-clockwise, depending from the sign of the applied electric field.

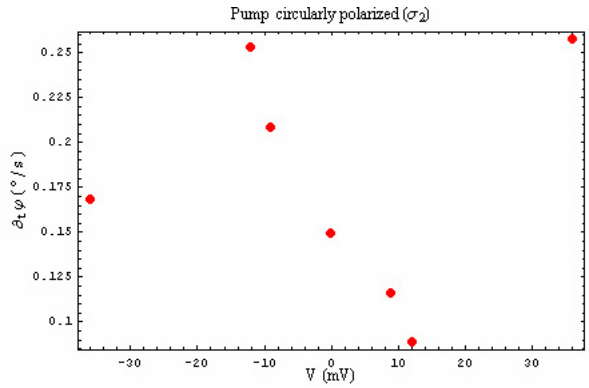

Figure 8.8: Angular velocity versus ΔV. Impinging light (σ_+) power: P = 187 mW.

8.2.2 Discordant helicities: light circularly polarized (σ_+)

In the case of discordant light and cholesteric helix helicities, we have seen that the reoriented pattern rotates clockwise (possessing thus positive angular velocity).

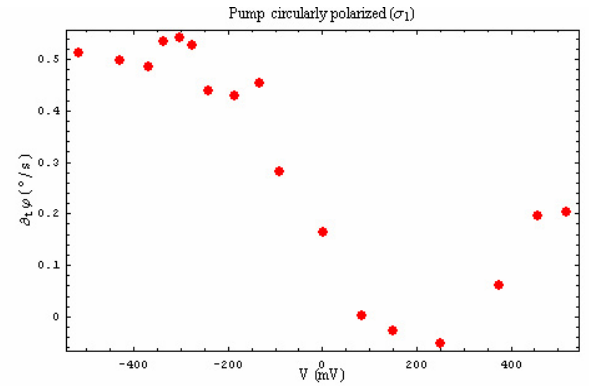

Figure 8.9: Angular velocity versus ΔV. Impinging light (σ_+) power: P = 197 mW.

The sample response to the electric field was always described by a relation like that given in eq. (8.2.1), but this time with positive ω_0 values.

8.3 Open questions

The above described measurements show the occurrence of the Lehmann rotation phenomenon, putting cholesteric LCs in rotation under the action of an applied electrostatic field. It is worth noting that the induced rotation is very slow, unlike the situation Lehmann observed, in which he reported the observation of *violent* rotation of the cholesteric drops.

The cause of such slow rotation could depend from two different factors, on which we are actually focusing our attention: the homeotropic anchoring on ITO and the generation of space charge.

8.3.1 Anchoring on ITO

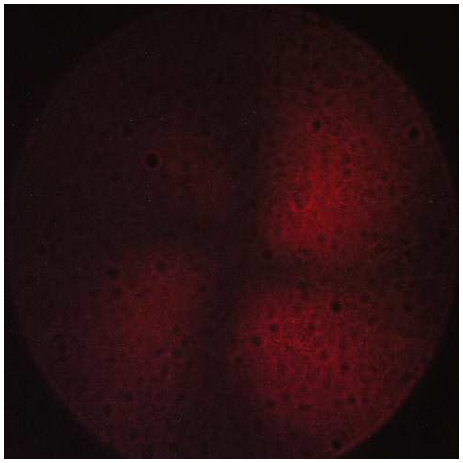

Figure 8.10: The cholesteric reorientation pattern above threshold in samples with ITO coated glasses.

Samples realized with ITO coated glasses show a very particular behaviour above OFT threshold. From consideration from the inhomogeneous retarder waveplate model 5.5.17 and from the observations performed on the same mixture put in cells without ITO deposition, the reoriented pattern is expected to

be elliptically shaped. As one can see in figure 8.10, the experimental observed pattern has a hollow cross in its middle. Increasing the pump value, the cross vanishes and the system behaves "normally", as expected.

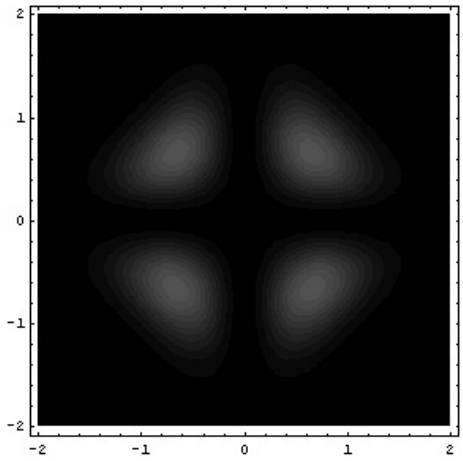

Figure 8.11: Simulation of the observed pattern by supposing the φ profile being not uniform.

The nature of this cross is still not very clear although it resembles very closely the conoscopic figures one observe illuminating an uniaxial crystal with convergent light. This could suggest an interpretation for the observed cross: reversing the physical picture, it could be that the parallel probe light impinges on the sample with non-perfectly-orthogonal aligned. In figure 8.11 is simulated how the reoriented pattern would appear if one suppose that the impinging light induces a nonuniformity in the φ profile (supposed to be hyperbolic). This simulation seems to provide a step toward the comprehension of the experimental observation.

Such problem is related to the slow rotation observed in our experiments because we decided to work, to avoid the occurrence of the hollow cross, far from the threshold and thus in a highly distorted state, where the pattern is expected to rotate very slowly.

A better anchoring is thus desirable because could let us work in the slightly-above threshold region, where the structure should rotate quicklier and, moreover, the flexoelectric effect is negligible.

At last, the anchoring on ITO coated glasses seems to possess a very short mean life: after few hours of pump illumination the anchoring breaks out and the cell remains *written*. A stronger anchoring could maybe improve the cells duration.

8.3.2 Space charge generation

The other open question is whether, applied the electric field, a space charge is generated and reaches the electrodes/cell walls -screening the applied electric field- or not. It is important to understand if this phenomenon takes place or not because, in affirmative case the effective electric field could be of order of magnitude smaller then the external applied field, giving rise to slower rotations.

An hint that this could be the situation comes from a dust contaminated sample (probably full of impurities), in which, reverting instantaneously the sign of the electric field, due to the charge redistribution, the reorientation pattern was destroyed and reformed within a minute. In cleaner samples this effect doesn't happen (by reverting instantaneously the sign of the electric field the pattern inverts its velocity without redistribution phenomena); that could not exclude the presence of spatial charge but ensures that its density is much lower. The question that remains still open is whether is low enough to neglect the external field screening effect.

A way of estimating the effective value of the electric field within the sample is obtained by considering the competition between light and electric field: by measuring the electric field intensity required to make *close* the light reoriented pattern, one could obtain the value of the *real* applied electric field.

Conclusions

The aim of the present work is the search for the Lehmann rotation induced by an electrostatic field, an intriguing phenomenon – involving cross-couplings between thermodynamical forces and fluxes of different vectorial nature – observed at the beginning of the research on LCs and never replicated in an clear and unequivocal way.
The idea behind this work was to realize a clever experimental configuration in which every other contributing factor would be excluded and the rotation could be ascribed only to the cross-couplings. To this purpose, we realized a long pitch cholesteric sample frustrated by the strong homeotropic anchoring to behave like a nematic LC. Illuminating the sample with a focused laser beam we were then able to create a thin cholesteric region (equivalent of the cholesteric drop in the Lehmann experiment) -surrounded by a nematic environment- whose characteristics could be set at will and whose axis is automatically along the z direction.

With this goal in mind, we mounted a detection apparatus that could gain information about the molecular reorientation state in every power range. The system is evolved through different stages; finally we chose as detection apparatus a revisited version of the polarized microscope. This configuration has revealed itself surprisingly sensitive: it furnishes the picture of the whole transverse reorientational profile within the sample and not only its amplitude (as the detection systems based on the far-field self-diffraction rings do).

A first unexpected result was obtained analyzing with our detection appara-

tus the response of a nematic sample to circularly polarized light. We observed that the light put in rotation not only the molecular director but also the whole reoriented pattern, that was put in rotation as a single rigid crystal. Such unexpected coupling between θ and φ was never observed before. For a fitting description of such phenomenon one needs to go beyond the plane-wave approximation in developing a model; a 3-D model, which accounts fairly well for the experimental observations, has been described within this work.

The analysis of cholesteric samples has given unexpected results too. In the case of circularly polarized impinging light, for example, we found the sample rotating. Such result was predicted from a very recent numerical model [Brasselet et al. (2005)] but was never observed before. For linearly polarized light we checked the hypothesis made in [Abbate et al. (1996)]: a cholesteric sample, in the Optical Phase Locked region acts like a rotator, rotating the direction of the linearly polarized impinging light. Moreover we performed an analysis of the response of cholesteric samples to depolarized light.

Having characterized the behaviour of the samples with our new detection apparatus, we could finally begin our search for the light-assisted Lehmann rotation induced by an electrostatic field. When the cholesteric "droplet" was created by the depolarized light, the system showed the same features of the Lehmann rotation: it was put into rotation by the electric field, the rotational velocity was linear in the applied field and reverted its sign by inverting the electric field, as predicted by the theory.
When the cholesteric "droplet" was created instead by circularly polarized light, we could observe the competition between the light spin angular momentum transfer to the cholesterics and the Lehmann torque induced by the electrostatic field. By varying opportunely the electric field intensity we was able to regulate, at will, the molecular rotation, increasing or stopping it.

It is worth noting that, due to the big amount of unexpected and never before observed effects contained in this work, there is still much to do, both from the experimental and from the theory point of view. The problem of increasing

the quality of the anchoring of the ITO coating is an example as is also the extension of our 3D model to the case of cholesterics under static electric field. Also the space charge in the sample is a problem to be faced on.

Appendix A

Proposal for a better polarimeter

Putting at the entrance of the polarimeter stage described in section 5.2 (figure 5.2) a retardation waveplate with delay that increases with the time (as an example, a Pockels cell driven by a saw-tooth signal) with slope ω_p and fixes its easy axis at 45^o with respect to the reference direction, the photodiode signal is given by:

$$\begin{aligned} s(t) \quad \propto \quad & 4S_0 + 4S_0 \cos 2\Omega t + 4S_2 \sin 2\Omega t + \\ & + 2S_1 \cos \omega_p t - 2S_3 \sin \omega_p t + \\ & + 2S_1 \cos\Big[(2\Omega - \omega_p)t\Big] + 2S_3 \sin\Big[(2\Omega - \omega_p)t\Big] + \\ & + 2S_1 \cos\Big[(2\Omega + \omega_p)t\Big] - 2S_3 \sin\Big[(2\Omega + \omega_p)t\Big] + \\ & + S_1 \cos\Big[(4\Omega - \omega_p)t\Big] + S_3 \sin\Big[(4\Omega - \omega_p)t\Big] + \\ & + S_1 \cos\Big[(4\Omega + \omega_p)t\Big] - S_3 \sin\Big[(4\Omega + \omega_p)t\Big]. \end{aligned} \tag{A.0.1}$$

A lock-in working in the dual reference mode would then give the following

phase X and quadrature signals Y:

$$\begin{cases} X_{2\Omega} = 4S_0 \\ Y_{2\Omega} = 4S_2 \\ X_{\omega_p} = 2S_1 \\ Y_{\omega_p} = -2S_3 \end{cases} \tag{A.0.2}$$

In this way all Stokes' parameters can be directly measured on independent channels (instead of calculating S_3 from the other parameters, as in the case of the polarimeter used in this thesis).

Bibliography

Abbate, G., Ferraiuolo, A., Maddalena, P., Marrucci, L., and Santamato, E., 1993, *Optical Reorientation in Cholesteric-nematic Mixtures*: Liq. Cryst., **14**, 1431.

Abbate, G., Arnone, G., Lauria, A., Maddalena, P., Marrucci, L., Paparo, D., and Santamato, E., 1996, *Nonlinear effect in nematics doped by dyes and chiral agents* in Novel Optical Materials and Applications, cap. 5 John Wiley & Sons, Inc.

Arnone, G., Sirleto, L., Marrucci, L., Maddalena, P., and Santamato, E., 1996, *Optical Frédericksz Transition Induced by Depolarized Light*: Mol. Cryst. Liq. Cryst., **282**, 191–204.

Brasselet, E., Krimer, D., and Kramer, L., 2005, *Light-induced competition instabilities driven by competing helical patterns in long-pitch cholesterics*: Eur. Phys. Journ. E, **17**, 403–411.

Chandrasekhar, S., 1977, *Liquid Crystals*: Cambridge University Press, Cambridge.

Curie, P., 1894, *Sur la symétrie dans les phénomènes physiques, symétrie d'un champ électrique et d'un champ magnétique*: J. de Phys., **3 série, t. III**, 393.

de Gennes, P. G., 1974, *The Physics of Liquid Crystals*: Oxford University Press, Oxford.

de Groot, S., and Marur, P., 1962, *Non-equilibrium thermodynamics*: Amsterdam, North-Holland.

Durbin, S. D., Arakelian, S. M., and Shen, Y. R., 1981, *Optical-Field-Induced Birefringence and Fréedericksz Transition in a Nematic Liquid Crystal*: Phys. Rev. Lett., **47**, 1411.

Éber, N., and Jánossy, I., 1982, *An experiment on the thermomechanical coupling in cholesterics*: Mol. Cryst. Liq. Cryst., **72**, 233–238.

Éber, N., and Jánossy, I., 1984, *Thermomechanical coupling in compensated cholesterics*: Mol. Cryst. Liq. Cryst., **102**, 311–316.

Fréedericksz, V., and Zolina, V., 1933, *Forces causing the orientation of an anisotropic liquid*: Trans. Faraday Soc., **29**, 919.

Gil, L., and Gilli, J., 1998, *Surprising Dynamics of Some Cholesteric Liquid Crystal Patterns*: Phys. Rev. Lett., **80**, 5742–5745.

Kamien, R., and Seilinger, J., 2001, *Order and frustration in chiral liquid crystals*: J.Phys.: Condens. Matter, **13**, R1.

Lehmann, O., 1900, *Structur, System und magnetisches Verhalten flüssiger Kristalle und deren Mischbarkeit mit festen*: Annalen der Physik, **Vierte Folge, Band 2, n. 8**, 649–705.

Leslie, F., 1968, *Some thermal effects in cholesteric liquid crystals*: Proc. Roy. Soc. A, **307**, 359–372.

Leslie, F., 1969, *Continuum theory of cholesteric liquid crystals*: Mol. Cryst. Liq. Cryst., **7**, 407–420.

Leslie, F., 1971, *Thermo-mechanical coupling in cholesteric liquid crystals*: Symposia of the Faraday Society, **5**, 333–340.

Maddalena, P., Arnone, G., Abbate, G., Marrucci, L., and Santamato, E., 1995, *Optically induced reoriantation in nematics doped by chiral agents*: Mol. Cryst. Liq. Cryst., **261**, 113–122.

Madhusudana, N., and Pratibha, R., 1989, *An experimental investigation of electromechanical coupling in cholesteric liquid crystals*: Liquid Crystals, **5**, 1827–1840.

Madhusudana, N., Pratibha, R., and Padmini, H., 1991, *Electromechanical Effect in Cholesteric Liquid Crystals with Fixed Boundary Conditions*: Mol. Cryst. Liq. Cryst., **202**, 35–49.

Marrucci, L., Maddalena, P., Arnone, G., Sirleto, L., and Santamato, E., 1998, *Liquid Crystal Reorientation Induced by Completely Unpolarized Light*: Phys. Rev. E, **57**, no. 3, 3033–3037.

Mauguin, C., 1911, *Sur les cristaux liquides de Lehmann*: Bull. Soc. Franc. Mineral., **34**, 71–85.

Meyer, R., 1969, *Piezoelectric effects in liquid crystals*: Phys. Rev. Lett., **22**, 1918.

P. Oswald, J. B., and Pirkl, S., 2000, *Static and dynamic properties of cholesteric fingers in electric field*: Phys.Rep., **337**, 67.

Patel, J., and Meyer, R., 1987, *Flexoelectric Electro-optics of a Cholesteric Liquid Crystal*: Phys. Rev. Lett., **58**, 1538.

Piccirillo, B., Vella, A., Setaro, A., and Santamato, E., 2005, *Nonlinear dynamics induced in liquid crystals by the competition between the orbital and the spin angular momentum of light*: submitted to PRE.

Pomeau, Y., 1971, *Phénomènes de transport pour des molecules optiquement actives*: Phys.Lett., **34A**, 143.

Santamato, E., and Shen, Y. R., 1985, *Field-Curvature Effects in Spatial Self-Phase Modulation of Laser Radiation in a Liquid Crystal Film*: Opt. Lett., **9**, 564.

Santamato, E., Daino, B., Romagnoli, M., Settembre, M., and Shen, Y. R., 1986, *Collective Rotation of Molecules Driven by the Angular Momentum of Light in a Nematic Film*: Phys. Rev. Lett., **57**, no. 19, 2423–2426.

Santamato, E., Daino, B., Romagnoli, M., Settembre, M., and Shen, Y. R., 1987, *Collective Rotation of the Molecules of a Nematic Liquid Crystal Driven by the Angular Momentum of Light*: Mol. Cryst. Liq. Cryst., **143**, 89.

Santamato, E., Romagnoli, M., Settembre, M., Daino, B., and Shen, Y. R., 1988, *Self-Induced Stimulated Light Scattering*: Phys. Rev. Lett., **61**, no. 1, 113–116.

Shahinpoor, M., 1976, *On the Lehmann's effect*: Rheol. Acta, **15**, 215–217.

Stewart, I., 2004, *The static and dynamic continuum theory of liquid crystals*: Taylor and Francis, London and New York.

Tarasov, O., Krekhov, A., and Kramer, L., 2003a, *Dynamics of cholesteric structures in an electric field*: Phys. Rev. E, **68**, 031708.

Tarasov, O., Krekhov, A., and Kramer, L., 2003b, *Rotation of cholesteric drops under dc electric field*: unpublished.

Zel'dovich, B. Y., and Tabiryan, N. V., 1982, *Theory of optically induced Fréedericksz transition (OFT)*: Zh. Eksp. Teor. Fiz., **82**, 1126.

Zolot'ko, A. S., Kitaeva, V. F., Kroo, N., Sobolev, N. I., and L.Csillag, 1980, *The Effect of an Optical Field on the Nematic Phase of the Liquid Crystal OCBP*: Pis'ma Zh. Eksp. Teor. Fiz., **32**, 170.